Quantitative techniques for analysis and visualization of three-dimensional ultrasound data

Sevald Berg

Norwegian University of Science and Technology

October, 1999

Abstract

Medical three-dimensional (3D) ultrasound has become a promising technique, and exciting applications have emerged in a wide range of disciplines during the last ten years. Still, 3D ultrasound has yet to become an everyday clinical tool.

The main objectives for this thesis were to use raw ultrasound data to achieve 3D reconstructions with minimum loss of resolution, and to extract precise quantitative volumetric information from these reconstructions.

Most medical imaging techniques including ultrasound are affected by different kinds of noise. To improve image quality, a framework for nonlinear image filters based on fuzzy connected neighborhoods was developed. These filters were applied on both photographic images and medical images. Thin structures and edges were preserved even when substantial smoothing was performed.

Transvaginal 3D ultrasound was used to improve the measurement, the shape analysis, and the visualization of the endometrium, which is the inner surface of the uterus. The endometrium was identified in the 3D data and displayed with volume rendering techniques. Quantitative measurement of the endometrial thickness was possible and was used to highlight regions in the rendering process.

A method was developed to improve the volume measurement of small structures using 3D ultrasound. The resolution of the ultrasound beam was incorporated into the volume calculations to eliminate the effect of under- or overestimation due to the limited resolution. The volume estimation algorithm was verified by water tank phantom experiments. The same method was applied for the brain cavities on a series of human embryos showing the potential for measuring small organ volumes *in-vivo* with high accuracy.

Dynamic 3D echocardiography was used to develop a method for cardiac wall motion imaging. The ultrasound tissue data were reconstructed as a series of volumes throughout the cardiac cycle, and the ventricle wall motion was calculated as a set of vectors normal to the wall surface. Characteristic wall movement could be viewed in relation to the rest of the ventricular structures with color coded and surface rendered velocity values.

A method for freehand acquisition of dynamic 3D ultrasound data was developed. A position sensor device was mounted on a probe, and the accuracy of the 3D reconstructions was evaluated. Raw digital data and high frame rate acquisition improved the reconstruction quality, and examples of reconstructions of different types of ultrasound data demonstrate this method's potential to produce clinically interesting data.

Dynamic freehand 3D echocardiography was used to develop an angle-independent method for measuring blood volume flow. Ultrasound color flow data were extracted from a cross-sectional slice in the area of the aortic valve. The blood volume flow at each time instance throughout the cardiac cycle was calculated and the total blood flow determined. Examples of *in-vivo* measurements are given.

Preface

This is a doctoral thesis submitted to the Norwegian University of Science and Technology (NTNU). The research work in this thesis was carried out at three different institutions:

- National Center for Fetal Medicine (NSFM), Trondheim University Hospital
- Department of Physiology and Biomedical Engineering (IFBT), NTNU
- Department of Computer and Information Science (IDI), NTNU

My supervisors have been Professor Bjørn Olstad, IDI, and Professor Hans Torp, IFBT. Close cooperation with the Cardiology Section, Trondheim University Hospital has also been important during the thesis.

Acknowledgments

This thesis could not have been realized without extensive help and support from others. I wish to especially thank my supervisors Bjørn Olstad and Hans Torp. Their ideas, knowledge and support have been invaluable for me during the work of this thesis.

I would also like to thank Sturla Eik-Nes, head of the National Center for Fetal Medicine, for introducing me to the world of medicine while I was doing my service (in the name of peace) at his institution, and for his support during my work. I am very grateful for the collaboration with Harm-Gerd Blaas, also at NSFM. His thorough way of doing research has set an important example, and is one of the most important things I have learned during this work.

The collaboration with the Cardiology Section has been very inspiring. Many thanks to Stein Samstad, Bjørn Olav Haugen and Stig A. Slørdahl for their continuous enthusiasm. Also thank to Klaus P. Schipper for the help in the initial phases of my work.

Many of the results in this thesis would have been much harder to reach without the extensive programming help from Ditlef Martens, CMR, and Erik Steen, GE Vingmed Ultrasound. Their help is greatly appreciated.

A special thank to Anders H. Torp for solving numerous computing problems making my life with the computer much easier, and for most fruitful scientific discussions. Lots of thanks to my colleagues and friends Leif Rune Hellevik, Stein Inge Rabben, Andreas Heimdal, Steinar Bjærum, Johan Kirkhorn and Bjarte M. Østvold for all help and inspiring discussions.

Thanks to Nancy Eik-Nes for revising most of this thesis. Making my clumsy English understandable has been of great importance.

Thanks also to Bjørn Angelsen, IFBT, who made it possible for me to work for a while as a part-time system administrator at IFBT, prolonging my financial support in a critical phase of my project.

The financial support from the Norwegian Research Council and GE Vingmed Ultrasound is greatly appreciated.

Oslo, October 1999

Sevald Berg

Contents

Paper A – **Fuzzy connected neighborhood filters**
Based on *"Evaluation of fuzzy neighborhood filters in medical imaging"*.
In *Proc. of SPIE Medical Imaging*, 3034:990–998, 1997
Sevald Berg and Bjørn Olstad

Paper B – **3D transvaginal ultrasound imaging for identification of endometrial abnormality**
In *Proc. of SPIE Medical Imaging*, 2432:543–553, 1995
Bjørn Olstad, Sevald Berg, Anders H. Torp, Klaus P. Schipper and Sturla Eik-Nes

Paper C – **Accuracy of in-vitro volume estimation of small structures using three-dimensional ultrasound**
Submitted for publication, 1999
Sevald Berg, Hans Torp and Harm-Gerd Blaas

Paper D – **In-vivo three-dimensional ultrasound reconstructions of embryos and early fetuses**
Lancet, 352(9135):1182–1186, 1998
Harm-Gerd Blaas, Sturla Eik-Nes, Sevald Berg and Hans Torp

Paper E – **Quantitative wall motion coding in three-dimensional echocardiography**
In *Proc. of SPIE Medical Imaging*, 2709:424–432, 1996
Sevald Berg, Anders H. Torp, Klaus P. Schipper and Bjørn Olstad

Paper F – **Dynamic three-dimensional echocardiography using raw digital ultrasound data**
Ultrasound Med Biol, 25(5):745–753, 1999
Sevald Berg, Hans Torp, Ditlef Martens, Erik Steen, Stein Samstad, Inge Høivik and Bjørn Olstad

Paper G – **Volumetric blood flow measurement using dynamic three-dimensional ultrasound color flow imaging**
Submitted for publication, 1999
Sevald Berg, Hans Torp, Bjørn Olav Haugen and Stein Samstad

Chapter 1

Introduction

This thesis is divided into two parts. The first part contains an introduction with an overview of the thesis. A short history of 3D ultrasound is presented. Different aspects of 3D ultrasound are described supplementing the papers in part two. This includes an overview of 3D ultrasound technology with some clinical applications. The first part ends with concluding remarks and directions for further work. The second part consists of the seven separate papers. The papers are self-contained and complete with abstracts and references.

1.1 From A-mode to 3D ultrasound

Medical diagnosis using ultrasonic waves was pioneered by Howry and Bliss [42] and Wild and Reid [96] in the early 1950s developing pulsed-echo systems capable of imaging internal human organs. In 1954, Edler and Hertz [27] introduced echocardiography using the pulsed echo technique to record the moving heart walls, then Donald et al. [24] began using ultrasound in obstetrics. The use of Doppler techniques for measuring the velocity of blood was first presented in 1957 by Satumora [82]. But it was not until the beginning of the 1970s that real-time two-dimensional imaging was introduced; the subsequent rapid evolution of signal processing and computer science made ultrasound scanners important diagnostic tools in modern hospitals. Reviews of ultrasound history can be found elsewhere [58, 95].

A-mode is the simplest ultrasound imaging technique, where ultrasound pulses are transmitted into the object with a focused transducer. When the pulse propagates through the object, it is partly reflected by the differences in mechanical impedance of boundaries between structures [1]. The amplitudes of the returning echoes representing the spatial placements of these structures are displayed as an amplitude curve. When a new pulse is repeatedly transmitted, moving structures like the cardiac wall or valves can be displayed in an M-mode image, where the tissue depth is displayed along one axis and time along the other, and brightness is controlled by the echo amplitude. Two-dimensional imaging (B-mode) is achieved by sweeping the ultrasound beam in the lateral direction.

The ultrasonic pulses are generated by piezoelectric transducers, and the direction of the ultrasound beams is controlled by either mechanical or electronic beam steering. The annular array is common for mechanical steering, and consists of a set of concentric rings. The beam steering is performed by physically tilting the transducer to produce a sector image. The electronic arrays consist of a set of small transducer elements placed in a row, and the beam steering and focusing is controlled electronically by changing the transmission time for each element. In the work presented in this thesis, only probes limited to transcutaneous, transvaginal or transesophageal scanning were used, where the transducer center frequencies were in the range 2.5–7.5 MHz.

In the traditional B-mode imaging mode, two-dimensional (2D) images are created real-time by steering the ultrasound beam in, for instance, a sector pattern. Three-dimensional (3D) imaging can be obtained by steering the probe to cover a volume in space. Generally, beam steering in 3D imaging can be achieved in two ways: electronically controlled by the transducer or controlled by various means external to the probe. The latter usually involves tracking the spatial position of a B-mode image, and this has been the dominant method since commercially-available 2D ultrasound scanners could be used.

Attempts to extract volumetric information from ultrasound scans have been made since the early days of ultrasound. Howry et al. [43] scanned objects by motorized movement of the transducer. Stereoscopic images were generated from two different projections. In the beginning of the 1960s, Baum et al. [2] scanned the eye in search of orbital lesions. The scans were transferred to photographic plates and stacked to create a volume representation. Ten years later, Robinson [75] digitized a series of B-mode images and was able to derive cross-sectional images from volume data of the fetus. Dekker et al. [20] digitized A-mode beams steered with a mechanical position sensing arm to create the first ultrasound volumes of the heart. In the late 1970s, Brinkley et al. [17] developed a different position locator system based on acoustic sensing. A light pen was used to outline object borders in the B-mode images, and the corresponding contours were reconstructed in three dimensions.

The first applications of these techniques in echocardiography were focused on ventricle volume measurement. Moritz et al. [61] used the same acoustic position sensing system as above to create non-parallel ventricle contours of hearts *in vitro*. Geiser et al. [32] achieved dynamic ventricular volumes from human hearts *in vivo* using a mechanical positioning arm. Common for these first methods were the lack of computing power and cumbersome acquisition and processing techniques. Only the contours were reconstructed as volumes after digitalization, and the whole process has been reported to take as much as 4–7 days.

Visualization of volumetric information requires 3D data to be projected onto a 2D image. In the first attempts for 3D ultrasound mentioned above, the only things that were rendered were manually extracted contours giving limited impression of depth. Raichlen et al. [73] were able to create dynamic images of open chest dog heart cavities from 3D ultrasound. However, these images were only based on segmented contours, and the realism achieved was limited. Volume visualization, or volume rendering, of

3D medical data is based on ray tracing techniques adopted from computer graphics. Drebin et al. [26] presented a volume rendering algorithm where local gradients were computed and used in shading calculations. This method relied on initial classification of the volume data. Scalar fields, such as ultrasound volumes, can be rendered without this classification, as described by Sabella [77]. Ultrasound volume rendering requires computer intensive processing, and it was not until the late 1980s that successful renderings emerged. McCann et al. [57] rendered dog hearts *in vitro* and human hearts *in vivo*, and later, Steen and Olstad [88] and Sakas et al. [78] achieved realistic renderings of fetal structures *in vivo*.

In the 1990s, commercially-available dedicated 3D ultrasound scanners have made volume reconstructions of both cardiac and abdominal structures wide-spread. Position measurement using rotating stepper motors have become the most dominant technique for dynamic 3D acquisition of the heart. Roelandt et al. [76] used a rotating transthoracic probe, while Salustri and Roelandt [80] used a rotating multi-plane transesophageal probe to image the mitral and aortic valves. Tilting probes have been used for abdominal 3D acquisition, as demonstrated by Merz et al. [59] showing 3D renderings of various fetal structures, and Martin et al. [55] using a tilting transesophageal 3D probe for ventricular volume measurement.

Using a collection of 2D scan planes to acquire data on cyclically moving structures such as the heart requires monitoring and gating of physiological signals, so that individual scan planes can be reorganized according to its position in the cycle. The ECG-signal is commonly used for this purpose [57, 76]; in addition, respiration is monitored to prevent movement that can corrupt the reconstructed data. In fetal 3D echocardiography where the ECG-signal from the fetus can be difficult to detect, other methods have been used. Nelson et al. [64] described a system where one M-mode line was extracted from the rotated 3D data and used to calculate the trigger positions.

Electronic beam steering in three dimensions is achieved using a transducer matrix (2D array), as described by Smith et al. [87] and von Ramm et al. [94]. Real-time acquisition of ultrasound volume data can be achieved with this technique, making the need for ECG and respiratory gating in cardiac applications obsolete; the whole volume for a single time instance is acquired within one sweep, in a similar manner as a 2D scan plane. The amount of data to be processed by the scanner front-end (the beam-former) is huge, and it was not until the mid 1990s that such scanners became commercially available. Shiota et al. [84] performed an animal study of ventricle volumes with such a scanner.

Regardless of what techniques are used to acquire 3D ultrasound data, it is essential that both the temporal and the spatial resolutions are good to achieve clinically relevant data. During the years of development, the various methods have compromised on quality due to the lack of signal and computer processing power. This was also due to the fact that most 3D systems have been add-ons to existing 2D scanners, so access to the image formation process has not been available. Instead, the video output signal from the scanner was digitized resulting in a frame rate as low as 25 frames/s. This made the analysis of rapidly moving cardiac structures difficult, and also introduced jitter artifacts in the 3D reconstruction.

An important development that has improved the image resolution was the introduction of digital beam forming. After receiving the digitized individual signals from the transducer elements, the digital beam former can focus the beam dynamically, producing a thin ultrasound beam. Higher frame rates are achieved by duplicating the beam former components generating several receive beams that are steered and focused separately (multiple line acquisition). By using raw digital data in the 3D reconstruction, we can take advantage of these features to improve the reconstruction quality.

In the second half of the 1990s, second harmonic imaging was introduced as another image quality improvement technique. The second harmonic component of the received signal is used as the image formation source. The beam width of this component is narrower than the first harmonic, resulting in better lateral and elevation image resolution. Improved resolution in the elevation direction is desirable when stacking a set of 2D slices to produce the 3D volume. The 1D phased array transducers have a rather poor elevational resolution, and the focus can not be changed dynamically. Transducers with a few elements in the elevation direction have been introduced (e.g., 1.5D arrays), so that several foci can be achieved [18].

An important quantitative ultrasound technique is to use the Doppler shift from a series of returning echoes, so that blood flow velocity can be measured [1]. Pulsed wave (PW) and continuous wave (CW) Doppler techniques have become everyday clinical tools for diagnosis of cardiac disorders [38]. Kasai et al. [47] introduced color flow imaging (CFI), where the blood flow velocities were estimated from the Doppler shifts using autocorrelation techniques, and color coded and displayed onto the tissue image to visualize the flow distribution. Later, myocardial velocities were achieved using similar techniques [60], creating tissue Doppler imaging (TDI), and recently, Heimdal et al. [39] introduced Doppler techniques for measuring the myocardial strain rate (SRI). Various other quantitative methods have been developed for measuring the cardiac function [28], but a description of these goes beyond the scope of this introduction.

Volume estimation was one of the first applications of quantitative 3D ultrasound [17, 33]. This is still an important application and is usually performed by manually tracing contours in a 3D dataset [35, 36, 44]. Ghosh et al. [34] described a method for ventricle volume estimation from a limited number of 2D scan planes. Mæhle et al. [54] extended this methodology to encompass quantitative wall motion and regional phase analysis. There have also been attempts to quantify volumes of regurgitation jets by 3D color Doppler [85], as well as measurement of cardiac output from volumetric blood flow [72].

Three-dimensional ultrasound has yet to become an everyday clinical tool, mainly due to the complicated recording procedure, and the question as to whether 3D ultrasound improves the diagnosis compared to 2D ultrasound. The acquisition methods must be improved, and reliable techniques for analysis of 3D ultrasound data must be developed.

1.2 Aims of study

The availability of raw digital ultrasound data for 3D processing can potentially improve the reconstruction and the quantitative analysis of volumetric ultrasound data.

The aim of this thesis is the evaluation and development of techniques for providing 3D ultrasound data with little loss of resolution compared to the original ultrasound data, and for doing precise quantitative analysis of such volumetric information.

Three-dimensional data can be acquired in many ways. We will mainly focus on two methods: rotational probe for the transvaginal applications, and position sensing devices for the cardiac applications. Both the temporal and the spatial resolution in the data reconstruction are important for the quality of the visualizations and of the measurements.

Ultrasound images are affected by different kinds of noise. We address this by introducing a general framework for non-linear filters that can potentially improve image quality.

Volume measurement of small structures can be difficult due to the relatively low resolution of the ultrasound beams. We focus on the accuracy of such measurements by incorporating the beam resolution in the calculations. The original Doppler velocity estimates provided by the raw digital data can be used to create 3D velocity data. This will be exploited in the measurement of cardiac blood volume flow.

1.3 Contributions

The main contributions of this thesis are summarized as follows:

- A framework for a new class of non-linear filters based on fuzzy connected neighborhoods was developed. The filters were capable of preserving fine structures in the images even during strong filtering. The filters were applied to both synthetic images with known noise level and to ultrasound images.

- A dynamic 3D freehand ultrasound system was developed. Raw digital data were used to produce optimal 3D ultrasound data. Results show *in vivo* 3D reconstruction and visualization of mitral and aortic valve morphology and blood flow, and myocardial tissue velocity. The reconstruction errors were smaller than the resolution of the original ultrasound beam, and a temporal resolution up to 150 frames/s was achieved.

- A dedicated transvaginal 3D ultrasound probe was used to create optimal 3D reconstructions for different clinical applications such as the endometrium or the fetus *in vivo*.

- A method for accurate volume measurement of small structures with special attention to fetal structures was developed. Both *in vitro* and *in vivo* validation were performed. Volume of brain cavities of embryos down to 7 weeks of age were measured.

- A method for wall motion analysis from dynamic 3D echocardiographic data was developed. The velocity of the cardiac wall was calculated from gray scale tissue data; volume distance transform algorithms were used. The instantaneous velocity was visualized as a color coded surface rendering.
- A method for volumetric blood flow measurement using 3D color flow imaging was developed. The cardiac output measurement was independent of the actual blood flow direction, and the blood volume flow through moving anatomical structures such as the heart valves was measured.

1.4 Publications

The journal papers, conference articles, and conference abstracts produced during this work are listed in the References [5–15, 67, 86].

1.5 Summary of papers

Paper A — Fuzzy connected neighborhood filters

Different non-linear filters have been applied to medical ultrasound imaging to reduce speckle and other forms of noise. Image smoothing is necessary in 3D ultrasound imaging where additional noise appears due to motion artifacts and reconstruction jitter. In this paper, we present a general framework of a new class of nonlinear digital filters based on fuzzy connected neighborhoods. These neighborhoods defined the filter mask and were found by calculating a shortest-path based on different criteria. An introduction to fuzzy neighborhoods is given, and average and regression filters are described. The fuzzy neighborhood approach offered flexibility in the design of the filters. The framework was adapted to photographic images, ultrasound images and multi-spectral images, and was well-suited for temporal and multi-dimensional applications. No quantitative comparison with other filters was performed. Results showed that these filters can reduce noise and still maintain fine, thin structures without blurring edges.

S. Berg did the experiments and wrote the paper, and B. Olstad assisted with the experiments and supervised the work.

Paper B — 3D transvaginal ultrasound imaging for identification of endometrial abnormality

This is the first of three papers related to transvaginal 3D ultrasound applications. In this paper, we present methods to improve the measurement, shape analysis, and visualization of the endometrium, which is the inner surface of the uterus. Endometrial growth or textural changes can be a risk indicator for different pathological lesions. We acquired volume data of the endometrium by rotating a transvaginal probe with a stepper motor. Identification of the endometrial border was performed using semi-automatic active contour techniques on the reconstructed 3D data. From these contours, the shape of the endometrium was visualized and used to do quantitative measurements of the thickness. The voxels representing the inside of the endometrium were volume rendered in order to emphasize inhomogeneities. To accommodate for these inhomogeneities that can exist both on the outside and the inside of the endometrium, the rendering algorithm had a controllable opacity function. A 3D distance transform was applied to the data volume measuring the shortest distance to the detected endometrial border for each voxel. This distance was used as a basis for opacity computations which allowed the user to highlight different regions of the endometrium.

B. Olstad supervised the work and wrote part of the paper, S. Berg did the 3D reconstructions and analysis, and wrote most of the paper, A. H. Torp developed the active contour algorithms, K. P. Schipper assisted with the technical performance of the experiments, and S. H. Eik-Nes supervised the clinical experiments.

Paper C — Accuracy of in-vitro volume estimation of small structures using three-dimensional ultrasound

The results from the previous paper were promising. However, an ordinary 2D probe was used to acquire the 3D data. Since this probe was not designed to rotate, the 3D data contained geometrical reconstructions artifacts. To eliminate these errors we developed a dedicated ultrasound probe for transvaginal 3D imaging. The transducer was an annular array with a center frequency of 7.5 MHz. The transducer was rotated with an internal stepper motor. The probe had no external moving parts, and the total volume covered by a full rotation defined a half sphere. The raw digital data from the scanner were transferred to an external PC for 3D reconstruction. We evaluated the 3D imaging system by measuring the volume of a series of phantoms (range 24.8–3362.5 mm^3) in a water tank, and found good correlation with true volumes (linear regression with a slope of 0.967 and R^2 = 0.993). The mean percentage error was -3.4% ± 7.4%. The effect of under- or overestimation due to the limited ultrasound beam resolution was taken into account by incorporating the size of the point-spread function in the calculations. An example of data acquisition, volume estimation and visualization of an embryo less than 8 weeks old *in vivo* with the brain cavities and body was given. We conclude that the 3D reconstruction and the volume estimation were accurate, and that it was possible to visualize and measure embryonic organ volumes.

S. Berg did the phantom experiments, assisted with the technical performance of the clinical experiments, and wrote the paper, H. Torp supervised the work, and H.-G. Blaas assisted with the phantom measurements and did the fetal acquisitions and reconstructions.

Paper D — In-vivo three-dimensional ultrasound reconstructions of embryos and early fetuses

The transvaginal 3D probe described and evaluated in the previous paper was now applied *in vivo* to measure volumes of brain cavities of human embryos during early pregnancy. We included 34 women at 7-10 weeks' gestation. We measured the crown-rump length (CRL) of the embryos and fetuses and transferred the 3D ultrasound data to an external computer for further processing to calculate volume. The CRLs ranged from 9.3 mm to 39.0 mm. The quality of the images of the embryos and fetuses made it possible to outline in detail the outer contours and the contours of the brain cavities. The calculated volumes corresponded well to the descriptions from classic human embryology.

H.-G. Blaas planned the study, did the ultrasound examinations and the 3D reconstructions, and wrote the paper. S. H. Eik-Nes supervised the planning and revision of the study and its results. S. Berg assisted with the technical performance of the 3D reconstructions of the test series and of the study objects. H. Torp assisted with the mathematical assessment of the 3D analysis and the validity of the method.

Paper E — Quantitative wall motion coding in three-dimensional echocardiography

The next three papers take up different aspects of dynamic 3D echocardiography with the focus on optimal data reconstruction and quantitative analysis. In 2D echocardiography, wall motion analysis is important in detection of heart dysfunction. Conventional methods suffer from being only approximations due to the complex movement of the heart. In this paper, we used 3D ultrasound to improve the quantitative analysis of the left ventricular wall motion. A motor rotating the probe one step for each cardiac cycle was used to acquire data. The wall motion was calculated using the 3D Euclidean distance transform, resulting in a set of vectors normal to the endocardial surface. The endocardial wall velocity values were color coded and the surface was rendered creating a cineloop of the left ventricle with color intensities indicating the wall motion. The 3D motion coding technique allowed for a quantitative analysis of the heart function. Infarcted areas were shown with different color intensities than the rest of the heart due to the muscle activity reduction in that region.

S. Berg did the 3D reconstructions and analysis and wrote the paper, A. H. Torp developed the active contour algorithms, K. P. Schipper assisted with the 3D acquisitions, and B. Olstad supervised the work.

Paper F — Dynamic three-dimensional echocardiography using raw digital ultrasound data

The previous paper used a rotating stepper motor for the 3D acquisition and based the reconstruction on the video signal from the scanner. The data acquisition time was more than 3 min, and the low frame rate introduced reconstruction artifacts.

In this paper, we describe a new method to construct dynamic 3D ultrasound data that reduced both acquisition time and reconstruction artifacts. We used an electromagnetic position sensor device attached to the ultrasound probe for spatial location of the probe, which was slowly tilted in the transthoracic scanning position. The 3D data were recorded in 10–20 s, and the analysis was performed on an external PC within 2 min after the raw digital ultrasound data were transferred directly from the scanner. The spatial and temporal resolutions of the reconstruction were evaluated and were superior to video-based 3D systems. Examples of volume reconstructions with better than 7 ms temporal resolution are given. The raw data with Doppler measurements were used to reconstruct both blood and tissue velocity volumes. The velocity estimates were available for optimal visualization and for quantitative analysis. The freehand data reconstruction accuracy was tested by volume estimation of balloon phantoms, giving high correlation with true volumes. Results show *in vivo* 3D reconstruction and visualization of mitral and aortic valve morphology and blood flow, and myocardial tissue velocity. We concluded that it was possible to construct multi-modality 3D data in a limited region of the human heart within one respiration cycle, with reconstruction errors smaller than the resolution of the original ultrasound beam, and with a temporal resolution of up to 150 frames/s.

S. Berg did the 3D analysis and wrote the paper, H. Torp assisted the writing and analysis, D. Martens implemented the 3D reconstruction, E. Steen implemented the 3D visualization, S. Samstad assisted with the 3D acquisitions, I. Høivik integrated the position sensor with the ultrasound system, and B. Olstad supervised the work.

Paper G — Volumetric blood flow measurement using dynamic three-dimensional ultrasound color flow imaging

The routine method of estimating blood volume flow using Doppler and 2D echocardiography is an approximative method which is sensitive to measurement errors. The method measures the aortic outflow and is not suitable to measure the mitral inflow. In this paper, we used the 3D acquisition technique described in the previous paper, and estimated the blood volume flow independently of the flow direction using the raw 3D data. The ultrasound data were acquired in color flow imaging mode, and separate raw digital tissue and Doppler data were transferred to an external PC for post-processing. From each time step in the reconstructed 3D data, one cross-sectional slice was extracted with the measured and recorded velocity vector components perpendicular to the slice. The volume flow rate through these slices was found by integrating the vector components, and was independent of the angle between the actual flow direction and the measured velocity vector. Allowing the extracted surface to move according to the movement of anatomical structures, an estimate of the flow through the cardiac valves was achieved. The temporal resolution was preserved in the 3D reconstruction, and with a frame rate of up to 104 frames/s the reconstruction jitter artifacts were reduced. Examples of *in vivo* blood volume flow measurement are given, showing the possibilities of measuring the cardiac output and analyzing blood flow velocity profiles.

S. Berg did the 3D analysis and wrote the paper, H. Torp supervised the work and assisted with the 3D analysis, B. O. Haugen assisted with the 3D acquisitions, and S. Samstad supervised the clinical experiments.

Chapter 2

Building blocks of a 3D ultrasound system

During the past 20 years, 3D medical ultrasound applications have emerged in most areas where ordinary 2D ultrasound has been applied. This includes volume measurement of abdominal organs [35], 3D reconstruction of intracoronary data [21, 23], 3D reconstruction and visualization of cardiac structures of both adults [81] and infants [93], 3D imaging of the eye [25], assessment of uterine anatomy [46], volume measurement of embryonic brain cavities [15], various applications in radiology [37], and methods for 3D ultrasound guided neurosurgery [53]. Reviews of the history of 3D ultrasound can be found elsewhere [4, 63].

This chapter describes the different techniques required to produce the 3D ultrasound data presented in this thesis. Focus is put on aspects which are not well described in the papers.

2.1 Ultrasound probes for 3D acquisition

A wide range of technical arrangements for acquisition of 3D ultrasound data have been presented. The most successful solutions can be divided into three groups: motorized movement, freehand position sensing, and 2D array scanning. Fig. 2.1 shows some images of different probes used in this thesis. Common for these probes is that they can be used for both static and dynamic imaging.

2.1.1 Motorized movement

The motor moves the ultrasound probe in a predefined pattern. Most common are rotating (Fig. 2.1(a) and (c)), tilting (Fig. 2.1(b)), and translating movements. During acquisition, both the patient and the probe must be kept in a stable position in order to avoid geometrical reconstruction artifacts. The amount of probe movement is

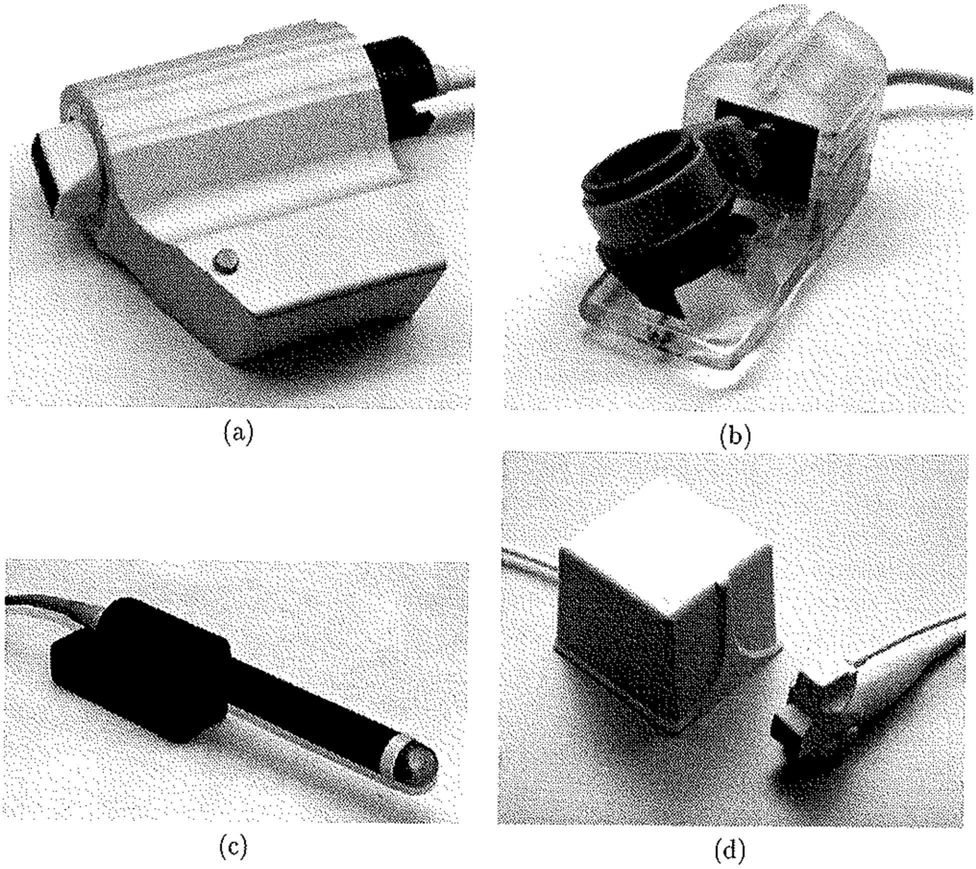

(a) (b) (c) (d)

Figure 2.1: Four different 3D probes referred to in this thesis. (a) Rotational probe. (b) Tilting probe. (c) Rotational transvaginal probe. (d) Probe with magnetic position sensor.

determined by the motor movement, so that each recorded ultrasound frame is labeled with its relative spatial position. It is also possible to synchronize the motor steps with the frame sampling on the scanner. Rotational probes are described and used in Papers B–E.

The advantage of these probes is that they create a regular geometry which is easy to manipulate in the post-processing applications. Successful imaging with ECG and respiration gating for dynamic 3D echocardiography has been implemented using both transthoracic and transesophageal rotating probes. The disadvantage is that the probes must be kept stable during the whole acquisition, which is difficult to achieve when the acquisition time is long.

2.1.2 Freehand position sensing

Since the spatial position of the ultrasound probe is continuously recored when using position sensing, the probe may move freely during data acquisition. Several different position locator systems for freehand 3D ultrasound have been described: 1) Magnetic systems (Paper F, [22]), where a transmitter generates a magnetic field and a sensor is mounted on the ultrasound probe. The position and the orientation of the sensor is continuously recorded (Fig. 2.1(d)); 2) Acoustical systems [61], where an array of spark gaps mounted on the probe emits acoustic waves which are sensed by an array of microphones; 3) Mechanical systems [32], where the probe is mounted onto a mechanical arm with several degrees of freedom; and 4) Optical systems [53], where light sources are mounted on the probe.

The freehand systems prevent the examiner from having to keep the probe in a stable position during the acquisition. Motion artifacts will then only result from movement of the patient. The best possible acoustic window can be chosen during acquisition. The optical systems have better resolution than the magnetic systems, and are not affected by surrounding ferromagnetic equipment. However, the movement can be limited to avoid the sensor from being obscured by the optical transmitters. For all systems, there is a need for accurate calibration techniques.

2.1.3 Two-dimensional transducer arrays

Whereas 1D transducer arrays consist typically of 96–128 elements, 2D arrays may consist of as many as 2000–10000 elements [87, 94]. The amount of parallel processing of the receive beams is tremendous, so it is necessary to reduce the number of beams. This can be achieved by using sparse arrays, which must be optimized to reduce side-lobe levels [41].

The current commercially available 2D array scanner from Volumetrics (Model 1) is equipped with a transducer with almost 2000 elements. The aperture is circular symmetric. Beam resolution is thus equal in both the azimuth and the elevation directions. The pyramid shaped scan volume consists of 4096 beams generated with 16×MLA (multiple line acquisition) on 256 channels. The volume rate is reported to be up to 45 volumes per second. This scanner is also capable of providing volumetric color flow data, but the volume rate is at the moment as low as 2–4 volumes per second.

The 2D arrays are superior to other techniques in that they record a data volume real-time with no physical movement of the probe. The reconstructed data have very little geometrical distortion, and such probes are capable of scanning a series of volumes of the heart in just one cardiac cycle. The problem is that it is difficult to achieve acceptable image quality and frame rate with today's technology.

2.1.4 Other methods

There are other techniques for 3D acquisition. Omoto et al. [68] presented preliminary results using a mechanically tilted phased array transducer. The 2D scan plane was rapidly tilted back and forth, and the corresponding volume data for each scan were presented as volume rendered images with the rendering direction equal to the beam direction. Even though this was one of the first real-time rendered applications, both the spatial and temporal resolutions were too coarse to produce acceptable image quality. Another acquisition variant was presented by De Jong et al. [19], where the probe was capable of rotating the transducer continuously in one direction at a speed of 8 rotations per second, producing 16 cardiac volumes. These volumes were reconstructed off-line. For these methods, the image quality is not at the moment acceptable for clinical use.

2.2 Volume data reconstruction

The ultrasound beams are stored on the scanner as a matrix of beam samples with the geometry information stored separately. This is a dense representation which requires a minimum of disk space without reducing the data quality. Data files from dynamic 3D acquisitions can become quite large (more than 60 MB), so efficient use of the raw data is required.

Acquisition of CFI data results in two separate datasets representing the tissue and the Doppler data respectively. The CFI data have different properties than the tissue data, and must be processed differently as described in Paper G.

2.2.1 Scan conversion and interpolation

When the beam samples are to be displayed on the screen, they must at one point be converted to fit the regular geometry on the display. The display matrix has limited resolution, and the conversion is based on the geometry information from the scanning. This process is referred to as *scan conversion*. When producing a 2D image, each ultrasound scan line is converted to fit the rectangular grid resulting in a set of staircase-shaped lines. Equally, for the 3D data case, each scan line must fit the regular geometry of the cuberille. In both the motorized and the freehand position locator scans, the individual 2D scan planes have well defined positions in space.

The gaps between each individual scan converted scan line are then interpolated using bilinear or trilinear interpolation in the 2D and 3D case respectively.

Two aspects can be considered to increase the efficiency of the scan conversion and interpolation: 1) the scanning geometry; and 2) the display method. If the scan plane has been rotated or tilted in a regular manner, the reconstruction can take advantage of this to create efficient lookup-tables. However, for a freehand scan, each volume is different and must be calculated separately, as described in Paper F. When the volume data are visualized as 2D slices through the volume, there is no need to reconstruct the whole dataset; only the data of interest are converted, thus reducing the amount of computation.

2.2.2 Cardiac gating

Using motorized or freehand techniques for dynamic 3D data acquisition of the heart requires cardiac gating (triggering). This means that since the recorded ultrasound images are collected from several consecutive cardiac cycles, the set of scan planes in each cardiac cycle does not constitute the same volume, and the planes must be reorganized according to their position in the cycle. In Paper F, a detailed description of this algorithm is given. The gating is usually performed in real-time in the ultrasound scanner [69], resulting in one trigger position for each cardiac cycle.

Since several cardiac cycles are used, the reconstruction becomes sensitive to heart beat variability. For patients with arrythmia, the lengths of the cardiac cycles vary considerably, but even normal beating hearts have significant variations. These variations are not equally distributed throughout the cycle. The period from the initialization of the cycle (P-wave) to the end of systole is almost constant for all cycles. Most of the variations are found in the last part of diastole. This means that the different cycles can not be aligned by linear stretching. In Paper F we proposed that the reconstruction should be performed by using the first N image frames in each cycle, where N is the number of frames in the shortest cycle. The first frame in each cycle will constitute the first data volume, and should be chosen as the frame corresponding to the start of the P-wave, i.e., when the contraction starts. In Fig. 2.2 we show the effect of choosing a different start position. Fig. 2.2(a) is the original scan plane of a parasternal long axis view of mitral and aortic valves. The probe was coupled to a position sensor and was kept at the same position during 6 cardiac cycles. The recorded data were reconstructed as though they were translated in a linear manner. Fig. 2.2(b) shows two reconstructions of slices through the data as indicated by the dotted line in Fig. 2.2(a). We can see by the straight lines created by the myocardium that the probe was stable during acquisition, which was verified by reconstructing the images using the position data. In the left image in Fig. 2.2(b), the first frame in each cycle was chosen to be at the R-wave in the QRS complex, while in the right image the start frame was 100 ms earlier. As seen from Fig. 2.2(a), the slices were taken while the mitral valve is closing. The reconstruction starting at the R-wave shows more artifacts than the one starting at the P-wave, suggesting that our assumptions were correct. However, this method will only work for small cardiac cycle variations. In situations of, for example, extra-systole, other techniques must be used.

One possible way to overcome the problem of irregular heart beat is to record

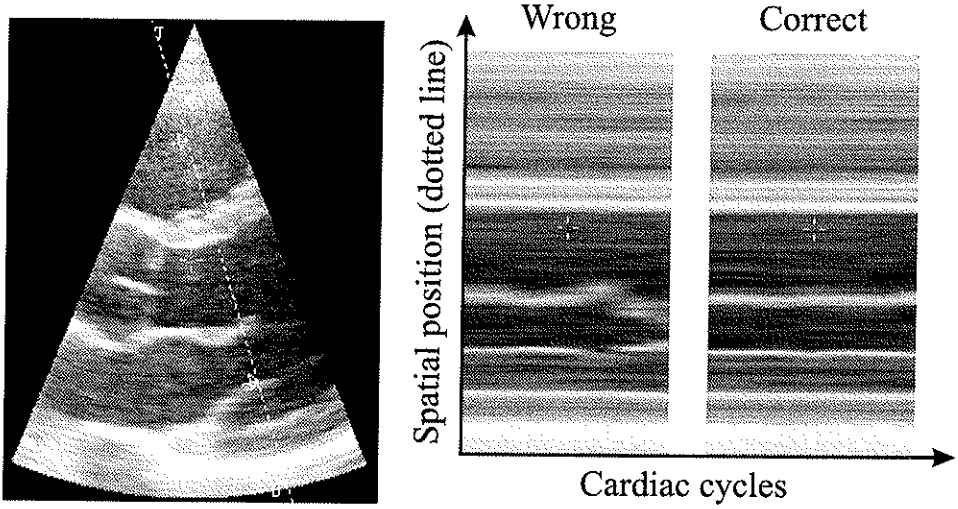

(a) (b)

Figure 2.2: Reconstruction effect of different start frames. (a) The original parasternal long axis scan plane. The dotted line indicates the position of the slices. These slices pass through the mitral valve in the left ventricle. (b) Slice through the mitral valve when reconstruction start frame is at the R-wave (left), and with the start frame 100 ms earlier (right).

only the cycles whose ECG R–R-intervals are within certain limits. This selection is performed during scanning, and the movement of the probe stops until valid cycles reappear. This has been implemented using a rotational stepper motor that was rotated a small step (typically 3 degrees) for each valid cardiac cycle [80]. The main problem with such a solution is that the total acquisition time becomes several minutes, resulting in increased motion artifacts due to movement of the patient and the probe. The gating can also be performed off-line, as described in Paper F, but removing non-representative cycles after acquisition will result in gaps in the data.

Respiration is an additional physiological parameter used for gating. The patient must breathe if the recording takes several minutes. This introduces movement of the chest which again results in irregular movement of the probe in relation to the heart. The respiration cycle can be extracted from the ECG-signal using a low-pass filter. Thus, by allowing data collection only within a certain period of the respiration cycle, motion artifacts can be reduced.

The audio signal from the heart valves can also be used for cardiac gating. The sound caused by the opening of the mitral valve can be used to create at least one data volume during the isovolumetric phase. This can be useful for analyzing cardiac function during this phase of the cardiac cycle.

Dynamic 3D echocardiography of the fetal heart requires different gating methods. The ECG signal is dominated by signals from the mother's heart. Nelson et al. [64] demonstrated the use of an M-mode for fetal cardiac gating. The probe was rotated with the rotation axis positioned along a line intersecting the moving valves. The ultrasound tissue data from this axis was extracted to produce an M-mode with characteristic detection points for each cardiac cycle.

2.2.3 Temporal reconstruction resolution

The ability for the human eye to perceive motion is limited, so about 25 frames/s is a sufficient frame rate for imaging systems. However, the need for higher temporal resolution is strongly motivated by two needs: 1) to be able to evaluate rapidly occurring events such as contraction wave propagation or valve motion; and 2) to reduce 3D reconstruction jitter artifacts. During the past 10 years the development of dynamic 3D echocardiography has been dominated by add-on equipment for existing ultrasound scanners, with extensive use of frame-grabbed video output signals. Though volume rendered images have been shown, they can not reveal details of the valve movement due to the low temporal resolution (25 frames/s for the PAL video standard). The low frame rate also introduces reconstruction jitter artifacts.

The reconstruction jitter is due to the fact that there is no synchronization between the ECG signal, the scanner frame sampling and the video frame grabbing. In Fig. 2.3 we illustrate the effect of low frame rate in the 3D reconstruction. At the top, we see the ECG signal of the systolic part of the cardiac cycle. In this particular case, the systolic part lasts 350 ms. The vertical line through the QRS complex indicates the trigger position. The top horizontal line shows the frame sampling of the scanner at a frame rate of 25 frames/s. This gives a temporal resolution of 40 ms, and consequently, the

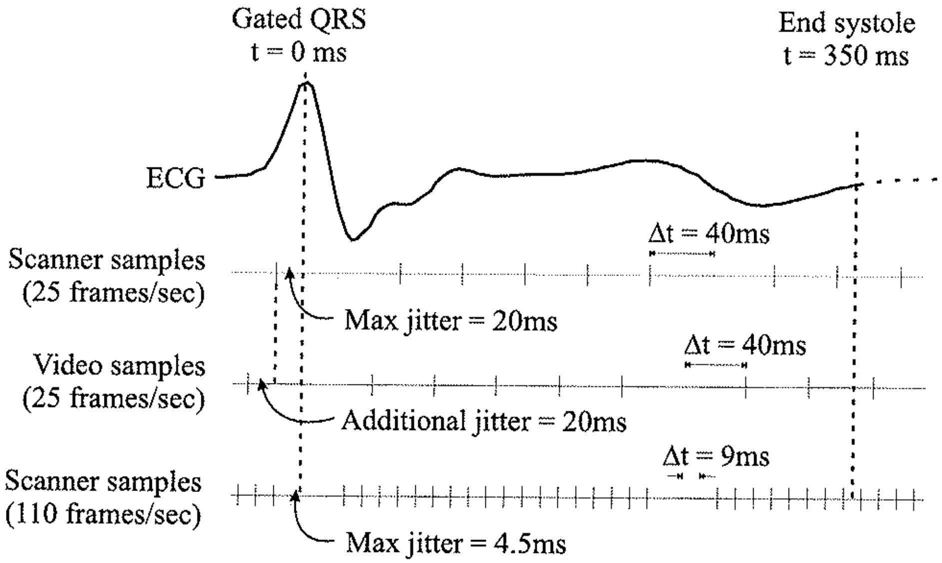

Figure 2.3: Illustration of the how the lack of synchronization between the ECG and the image sampling causes jitter. The ECG represents only the systole.

maximal jitter is ± 20 ms. With this resolution, approximately 10 frames are sampled during systole. This means that the 2D frames in a reconstructed data volume at a given time step can represent tissue movement 20 ms apart. If this signal is video-grabbed, as indicated by the next line in Fig. 2.3, this uncertainty is doubled, resulting in a total maximal error of 40 ms within one reconstructed volume. However, increasing the scanner frame rate to 110 frames/s, and using the raw digital data directly, the jitter decreases to 4.5 ms. In this case, the systole in Fig. 2.3 is covered by more than 30 frames.

In Fig. 2.4 the reconstruction jitter is illustrated. The images represent cross-sectional slices through the mitral valve from two consecutive acquisitions from the same heart. The acquisition was performed using a position sensor, tilting the probe in a parasternal long-axis position. Both slices are taken at the position indicated by the dotted line in Fig. 2.2(a). In Fig. 2.4(a) the data were recorded with a frame rate of 30 frames/s, while in Fig. 2.4(b), we used 200 frames/s. In both reconstructions the start-frame was chosen at the P-wave. We can observe that reconstruction noise is considerable in Fig. 2.4(a), where the maximal jitter was 16.7 ms. In Fig. 2.4(b) this noise is reduced significantly, and here the maximal jitter was only 2.5 ms.

The reconstruction jitter artifacts can be removed by constructing a scanner which synchronizes the data acquisition with the cardiac gating. When the trigger position is found the acquisition must be restarted so that for each cardiac cycle the scanning

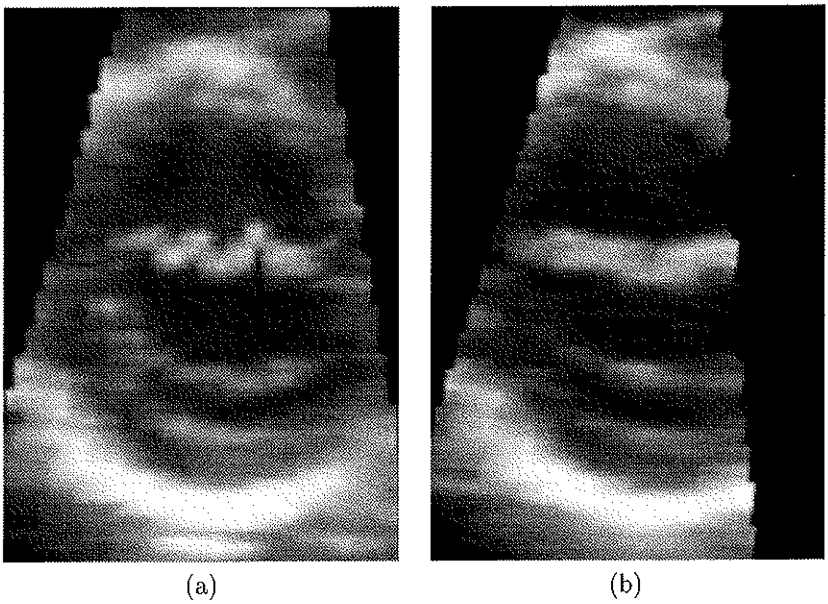
(a) (b)

Figure 2.4: 2D slices through the mitral valve from two 3D reconstructions with different temporal resolutions. (a) 30 frames/s. (b) 200 frames/s.

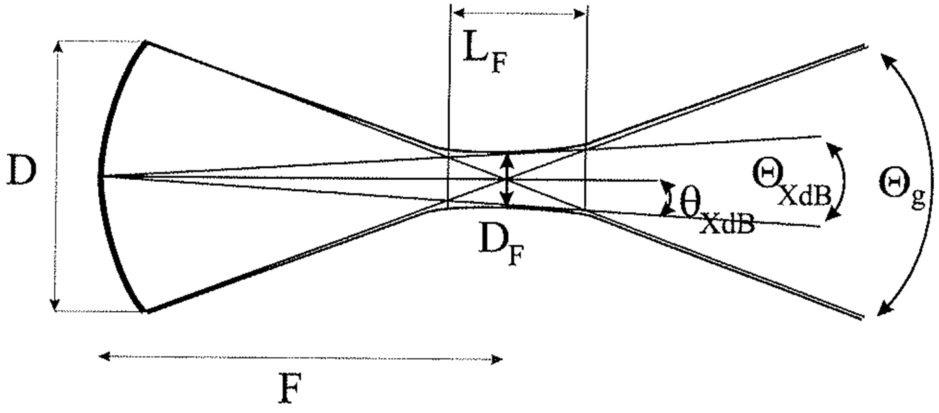

Figure 2.5: The focusing of the ultrasound beam. D is the aperture diameter, F is the focal length, $\theta_{X\text{dB}}$ and $\Theta_{X\text{dB}}$ are the single and dual sided opening angle respectively, where the amplitude has fallen X dB off from the axial value, Θ_g is the geometrical opening angle, D_F is the focal diameter, and L_F is the depth of focus (the focal zone).

starts at this position. Then, by using the raw data, no jitter is created even for low frame rate acquisition.

2.2.4 Spatial ultrasound beam resolution

By carefully considering the ultrasound beam profile, optimal 3D reconstructions can be made, and more accurate volume measurements of small structures can be performed (Paper C). In Fig. 2.5, the beam profile of a focused transducer is illustrated. This beam has a limited spatial resolution which means that all structures in the resulting image will be smeared out in accordance with the size of the image point-spread function.

All data acquisitions in this thesis are performed either with an annular array or a linear phased array transducer. For the annular array, the aperture is circular which gives a symmetrical beam with equal azimuth and elevation resolution. For the linear phased array, the elevation aperture is typically smaller than the azimuth aperture, resulting in a wider elevation focus. In addition, dynamic focusing is not possible in the elevation direction since only one transducer element is used to focus in that direction.

The two-way transducer beam profile in the focal zone is described by either a $\text{sinc}^2(x)$ or a $\text{jinc}^2(x)$ function depending on whether the aperture is rectangular or circular respectively [1]. The $\text{jinc}(x)$ function is defined as $\text{jinc}(x) = 2J_1(\pi x)/\pi x$, where J_1 is the Bessel function of the first kind and first order. The spatial resolution of the received ultrasound beam from a point scatterer is now defined by the amplitude of the main-lobe of these functions, which are plotted in Fig. 2.6. The beam profile of

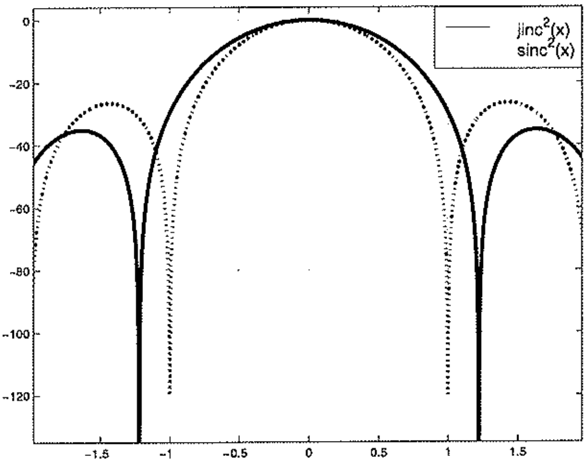

Figure 2.6: The main- and first side-lobe of the two-way beam profile for both the circular (jinc) and rectangular (sinc) aperture in dB scale.

a rectangular transducer is described with:

$$p(\theta) = \mathrm{sinc}^2(\frac{D}{\lambda}\sin\theta), \tag{2.1}$$

where θ is the single-sided opening angle, λ is the ultrasound wavelength, and D is the aperture diameter. The dual-sided opening angle Θ is then $\Theta = 2\theta$. Since $\Theta \approx \sin\Theta$ for small angles, we find Θ defined by the X dB beam amplitude reduction as

$$\Theta_{X\mathrm{dB}} = k_{X\mathrm{dB}} \cdot \frac{\lambda}{D}. \tag{2.2}$$

The parameter $k_{X\mathrm{dB}}$ is the two-way amplitude reduction factor, and values for both the circular and rectangular aperture are given in Table 2.1. The lateral beam resolution, D_F, at a given focus F, is now defined as

$$D_F = \Theta_{X\mathrm{dB}} \cdot F = k_{X\mathrm{dB}} \cdot \frac{\lambda}{D} \cdot F. \tag{2.3}$$

The depth of focus, L_F, is defined as the region where the beam diameter is limited by diffraction, and can be expressed as where the on-axis beam amplitude has dropped 1 dB:

$$L_F(1\ \mathrm{dB}) = 2 \cdot D_F(12\ \mathrm{dB}) \cdot \frac{F}{D}. \tag{2.4}$$

The resolution in the radial direction is given by the length of the transmitted pulse T_p:

$$\Delta r_p = c \cdot \frac{T_p}{2} = \frac{\lambda}{2} \cdot f \cdot T_p, \tag{2.5}$$

XdB	6	12	24	∞
$k_{X\mathrm{dB}}$–circular	1.0	1.4	1.9	2.4
$k_{X\mathrm{dB}}$–rectangular	0.9	1.2	1.6	2.0

Table 2.1: The dual-sided, two-way amplitude reduction factor $k_{X\mathrm{dB}}$ for the circular and the rectangular aperture.

where c is the sound velocity and f is the transmit frequency. Here, $c = 1540$ m/s was used as the mean value for tissue. The product $f \cdot T_p$ is the number of periods in the transmitted pulse.

To achieve sufficiently long elevation focus F, the elevation aperture D must be small. According to Eq. 2.3, this gives poorer resolution in the elevation direction. As described earlier, the reconstructed 3D data consist of a set of 2D slices stacked together. For each individual slice, high azimuth resolution is obtained. However, the resolution between each slice will suffer from the relatively poor elevation resolution, especially where the beam is not in focus. This fact must be kept in mind when structures lying far from the transducer are being imaged, e.g., the mitral and aortic valves when the probe is placed in an apical position.

In Paper C and D we used the beam resolution values to create a better volume estimate with special attention to small structures. In Paper F the resolution values were used to define the optimal sampling density of the scan planes to create 3D reconstructions with as high resolution as possible.

2.3 Data enhancement

Ultrasound images are characterized by speckle and noise from reverberations and phase aberrations. Methods for reducing ultrasound speckle have been presented previously [40]. A range of nonlinear filters can be used for digital image processing, such as order statistic filters, morphological filters or polynomial filters [71]. Temporal filters are commonly used in ultrasound scanners for display of both B-mode and color flow images. In 3D ultrasound imaging, additional noise appears due to motion artifacts and reconstruction jitter. Spatial and temporal smoothing filters have been used to improve volume visualizations. Sakas et al. [78] used both Gaussian and median filters for noise reduction and created smooth surface reconstructions of fetal structures. The amount of filtering was a trade-off between smooth surfaces and loss of information. Steen [89] used an anisotropic diffusion filter for 3D ultrasound data to improve both edge detection and volume rendering. The filter weight function was adapted to ultrasound images resulting in a filter with edge preserving characteristics. In Paper A we present a filter framework based on fuzzy connected neighborhoods. The described filters can perform strong image smoothing while preserving edges. The framework is general and can be used for spatial, temporal and multi-spectral data.

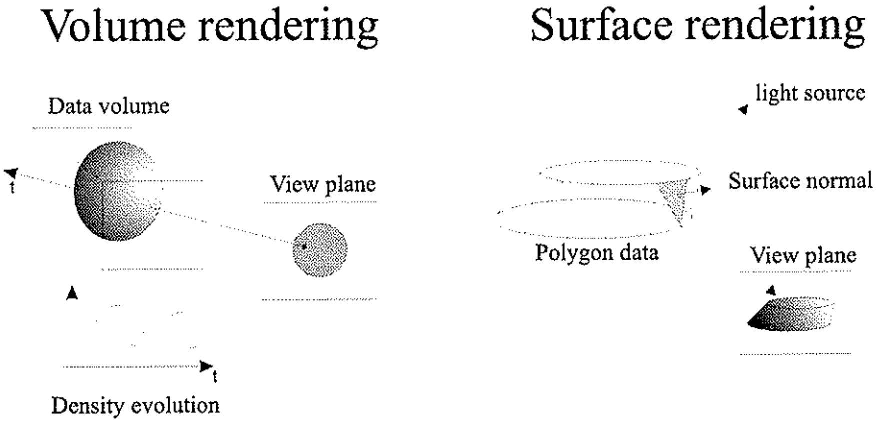

Figure 2.7: Two different rendering models. Volume rendering can be used for volumes without any predefined objects. Surface rendering applies to polygon data representing objects with known geometry.

2.4 Visualization

Visualization of volumetric medical data is based on techniques adopted from computer graphics, where well-defined spatial objects are displayed using different ray-tracing and shading techniques [31]. Medical data do not usually contain explicit definitions of different structures. The resulting volumes consist of a set of pixels or voxels with no relation to each other. In addition, the inherent properties of ultrasound regarding the relatively low resolution and the low signal-to-noise ratio, make volume visualization a difficult task. We can divide the most common methods for visualizing volumetric ultrasound data into the following:

- **2D slicing.** Slicing is the most straightforward way of visualizing volumetric data. Slicing consists of extracting a 2D slice from 3D data at a specified position and angle. Orientation can be a problem using this method with no obvious landmarks in the data. Defining three orthogonal slices may ease the orientation. Slicing with full positional freedom is called "any-plane slicing".

- **Volume rendering.** Volume rendering algorithms for projecting 3D medical data onto a 2D plane have been described for use with magnetic resonance (MR) or computed tomography (CT) imaging [26, 52]. As opposed to polygon-based surface rendering methods, these techniques do not use discrete decisions that tend to create sharp boundaries in diffuse transitions found in medical images. The quality of the underlying MR or CT data makes it possible to incorporate illumination models in the calculations, creating realistic surface shaded renderings. The method of Drebin et al. [26] also relied on an initial classification of the voxels into different categories. This is difficult to achieve for 3D ultrasound data, so algorithms that are based on mapping image features directly have been proposed instead [66, 77]. The volume rendering model is illustrated in Fig. 2.7. Rays are casted from each pixel in the view plane and the corresponding density evolution, which is the trilinearly interpolated voxel values along the ray, is used as a basis for the projection algorithm. Maximum value projection is a simple application, but tends to give noisy results in ultrasound data. Steen and Olstad [88] extended this method calculating the local gradients along the density evolution producing a transparent view of the data with emphasized structure boundaries. Surface shading is also possible with this method [78], but the quality of the result is very dependent on the boundary definitions in the ultrasound data. Volume rendering techniques are also discussed in Paper B, and examples of surface shaded cardiac valves are presented in Paper F and in Chapter 3.

- **Surface rendering.** Surface rendering of polygon data is well-known from computer graphics, and the principle is illustrated in Fig. 2.7. The object has a well-defined position in space, and is made up of a set of polygons with a known surface normal. This vector is used, together with the light source and the view point, to create a 2D projection. Advanced illumination models can be incorporated into this model creating realistic images. These techniques can be applied to medical data by extracting surfaces inside the data volume and converting them to a polygon representation. The surfaces are detected by automatic, semi-automatic, or manual contour detection algorithms. The polygon volume format is also practical for volume estimation algorithms, as is demonstrated for volume estimation of ultrasound data in Paper C and D.

Chapter 3

Clinical applications

In this chapter, examples of clinical applications of 3D ultrasound are given which are not covered in the papers. The examples are from applications that we have studied during the work of this thesis, and the chapter will not cover all fields of clinical 3D ultrasound. The main contributions in this thesis are in the field of obstetrics and gynecology and in cardiology. More references to clinical applications in various fields can be found in a review by Nelson and Pretorius [63].

3.1 Applications of 3D ultrasound in obstetrics and gynecology

A great deal of research has been put into the field of 3D ultrasound in obstetrics and gynecology (Ob/Gyn) in the past years. One of the few successful industrializations of ultrasound scanners dedicated to 3D imaging has been made for Ob/Gyn and related applications (Kretztechnik AG, Austria). Ultrasound 3D imaging of stationary structures is in principle easier compared to dynamic 3D imaging of cardiac structures. Still, problems due to fetal movement during acquisition or to contact between fetal structures and the placenta, reduce the quality of the 3D reconstructions. Advantages of 3D ultrasound compared to conventional 2D ultrasound as experienced by Merz et al. [59] were: 1) Better overview of the field of interest when several different 2D slices can be visualized simultaneously; 2) The whole data volume can be reviewed later by the same examiner or by another person; 3) The data can be visualized by volume rendering; and 4) Reduced scanning time.

3.1.1 Embryo and fetus

Brinkley et al. [16] showed early that fetal weight estimation was possible using a position locator system for 3D reconstruction. Later, mechanically tilted probes were introduced and successful volume visualizations of fetal structures including malfor-

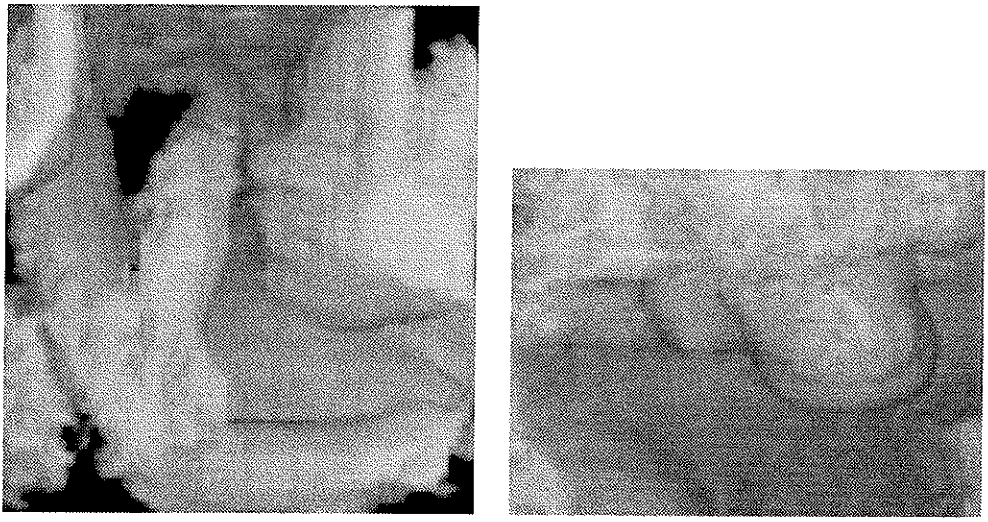
(a) (b)

Figure 3.1: (a) Face and part of one arm of a fetus. (b) "It's a boy!"

mations have been performed [45, 50, 88]. Merz et al. [59] scanned 204 patients with anomalies and found that 3D ultrasound was advantageous in demonstrating fetal defects in 62% of the cases. In 36%, the information was the same, and in 2% the 3D method was disadvantageous.

We showed previously that the volumes of embryonic brain cavities could be measured with 3D transvaginal ultrasound [15]. Later, we extended this technique by developing a dedicated transvaginal 3D ultrasound probe; this technique has been evaluated *in vitro* (Paper C), and *in vivo* (Paper D).

Fig. 3.1 shows two surface shaded images of parts of a fetus *in vivo*. The data were acquired using an abdominal probe mounted into a rotating motor device, and the reconstructions were performed on the EchoScan system (TomTec Inc.). The images were produced with 3D ultrasound technology in its early stages of development, and the quality of the renderings are improved with modern equipment. Still, the image in Fig. 3.1(a) illustrates two problems with fetal surface rendering: 1) Fetal movement during scanning, which can be seen by the blurred hand in front of the face; 2) Obstructing tissue, which can bee seen in the lower, left part of the image. This occurs when the fetus touches its surroundings.

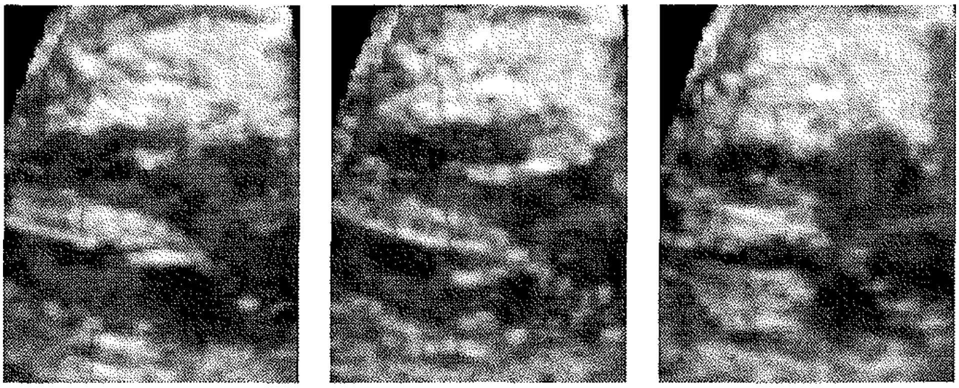

Figure 3.2: Preliminary results of dynamic 3D reconstruction of the fetal heart. The images show three slices through a fetal heart at different time positions in the cardiac cycle.

3.1.2 Fetal heart

As already mentioned, 3D acquisition of the fetal heart requires different cardiac gating methods than are required for the adult heart. The fetal heart is small (around 10 mm in diameter at 18 weeks' gestation and around 30 mm at 30 weeks), and the heart beat is fast (120-160 beats per minute). Studies have been reported where 3D acquisition of the fetal heart was performed without any cardiac gating [51, 97], but these reconstructions gave limited information compared to two-dimensional imaging.

Nelson et al. [64] presented a method for off-line fetal cardiac gating, where a position sensor was used in the acquisition. The probe was rotated slowly to cover the region of the fetal heart. To detect the position of the cardiac cycle, a synthetic M-mode line was extracted from the data passing through the moving valves. Fourier analysis was performed on these data and the regular movement of the valves was detected and used as the trigger positions. The reconstruction was then performed by reorganizing the data according to these trigger positions in a manner similar to adult dynamic 3D echocardiography. One limitation to this study was the temporal resolution given by the video output signal. Due to the high number of heart beats per minute, the temporal resolution in the 3D reconstructions should be 2–3 times as high for fetal hearts as it is for adult hearts.

In a preliminary study, we volume rendered the fetal heart for different positions during the cardiac cycle as shown in Fig. 3.2. The data were recorded with 104 frames/s which in this case corresponded to 45 volumes during one cardiac cycle. The fetus had reached 20 weeks of gestation. The recording was performed with a position sensor attached to the probe, which had a 5 MHz phased array transducer. The probe was swept slowly across the fetal heart and, unlike the method described by Nelson et al. [64], we found the trigger positions by manually selecting the start frames for each cardiac cycle based on the original 2D images. A future improvement of this technique is to detect the fetal ECG signal based on the maternal ECG [74]. The only requirement to this method is to detect a trigger position at each cardiac cycle occurring at the same relative position.

A fetal age of 18–22 weeks of gestation gives the best images for 3D reconstruction. The bone structures in the body is not too dominating, avoiding problems with shadowing artifacts, and the heart is enough developed to give clinical information. It is desirable to be able to detect cardiac disorders at an earlier stage, but the limited resolution of the ultrasound prevents details to be revealed. A review of different techniques for imaging the fetal heart with 3D ultrasound is given by Nelson [62].

3.1.3 Other applications

Kyei-Mensah et al. [49] used transvaginal 3D imaging to measure follicular volumes, and found that his 3D technique was more accurate than the conventional 2D ultrasound method. Jurkovic et al. [46] used the same acquisition technique for assessment of normal uterine anatomy and the diagnosis of congenital uterine anomalies. A similar method was used in Paper B, where 3D reconstruction of the endometrium was performed to improve distance and volume measurements, and to visualize anomalies.

3.2 Applications of dynamic 3D echocardiography

In the beginning of the 1970s, real-time 2D ultrasound imaging emerged as a new technique for diagnosing the heart. At the same time, attempts were made to reconstruct and visualize 3D ultrasound data of the heart. However, the relatively low computing power at that time limited the ability to visualize the 3D data, and as a consequence the first applications were volume estimation of the left ventricle which did not need any sophisticated visualization [32, 33, 56, 61, 83].

Successful volume visualizations of dynamic 3D echocardiographic data emerged in the late 1980s [57, 73, 76, 80]. It became possible to investigate cardiac disorders by visualizing the heart valves *in vivo* by non-invasive methods [79, 81]. Besides volume visualization, estimation of left ventricle volumes has been the most frequent application reported in the literature, and it has been shown that the accuracy of the estimates from 3D echocardiography are comparable to MR imaging methods [36, 44, 48, 65]. Other methods for quantification of the cardiac function have been reported. Wall motion analysis has been performed based on segmented gray-scale tissue data [29, 54]. Methods for quantification of blood volume flow have been presented based on a limited number of rotated 2D slices [72, 91, 92].

3.2.1 Valve surface visualization

As mentioned earlier, high temporal resolution is important in dynamic 3D reconstruction. We have shown that it was possible to reconstruct 3D data with as many as 200

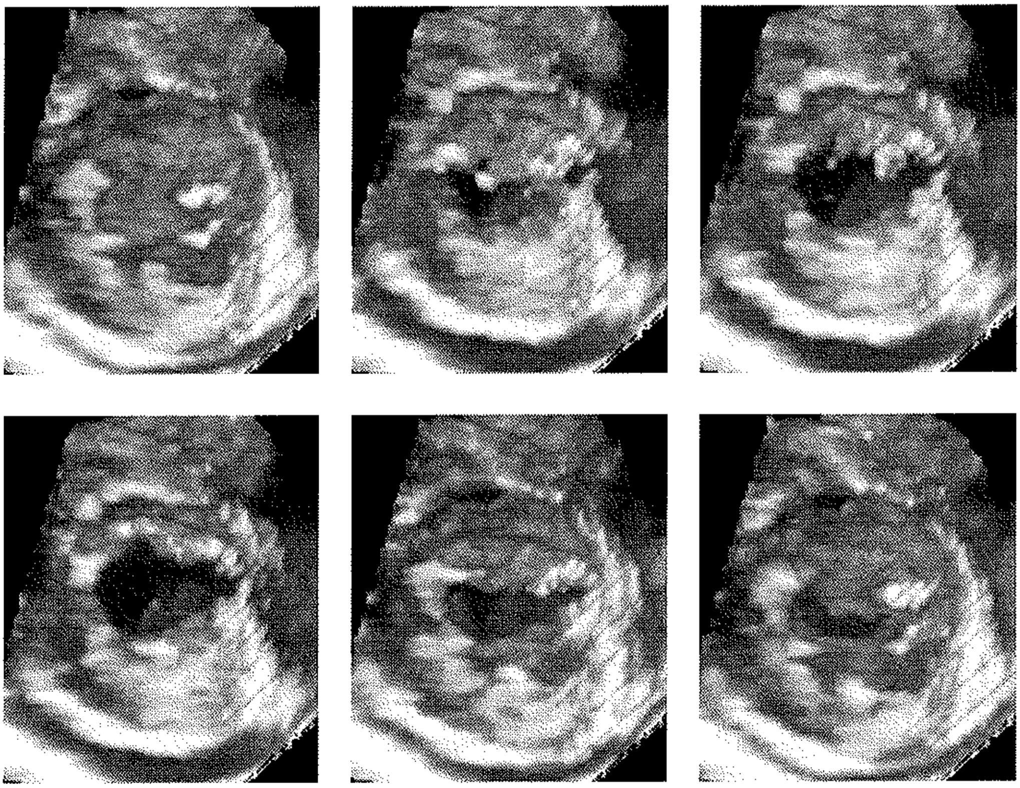

Figure 3.3: Surface visualization of the mitral valve seen from the left ventricle. The data consisted of a total of 60 volumes throughout the cardiac cycle. The six images represent the volumes number 10, 47, 48, 49, 1 and 8, from left–right, top–bottom.

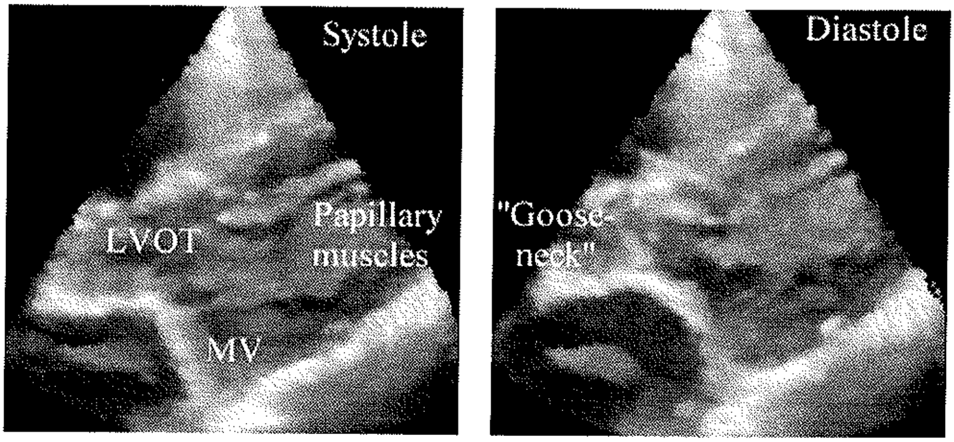

(a) (b)

Figure 3.4: The mitral valve and the left ventricle outflow tract (LVOT). (a) Systole. (b) Diastole. Dominating papillary muscles can bee seen, and the mitral valve creates a goose-neck (arrow).

frames/s, something that improves the reconstruction accuracy compared to video-based techniques. Fig. 3.3 shows six images of the mitral valve at different phases of a cardiac cycle. In this recording, the frame rate was 90 frames/s resulting in 60 volumes for a cardiac cycle. The valve is visualized from the left ventricle and no smoothing of the data has been performed.

Another patient example is given in Fig. 3.4, which shows the the mitral valve and the left ventricle outflow tract (LVOT) in systole and diastole. We see very dominating papillary muscles inside the left ventricle. In diastole, the mitral valve opens up and creates a so-called goose-neck which means that the leaflets unfolds into the LVOT as can be seen in Fig. 3.4(b).

3.2.2 Blood volume flow

Most of the work presented on 3D color flow imaging (CFI) has been qualitative, i.e., 3D visualization of color flow jets [3, 70]. Such techniques may give better understanding of a jet flow geometry and dynamics. The quality of the rendering is improved when raw digital data are used instead of video data. This is due to 1) the ability to process the tissue and the color flow data separately, and 2) the high frame rate of reconstruction. Fig. 3.5 shows three images of a mitral regurgitant jet during systole. The data are from the same patient as the surface visualization in Fig. 3.3. The images show the blood flow reversed back into the left atrium through the leaking mitral valve. The data were recorded with 45 frames/s.

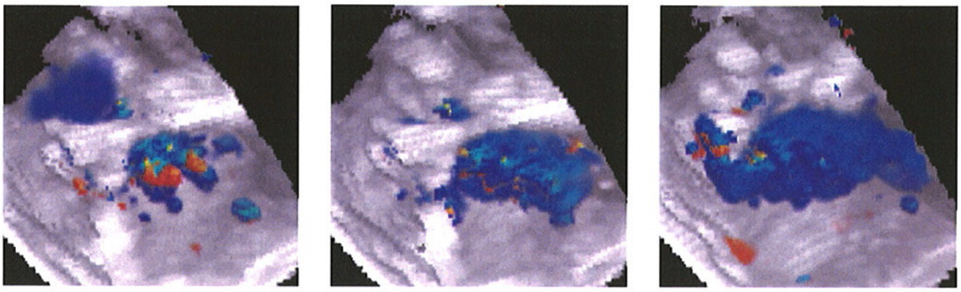

Figure 3.5: Rendering of mitral regurgitant jet at three time positions during the systole. The blue flow jet goes back into the left atrium through a dysfunctional mitral valve.

3.3 Other applications

3.3.1 Human tongue in motion

The tongue has a complex shape that varies with the different sounds. It has been difficult to visualize the shape of the tongue in three dimensions with current technology. MRI has been used, but it has been found difficult especially for dynamic 3D reconstruction. Three-dimensional ultrasound has been applied to phonetic research to visualize the human tongue [30, 90]. Surfaces of the tongue from different sounds were extracted from the 3D reconstructed data. The same sound was produced during each 3D acquisition.

Initial experiments with data acquisition and reconstruction of dynamic 3D ultrasound of the tongue have been performed. The aim of this work was to achieve surface visualization for a pronounced word rather than only a single vowel or consonant. The data acquisition was performed using a position sensor mounted on the ultrasound probe as previously described. The probe was placed underneath the jaw facing upwards. The scan plane was placed in either the saggital or the lateral direction. During acquisition, the probe was slowly tilted from one side to the other while a word was repeatedly pronounced. The head was placed in a stable position resting against a wall. The raw ultrasound data were recorded together with the spoken audio signal which was used as the reconstruction trigger signal. Similar to gating in 3D echocardiographic reconstruction, one trigger position was found in each cycle of the audio signal. The data representing the surface of the tongue were then extracted for each time step from the 3D data by manual segmentation. Fig. 3.6 shows three positions of a tongue pronouncing the Norwegian word “kakao”.

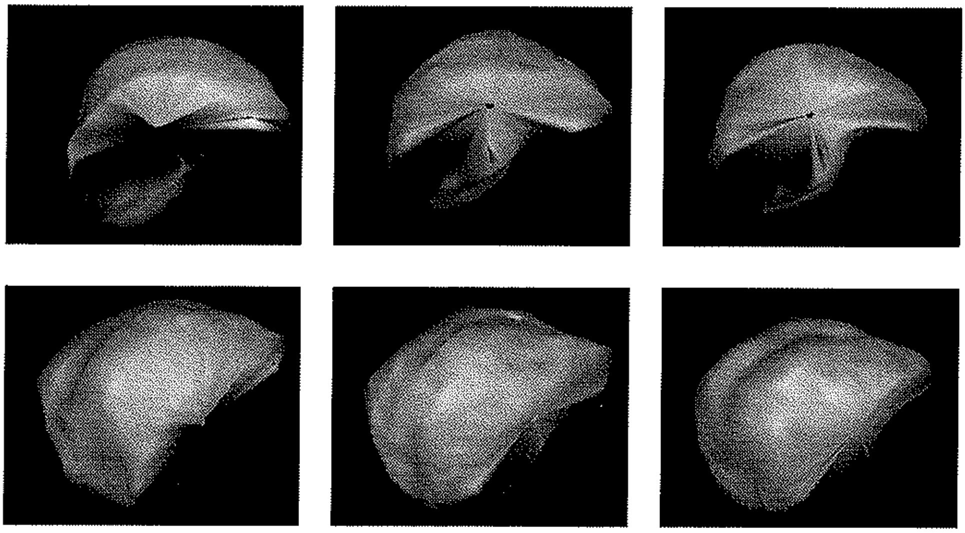

K··· ···*a*··· ···*kao*···

Figure 3.6: Visualization of the tongue during the pronunciation of the Norwegian word "kakao". Top row shows the tongue from the side with the tip at right. The bottom row shows the tongue from behind.

Chapter 4

Conclusions

The goal of this thesis was to develop and evaluate techniques that provide 3D ultrasound data with little loss of resolution compared to the original ultrasound data, and that perform precise quantitative analysis of such volumetric information.

Raw digital ultrasound tissue and Doppler data were used in most of the 3D reconstructions in this work. We showed that this had several advantages compared to using video-grabbed data, something that has been common for many of the 3D ultrasound methods presented so far. Using raw data, the temporal resolution from the original 2D scan planes was preserved in the dynamic 3D reconstructions of the heart. Reconstructions with a temporal resolution down to 5 ms was possible. This reduced the reconstruction jitter artifacts and made it possible to analyze rapidly moving heart valves.

Another consequence of using raw data was that the Doppler data were available for quantitative analysis. The tissue and Doppler components were processed separately to improve the flow region definition. It is difficult to get the original Doppler components and a good flow definition using video-grabbed data for 3D processing. We developed an angle-independent method for calculating the blood volume flow using dynamic 3D color flow data. The blood volume flow through the aortic annulus was calculated for each volume throughout the cardiac cycle and the cardiac output was estimated.

Rapid freehand acquisition of dynamic 3D ultrasound data was demonstrated using a magnetic positioning system. The data were acquired during 10–20 cardiac cycles. Compared to using ECG-gated rotating motors, this is a relatively short recording time. The reason why this short time could be achieved was that the probe was tilted across the heart without any ECG-gating while the patient held its breath. The positioning system made the movement flexible and a large part of the heart could be recorded. Volume reconstruction of a complete cardiac cycle was produced within 2 min after the raw data had been transferred from the ultrasound scanner. It was possible to do the recording and processing of the 3D data during the patient examination.

A method for volume measurement of small structures using 3D ultrasound was developed. The limited resolution of the ultrasound beam causes structures to be smeared out in the image. To compensate for this we incorporated the size of the beam in the volume calculations. According to water tank experiments this method was accurate, and the method was successfully used to measure the volume of embryonic structures *in vivo*.

4.1 Further work

One of the most promising acquisition techniques for 3D ultrasound is by using scanners with 2D arrays for real-time volumetric scanning. Currently, the image quality on such scanners is not satisfactory and much work has to be done to process the huge amount of data more efficiently. Poor temporal resolution and low sensitivity of the color flow signals on these scanners show that there are much room for improvements. The development of these techniques the past years indicates that these improvements will come. The methods for post-processing of the 3D data from 2D array scanners are much of the same as for 1D array scanners, so the methods presented in this work also apply for 2D array scanners.

We have shown that it was possible to produce 3D ultrasound data fast, with high resolution, and with the possibility of extracting quantitative information. However, there are still many challenges left to make 3D ultrasound an everyday clinical tool. The acquisition and visualization of the data should be completely integrated with the ultrasound scanner so that little extra effort is required to achieve the 3D images.

A great potential for quantitative analysis of 3D ultrasound data lies in combining information from different scanning modalities such as color flow imaging, tissue Doppler imaging, strain rate imaging or contrast imaging. Morphological information from tissue imaging can be combined with functional information from Doppler imaging and used in modeling of the cardiac function.

For fetal 3D ultrasound, further investigation can reveal anomalies at an early stage of embryonic development. Dynamic 3D reconstructions of the fetal heart can be improved with better cardiac gating. Using the fetal ECG is one possibility.

References

1. B. A. J. Angelsen. *Waves, signals and signal processing in medical ultrasonics. Volume I.* NTNU, Dept. of Physiology and Biomedical Engineering, The Norwegian University of Science and Technology (NTNU), Trondheim, Norway, 1995.

2. G. Baum, P. Chester, and I. Greenwood. Orbital lesion localization by three-dimensional ultrasonography. *New York State J Med*, 61:4149–4157, Dec. 1961.

3. M. Belohlavek, D. A. Foley, T. C. Gerber, et al. Three-dimensional reconstruction of color Doppler jets in the human heart. *J Am Soc Echocardiogr*, 7(6):553–560, 1994.

4. M. Belohlavek, D. A. Foley, T. C. Gerber, T. M. Kinter, J. F. Greenleaf, and J. B. Seward. Three- and four-dimensional cardiovascular ultrasound imaging: A new era for echocardiography. In *Mayo Clinic Proc.*, volume 68, pages 221–240, 1993.

5. S. Berg and B. Olstad. Evaluation of fuzzy neighborhood filters in medical imaging. In *Proc. of SPIE Medical Imaging*, volume 3034, pages 990–998, 1997.

6. S. Berg, S. Samstad, S. Bjærum, and H. Torp. Quantitative transthoracic three-dimensional (3D) color flow imaging: a new method applied to mitral blood flow. Presented at the 12th Symposium on Echocardiology and the 9th Meeting of the International Cardiac Doppler Society, Rotterdam, The Netherlands, June 1997.

7. S. Berg, S. Samstad, and H. Torp. Dynamic three-dimensional freehand echocardiography: high framerate transthoracic valve reconstruction. In *Supplement to Circulation*, volume 98, pages I–194, Oct. 1998.

8. S. Berg, A. H. Torp, K. P. Schipper, and B. Olstad. Quantitative wall motion coding in three-dimensional echocardiography. In *Proc. of SPIE Medical Imaging*, volume 2709, pages 424–432, Newport Beach, 1996.

9. S. Berg, A. H. Torp, K. P. Schipper, and B. Olstad. Real-time quantitative wall motion coding in two-dimensional echocardiography. In *Proc. of SPIE Medical Imaging*, volume 2709, pages 413–423, Newport Beach, 1996.

10. S. Berg and H. Torp. Volumetric blood flow estimation using dynamic three-dimensional ultrasound color flow imaging. In *Proc. of the IEEE Ultrasonics Symposium*, Sendai, Japan, 1998.

11. S. Berg, H. Torp, and H.-G. Blaas. Accuracy of in-vitro volume estimation of small structures using three-dimensional ultrasound. Submitted for publication, 1999.

12. S. Berg, H. Torp, B. O. Haugen, and S. Samstad. Volumetric blood flow measurement using dynamic three-dimensional ultrasound color flow imaging. Submitted for publication, 1999.

13. S. Berg, H. Torp, D. Martens, et al. Dynamic three-dimensional freehand echocardiography using raw digital ultrasound data. *Ultrasound Med Biol*, 25(5):745–753, 1999.

14. H.-G. Blaas, S. Eik-Nes, S. Berg, and H. Torp. In-vivo three-dimensional ultrasound reconstructions of embryos and early fetuses. *Lancet*, 352(9135):1182–1186, 1998.

15. H.-G. Blaas, S. Eik-Nes, T. Kiserud, S. Berg, B. Angelsen, and B. Olstad. Three-dimensional imaging of the brain cavities in human embryos. *Ultrasound Obstet Gynecol*, 5:228–232, Apr. 1995.

16. J. F. Brinkley, W. D. McCallum, S. K. Muramatsu, and D. Y. Liu. Fetal weight estimation from ultrasonic three-dimensional head and trunk reconstructions: Evaluation in vitro. *Am J Obstet Gynecol*, 144(6):715–721, 1982.

17. J. F. Brinkley, W. E. Moritz, and D. W. Baker. Ultrasonic three-dimensional imaging and volume from a series of arbitrary sector scans. *Ultrasound Med Biol*, 4(4):317–327, 1978.

18. R. Chiao, K. W. Rigby, and D. G. Wildes. Optimization of 1.5D arrays. In *Proc. of the IEEE Ultrasonics Symposium*, Sendai, Japan, 1998.

19. N. De Jong, K. Djoa, A. van der Steen, C. Lancee, J. Kasprazak, and N. Bom. Real-time three-dimensional data acquisition. In *Proc. of the IEEE Ultrasonics Symposium*, Sendai, Japan, Oct. 1998.

20. D. L. Dekker, R. L. Piziali, and E. Dong. A system for ultrasonically imaging the human heart in three dimensions. *Comput Biomed Res*, 7:544–553, 1974.

21. A. Delcker and H. C. Diener. 3D ultrasound measurement of atherosclerotic plaque volume in carotid arteries. *Bildgebung/Imaging*, 61(2):116–121, 1994.

22. P. R. Detmer, G. Bashein, T. Hodges, et al. 3D ultrasonic image feature localization based on magnetic scanhead tracking: in vitro calibration and validation. *Ultrasound Med Biol*, 20(9):923–936, 1994.

23. C. Di Mario, C. von Birgelen, F. Prati, et al. Three dimensional reconstruction of cross sectional intracoronary ultrasound: clinical or research tool? *Br Heart J*, 73:26–32, 1995.

24. I. Donald, J. MacVicar, and T. G. Brown. Investigation of abdominal masses by pulsed ultrasound. *Lancet*, 1:1188–1194, 1958.

25. D. B. Downey, D. A. Nicolle, M. F. Levin, and A. Fenster. Three-dimensional ultrasound imaging of the eye. *Eye*, 10:75–81, 1996.

26. R. A. Drebin, L. Carpenter, and P. Hanrahana. Volume rendering. *Computer Graphics (Proceedings of SIGGRAPH)*, 22(4):65–74, 1988.

27. I. Edler and C. H. Hertz. The use of ultrasonic reflectoscope for the continuous recording of movements of heart walls. *K Fysiogr Saellsk Lund F*, 24:1–19, 1954.

28. H. Feigenbaum. *Echocardiography*. Lea & Febiger, 5th edition, 1994.

29. D. Fine, D. Sapoznikov, M. Mosseri, and M. S. Gotsman. Three-dimensional echocardiographic reconstruction: qualitative and quantitative evaluation of ventricular function. *Comput Methods Programs Biomed*, 26:33–44, 1988.

30. A. K. Foldvik, U. Kristiansen, J. Kværness, A. H. Torp, and H. Torp. Three-dimensional ultrasound and magnetic resonance imaging: A new dimension in phonetic research. Int. Congress of Phon. Sciences, Stockholm, Aug. 1995.

31. J. D. Foley, A. van Dam, S. K. Feiner, and J. F. Hughes. *Computer graphics: principles and practice*. Addison-Wesley, 2nd edition, 1990.

32. E. A. Geiser, M. Ariet, D. A. Conetta, S. M. Lupkiewicz, L. G. Christie Jr, and C. R. Conti. Dynamic three-dimensional echocardiographic reconstruction of the intact human left ventricle: Technique and initial observations in patients. *Am Heart J*, 103(6):1056–1065, 1982.

33. E. A. Geiser, S. M. Lupkiewicz, L. G. Christie, M. Ariet, D. A. Conetta, and C. R. Conti. A framework for three-dimensional time-varying reconstruction of the human left ventricle: sources of error and estimation of their magnitude. *Comput Biomed Res*, 13:225–241, 1980.

34. A. Ghosh, N. C. Nanda, and G. Maurer. Three-dimensional reconstruction of echocardiographic images using the rotation method. *Ultrasound Med Biol*, 8(6): 655–661, 1982.

35. O. Gilja, A. Smievoll, N. Thune, et al. In vivo comparison of 3D ultrasonography and magnetic resonance imaging in volume estimation of human kidneys. *Ultrasound Med Biol*, 21(1):25–32, 1995.

36. A. S. Gopal, M. J. Schnellbaecher, Z. Shen, L. M. Boxt, J. Katz, and D. L. King. Freehand three-dimensional echocardiography for determination of left ventricular volume and mass in patients with abnormal ventricles: comparison with magnetic resonance imaging. *J Am Soc Echocardiogr*, 10(8):853–861, Oct. 1997.

37. U. M. Hamper, V. Trapanotto, S. Sheth, M. R. DeJong, and C. I. Caskey. Three-dimensional US: Preliminary clinical results. *Radiology*, 191(2):397–401, 1994.

38. L. Hatle and B. Angelsen. *Doppler ultrasound in cardiology: Physical principles and clinical applications.* Lea & Febiger, 2nd edition, 1985.

39. A. Heimdal, A. Støylen, H. Torp, and T. Skjærpe. Real-time strain rate imaging of the left ventricle by ultrasound. *J Am Soc Echocardiogr*, 11(11):1013–1019, 1998.

40. J. H. Hokland and T. Taxt. Ultrasound speckle reduction using harmonic oscillator models. *IEEE Trans Ultrason Ferrelec Freq Contr*, 41(2):215–224, Mar. 1994.

41. S. Holm, B. Elgetun, and G. Dahl. Properties of the beampattern of weight- and layout-optimized sparse arrays. *IEEE Trans Ultrason Ferrelec Freq Contr*, 44(5): 983–991, Sept. 1997.

42. D. H. Howry and W. R. Bliss. Ultrasonic visualization of the soft tissue structures of the body. *J Lab Clin Med*, 40:579–592, 1952.

43. D. H. Howry, G. Posakony, C. R. Cushman, and J. H. Holmes. Three-dimensional and stereoscopic observation of body structures by ultrasound. *J Appl Physiol*, 9: 304–306, Sept. 1956.

44. S. W. Hughes, T. J. D'Arcy, D. J. Maxwell, et al. Volume estimation from multiplanar 2D ultrasound images using a remote electromagnetic position and orientation sensor. *Ultrasound Med Biol*, 22(5):561–572, 1996.

45. A. D. Hull and D. H. Pretorius. Fetal face: what we can see using two-dimensional and three-dimensional ultrasound imaging. *Semin Roentgenol*, XXXIII(4):369–374, Oct. 1998.

46. D. Jurkovic, A. Geipel, K. Gruboeck, E. Jauniaux, M. Natucci, and S. Campbell. Three-dimensional ultrasound for the assessment of uterine anatomy and detection of congenital anomalies: a comparison with hysterosalpingography and two-dimensional sonography. *Ultrasound Obstet Gynecol*, 5:233–237, Apr. 1995.

47. C. Kasai, K. Namekawa, A. Koyano, and R. Omoto. Real-time two-dimensional blood flow imaging using an autocorrelation technique. *IEEE Trans Sonics Ultrason*, SU-32(3):458–464, May 1985.

48. I. Kupferwasser, S. Mohr-Kahaly, P. Stähr, et al. Transthoracic three-dimensional echocardiographic volumetry of distorted left ventricles using rotational scanning. *J Am Soc Echocardiogr*, 10:840–852, 1997.

49. A. Kyei-Mensah, J. Zaidi, R. Pittrof, A. Shaker, S. Campbell, and S.-L. Tan. Transvaginal three-dimensional ultrasound: accuracy of follicular volume measurements. *Fertil Steril*, 65(2):371–376, 1996.

50. A. Lee, A. Kratochwil, J. Deutinger, and G. Bernaschek. Three-dimensional ultrasound in diagnosing phocomelia. *Ultrasound Obstet Gynecol*, 5:238–240, Apr. 1995.

51. M. Levental, D. H. Pretorius, M. S. Sklansky, N. E. Budorick, T. R. Nelson, and K. Lou. Three-dimensional ultrasonography of normal fetal heart: comparison with two-dimensional imaging. *J Ultrasound Med*, 17:341–348, 1998.

52. M. Levoy. Display of surfaces from volume data. *IEEE Computer Graphics and Applications*, pages 29–37, Aug. 1988.

53. T. Lie, A. Kleven, Å. Grønningsæter, G. Unsgård, F. Lindseth, and T. E. Aarseth. Interactive, wand-driven stereoscopic visualization of 3D ultrasound brain data. Video presentation at the Second congress of International Society for Neurosurgical Instrument Inventors, Berlin, Germany, July 1997.

54. J. Mæhle, K. Bjoernstad, S. Aakhus, H. G. Torp, and B. A. J. Angelsen. Three-dimensional echocardiography for quantitative left ventricular wall motion analysis. *Echocardiography Am Jrnl of CV Ultrasound & Allied Tech*, 11(4):397–408, 1994.

55. R. W. Martin, G. Bashein, P. R. Detmer, and W. E. Moritz. Ventricular volume measurement from a multiplanar transesophageal ultrasonic imaging system: An in vitro study. *IEEE Trans Biomed Eng*, 37(5):442–449, 1990.

56. M. Matsumoto, M. Inoue, S. Tamura, K. Tanaka, and H. Abe. Three-dimensional echocardiography for spatial visualization and volume calculation of cardiac structures. *J Clin Ultrasound*, 9:157–165, 1981.

57. H. A. McCann, J. C. Sharp, T. M. Kinter, C. N. McEwan, C. Barillot, and J. F. Greenleaf. Multidimensional ultrasonic imaging for cardiology. *Proceedings of the IEEE*, 76(9):1063–1073, 1988.

58. M. B. McNay and J. E. E. Flemming. Forty years of obstetric ultrasound 1957–1997: from A-scope to three dimensions. *Ultrasound Med Biol*, 25(1):3–56, 1999.

59. E. Merz, F. Bahlmann, and G. Weber. Volume scanning in the evaluation of fetal malformations: a new dimension in prenatal diagnosis. *Ultrasound Obstet Gynecol*, 5:222–227, Apr. 1995.

60. K. Miyatake, M. Yamagishi, N. Tanaka, et al. New method for evaluating left ventricular wall motion by color-coded tissue Doppler imaging: in vitro and in vivo studies. *J Am Coll Cardiology*, 25(3):717–24, 1995.

61. W. E. Moritz, A. S. Pearlman, D. H. Mc Cabe, D. K. Medema, M. D. Ainsworth, and M. S. Boles. An ultrasonic technique for imaging the ventricle in three dimensions and calculating its volume. *IEEE Trans Biomed Eng*, 30(8):482–492, 1983.

62. T. R. Nelson. Three-dimensional fetal echocardiography. *Prog Biophys Mol Biol*, 69:257–272, 1998.

63. T. R. Nelson and D. H. Pretorius. Three-dimensional ultrasound imaging. *Ultrasound Med Biol*, 24(9):1243–1270, 1998.

64. T. R. Nelson, D. H. Pretorius, M. Sklansky, and S. Hagen-Ansert. Three-dimensional echocardiographic evaluation of fetal heart anatomy and function: acquisition, analysis and display. *J Ultrasound Med*, 15:1–9, 1996.

65. Y. F. M. Nosir, P. M. Fioretti, W. B. Vletter, et al. Accurate measurement of left ventricular ejection fraction by three-dimensional echocardiography. *Circulation*, 94(3):460–466, Aug. 1996.

66. B. Olstad. Maximizing image variance in rendering of volumetric data sets. *Journal of Electronic Imaging*, 1(3):256–265, 1992.

67. B. Olstad, S. Berg, A. Torp, K. Schipper, and S. Eik-Nes. 3D transvaginal ultrasound imaging for identification of endometrial abnormality. In *Proc. of SPIE Medical Imaging*, volume 2432, pages 543–553, San Diego, 1995.

68. R. Omoto, M. Matsumura, S. Kyo, et al. Real-time three-dimensional ultrasound system without reconstruction process: feasibility for application in mitral valve disease. In *Supplement to Circulation*, volume 98, pages I–226, Oct. 1998.

69. J. Pan and W. J. Tompkins. A real-time QRS detection algorithm. *IEEE Trans Biomed Eng*, BME-32(3):230–236, 1985.

70. P. A. Picot, D. W. Rickey, R. Mitchell, R. N. Rankin, and A. Fenster. Three-dimensional colour Doppler imaging. *Ultrasound Med Biol*, 19(2):95–104, 1993.

71. I. Pitas and A. N. Venetsanopoulos. *Nonlinear digital filters. Principles and applications.* Kluwer Academic Publishers, 1990.

72. J. K. Poulsen and W. Y. Kim. Measurement of volumetric flow with no angle correction using multiplanar pulsed Doppler ultrasound. *IEEE Trans Biomed Eng*, 43(6):589–599, 1996.

73. J. S. Raichlen, S. S. Trivedi, G. T. Herman, M. G. Sutton, and N. Reichek. Dynamic three-dimensional reconstruction of the left ventricle from two-dimensional echocardiograms. *J Am Coll Cardiology*, 8(2):364–370, 1986.

74. M. Richter, T. Schreiber, and D. T. Kaplan. Fetal ECG extraction with nonlinear state-space projections. *IEEE Trans Biomed Eng*, 45(1):133–137, Jan. 1998.

75. D. E. Robinson. Display of three-dimensional ultrasonic data for medical diagnosis. *J Acoust Soc Am*, 52(2):673–687, 1972.

76. J. Roelandt, A. Salustri, and B. Mumm. Precordial three-dimensional echocardiography with a rotational imaging probe. *Echocardiography Am Jrnl of CV Ultrasound & Allied Tech*, 12(3):243–252, 1995.

77. P. Sabella. A rendering algorithm for visualizing 3D scalar fields. *Computer Graphics (Proceedings of SIGGRAPH)*, 22(4):51–58, Aug. 1988.

78. G. Sakas, L.-A. Schreyer, and M. Grimm. Preprocessing and volume rendering of 3D ultrasonic data. *IEEE Computer Graphics and Applications*, pages 47–54, July 1995.

79. A. Salustri, A. E. Becker, L. Van Herwerden, W. B. Vletter, F. J. Ten Cate, and J. R. T. C. Roelandt. Three-dimensional echocardiography of normal and pathologic mitral valve: a comparison with two-dimensional transesophageal echocardiography. *J Am Coll Cardiology*, 27(6):1502–1510, 1996.

80. A. Salustri and J. Roelandt. Three dimensional reconstruction of the heart with rotational acquisition: methods and clinical applications. *Br Heart J*, 73:10–15, 1995.

81. A. Salustri, S. Spitaels, J. McGhie, W. Vletter, and J. R. T. C. Roelandt. Transthoracic three-dimensional echocardiography in adult patients with congenital heart disease. *J Am Coll Cardiology*, 26(3):759–767, 1995.

82. S. Satumora. Ultrasonic Doppler method for the inspection of cardiac function. *J Acoust Soc Am*, 29:1181–1185, 1957.

83. H. Sawada, J. Fujii, K. Kato, M. Onoe, and Y. Kuno. Three dimensional reconstruction of the left ventricle from multiple cross sectional echocardiograms. *Br Heart J*, 50:438–442, 1983.

84. T. Shiota, M. Jones, M. Chikada, et al. Real-time three-dimensional echocardiography for determining right ventricular stroke volume in an animal model of chronic right ventricular volume overload. *Circulation*, 97:1897–1900, 1998.

85. T. Shiota, B. Sinclair, M. Ishii, et al. Three-dimensional reconstruction of color Doppler flow convergence regions and regurgitant jets: an in vitro quantitative study. *J Am Coll Cardiology*, 27(6):1511–1518, 1996.

86. S. A. Slørdahl, S. Berg, A. Støylen, S. Samstad, and H. Torp. Left ventricular volumes from three-dimensional echocardiography by rapid freehand scanning using digital scan line data. Presented at the XXth Congress of The European Society of Cardiology, Vienna, Austria, Aug. 1998.

87. S. W. Smith, H. G. Pavy Jr., and O. T. von Ramm. High-speed ultrasound volumetric imaging system–Part I: transducer design and beam steering. *IEEE Trans Ultrason Ferrelec Freq Contr*, 38(2):100–108, 1991.

88. E. Steen and B. Olstad. Volume rendering of 3D medical ultrasound data using direct feature mapping. *IEEE Trans on Medical Imaging*, 13(3):517–525, Sept. 1994.

89. E. N. Steen. *Analysis and visualization of multi-dimensional medical images.* PhD thesis, Dept. of Computer Systems and Telematics, Norwegian Institute of Technology, 1996.

90. M. Stone and A. Lundberg. Three-dimensional tongue surface shapes of English consonants and vowels. *J Acoust Soc Am*, 99(6):3728–3737, 1996.

91. Y. Sun, P. Ask, B. Janerot-Sjöberg, L. Eidenvall, D. Loyd, and B. Wranne. Estimation of volume flow rate by surface integration of velocity vectors from color Doppler images. *J Am Soc Echocardiogr*, 8(6):904–914, 1995.

92. H. Tsujino, E. Shiki, M. Hirama, and K. Iinuma. Quantitative measurement of volume flow rate (cardiac output) by the multibeam Doppler method. *J Am Soc Echocardiogr*, 8(5):621–630, 1995.

93. M. Vogel, S. Y. Ho, K. Bühlmeyer, and R. H. Anderson. Assessment of congenital heart defects by dynamic three-dimensional echocardiography: methods of data acquisition and clinical potential. *Acta Paediatr Suppl*, 410:34–39, 1995.

94. O. T. von Ramm, S. W. Smith, and H. G. Pavy Jr. High-speed ultrasound volumetric imaging system–Part II: parallel processing and image display. *IEEE Trans Ultrason Ferrelec Freq Contr*, 38(2):109–115, 1991.

95. P. N. T. Wells. The present status of ultrasonic imaging in medicine. *Ultrasonics*, 31(5):345–352, 1993.

96. J. J. Wild and J. M. Reid. Echographic visualization of lesions of the living intact human breast. *Cancer Res*, 14:277–283, 1954.

97. N. Zosmer, D. Jurkovic, E. Jauniaux, K. Gruboeck, C. Lees, and S. Campbell. Selection and identification of standard cardiac views from three-dimensional volume scans of the fetal thorax. *J Ultrasound Med*, 15:25–32, 1996.

Paper A

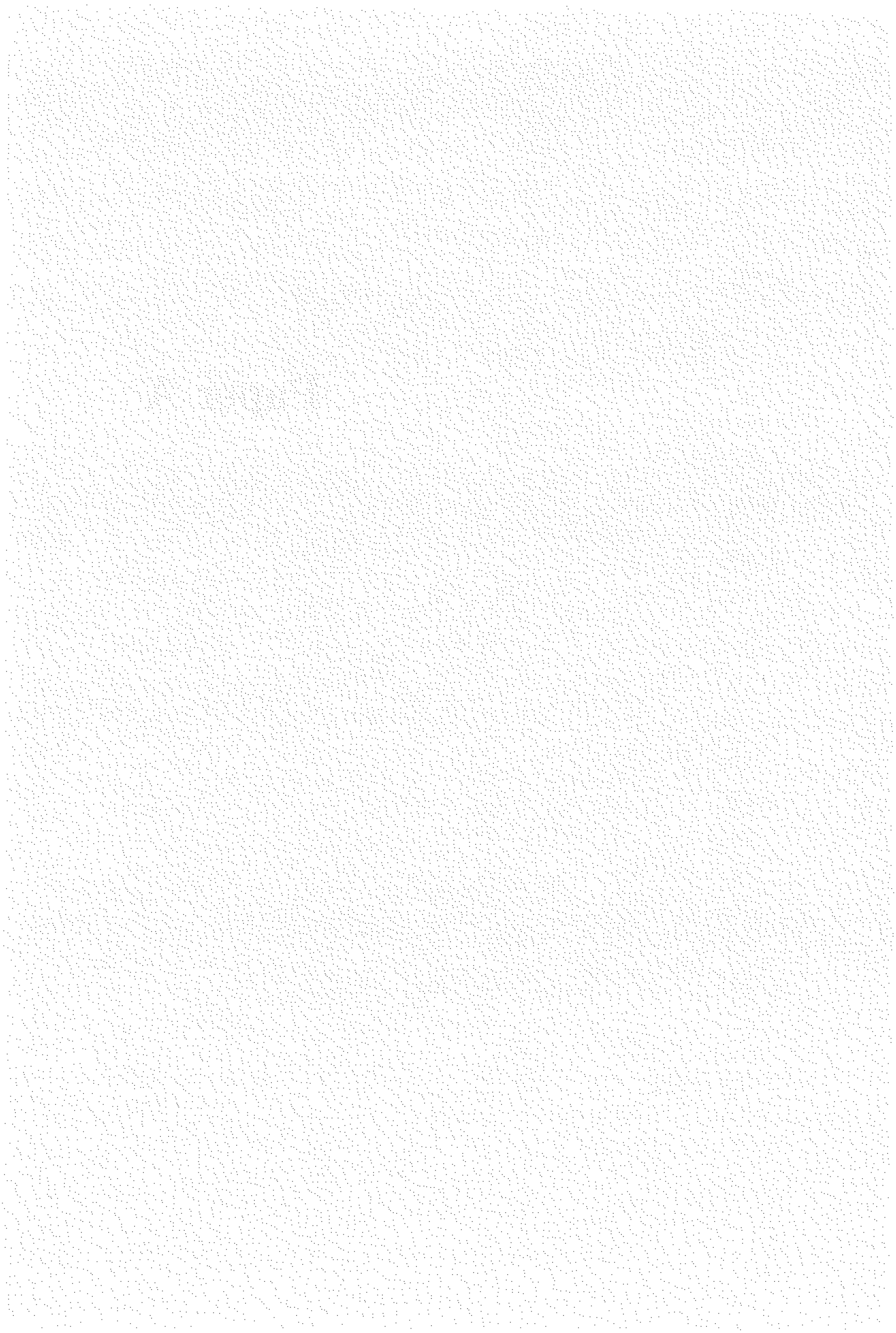

Fuzzy connected neighborhood filters

Sevald Berg and Bjørn Olstad

Dept. of Computer and Information Science,
Norwegian University of Science and Technology,
Trondheim, Norway

Abstract

In this paper we describe the framework of a new class of nonlinear digital filters based on fuzzy connected neighborhoods. An introduction to fuzzy neighborhoods is given, and two types of filters are developed. The framework is adapted to different image types, consisting of natural images, medical ultrasound images and multi-spectral images. We discuss the underlying definition of the distance metric in the given applications and appropriate hard constraints in the extraction of pixel neighborhoods. The fuzzy neighborhood approach offers more flexibility in the design of the filter and in the stability of the filtering process. The fuzzy connected neighborhood filters can perform strong filtering and still maintain fine, thin structures without blurring edges.

Based on *"Evaluation of fuzzy neighborhood filters in medical imaging"*
In *Proc. of SPIE Medical Imaging*, 3034:990–998, 1997

1 Introduction

Most image filter designs are based upon the moving window concept with a predefined filter mask. These filters will operate on the same pixels relative to the filter pixel and can only to a small extent take into account the local image content. It is desirable to have a filter with the ability to smooth image noise without degrading structures. In order to do this we introduce a framework based on *fuzzy connected neighborhoods* that incorporates the specific local image structure for each pixel. The concept of fuzzy neighborhoods is taken from the theoretic and algorithmic framework given by Udupa and Samarasekera [9] and Steen [7]. In these works, the method is used for fuzzy segmentation of medical images and volumes.

We apply the fuzzy connected neighborhood filters on images of different types and look at the filter properties. We use synthetic and natural images, and images from different medical imaging modalities. The filters can be used to improve edge detection algorithms in for example noisy ultrasound images where we want to track endocardial walls or heart valves. They also serves as smoothing filters for volume rendering applications. The edge preserving capabilities can be used to make spatio-temporal filters for ultrasound video sequences. In multi-spectral imaging like MRI a multi-spectral definition of the distance metric can be used in the filtering process.

We start by defining the fuzzy connected neighborhood and show how it is used in image filtering. We then briefly analyze the filter performance and discuss its relation to other filters. Finally, we show how the filter can be used in different medical imaging settings.

2 Definitions

We will use the fuzzy region growing method given by Steen [7] as a basis for our definitions. The theory of fuzzy objects and fuzzy regions introduces a range of related concepts. We will refer to the final result as a fuzzy connected neighborhood. Having computed a fuzzy connected neighborhood, we can use it in different image processing applications like filtering, edge detection and segmentation.

Udupa and Samarasekera [9] based their general framework for fuzzy object definition on the theory of fuzzy sets. This theory makes it possible to define fuzzy objects in a general N-dimensional space. This is demonstrated useful in segmentation of MR-images and as a basis for the definition of the interactive edge-detection algorithms called live-wire and live-lane [4].

Steen [7] described similar concepts, but with a simpler framework. The fundamental concepts are the notion of connectivity between pixels, and the existence of paths of pixels based on cost-functions. The definitions and discussions are based on pixels defined in a two-dimensional (2D) uniform grid, but can be extended into a three-dimensional (3D) volume with no loss of generality. Each pixel or voxel are associated with an attribute vector $\boldsymbol{A}$. Typical examples of pixel attributes are gray level values or multi-spectral values (as in color images).

DEFINITION 2.1 (K-NEAREST NEIGHBORS) In 2D, a pixel p has four horizontal and vertical nearest neighbors called *4-nearest neighbors*, denoted $N_4(p)$. Including the diagonal neighbors gives the *8-nearest neighbors*, or the *8-neighborhood*, $N_8(p)$. In 3D, a voxel v can have up to 26 nearest neighbors, $N_{26}(v)$. ■

DEFINITION 2.2 (K-CONNECTIVITY) Two pixels p and q are *K-connected* if they are K-nearest neighbors and if $\boldsymbol{A}(p) \in C$ and $\boldsymbol{A}(q) \in C$, where $\boldsymbol{A}$ is an attribute vector associated with each pixel, and C is a set of attribute values defining the connectivity. ■

DEFINITION 2.3 (K-PATH) A K-path between two pixels $p(x, y)$ and $q(s, t)$ is a sequence of distinct pixels with coordinates $(x_0, y_0), \ldots, (x_n, y_n)$ where $(x_0, y_0) = (x, y)$, $(x_n, y_n) = (s, t)$ and (x_{i-1}, y_{i-1}) is K-connected with (x_i, y_i) where $i \in \{1 \ldots n\}$. ■

The previous definitions make a very strict classification of which pixels to be included in a path or not. In order to take into account mixed distributions and to create a more fuzzy pixel selection, we use the notion of *weight* between two pixels. There is a certain cost related to the inclusion of pixels in a neighborhood.

DEFINITION 2.4 (WEIGHTED K-CONNECTIVITY) Any two pixels p and q that are K-neighbors are K-connected with a weight $w_M(p, q) \in \boldsymbol{R}^+$. ■

The M indicates material dependency, and is in practice dependent on the pixel attribute vectors and also possibly on the pixel coordinate values. The weight w_M can not be negative, and it decreases when the probability that the pixels are connected increases.

DEFINITION 2.5 (WEIGHTED K-PATH) A weighted K-path P between two pixels p_1 and p_n is a sequence of distinct pixels $p_1 \ldots p_n$, where p_{i-1} is weighted K-connected with p_i, $i \in \{2 \ldots n\}$. ■

DEFINITION 2.6 (PATH WEIGHT) The weight $w(P)$ of a path P is a function $f \in \boldsymbol{R}^+$ of the weights along the path. ■

The total path weight function f must be monotonically increasing with the length of the path. One function that has been found to be useful [7], is given by:

$$w(P) : f(w_M(p_1, p_2), \ldots, w_M(p_{n-1}, p_n)) = (\sum_{i=1}^{n-1} w_M(p_i, p_{i+1})^\gamma)^{\frac{1}{\gamma}}. \tag{1}$$

Here, p is the path elements. For $\gamma = 1$ the weight of the path is simply the sum of the weights along the path. Increasing γ will result in a stronger influence by the maximal weights.

DEFINITION 2.7 (MINIMUM WEIGHT PATH) In the set $Y(p_1, p_n)$ of all possible paths connecting p_1 and p_n there are at least one path with minimum weight, $\delta(Y(p_1, p_n))$. This minimum weight defines the weight of the connection between p_1 and p_n:

$$\delta(Y(p_1, p_n)) = \min_{P \in Y(p_1, p_n)} w(P). \tag{2}$$

■

We will now use this minimum weight path to define the fuzzy connected neighborhood. Actually, the fuzzy connected neighborhood of a pixel p_1 consists of all the pixels in the minimum weight path from p_1 to p_n. An important property of this set of values is that it is an ordered set. The weight $w(P)$ will increase monotonically as new elements are included in the neighborhood.

The choice of weight function clearly depend on the application of the fuzzy connected neighborhood. Steen [7] was concerned with segmentation of medical images and defined a weight function that was based on the distribution of the image pixels:

$$w_M(p, q) = 1.0 - e^{\frac{\|(\tilde{q}+\tilde{p})\cdot\frac{1}{2}-\mu\|^2}{\Sigma}}. \tag{3}$$

The values $\tilde{q}$ and $\tilde{p}$ are the image pixels convolved with a Gaussian kernel. The mean μ and the covariance matrix Σ can be computed by training or taken directly from a sample of the image (inside the area of segmentation). This has shown to give good results in segmenting medical ultrasound images. We are in this paper concerned with image filtering, and we propose two simple weight functions that are well-suited to our filter framework. The first function use the intensity value difference between two consecutive pixels in the path, while the second uses the difference between the first and the last pixel.

$$w_{prev}(P) = \left(\sum_{i=1}^{n-1} w_{prev}(p_{i+1}, p_i)^2\right)^{\frac{1}{2}} = \left(\sum_{i=1}^{n-1} (\boldsymbol{A}_I(p_{i+1}) - \boldsymbol{A}_I(p_i))^2\right)^{\frac{1}{2}}. \tag{4}$$

$$w_{orig}(P) = \left(\sum_{i=1}^{n-1} w_{orig}(p_{i+1}, p_1)^2\right)^{\frac{1}{2}} = \left(\sum_{i=1}^{n-1} (\boldsymbol{A}_I(p_{i+1}) - \boldsymbol{A}_I(p_1))^2\right)^{\frac{1}{2}}. \tag{5}$$

The attribute $\boldsymbol{A}_I$ denotes the pixel intensity value. We will extend these weight functions when applying the paths in different applications in Section 4. In order to find the minimum weight path between two pixels, i.e., to minimize Eq. (4) and (5), we use the Dijkstra algorithm [2]. This algorithm guarantees to find the shortest path between two elements in a weighted, directed graph. The weights must be nonnegative. In a typical application using pixels (or voxels) on a rectangular grid as vertices, and a K-neighborhood in a weighted K-path as edges, this can be regarded as a weighted, directed graph. A general solution of this algorithm can be solved in $O(V \log V + E)$ time [2], where V is the number of vertices and E is the number of edges. When using the fact that if the edge weights are integer values in the range $0 \ldots w_{Max}$, Ahuja et al. [1] reported a running time of $O(E + V\sqrt{\log w_{Max}})$. If we in addition map the minimum path weights to discrete values in the range $0 \ldots \delta_{\mathrm{Max}}$, Steen [7] reported a running time of $O(4V)$.

From the definitions, the number of elements n in such a path will be limited only by the total number of elements. We must put some constraints on this number. For a path P with elements $(p_1, \ldots, p_n)$ satisfying Eq. (2) we may use the constraints given below. We will later discuss the use of these constraints and different weight functions in practical examples.

CONSTRAINT 2.1 $\delta(Y(p_1, p_n)) \leq \delta_{\mathrm{Max}}$
The δ_{Max} is a threshold that sets an upper bound on the weight function. If it costs to much to include a pixel it is not considered a neighbor. This maximal cost can also be measured between elements p_{n-1} and p_n. ■

CONSTRAINT 2.2 $n < N$
The number N sets an upper limit for how many elements to be included in a neighborhood. ■

CONSTRAINT 2.3 $\| \boldsymbol{\xi}_{p_1} - \boldsymbol{\xi}_{p_i} \| \leq D_{\mathrm{Max}} \;\; \forall p_i \in P$
$\boldsymbol{\xi}_{p_i}$ is the coordinate for element p_i. The constant D_{Max} is the maximum spatial deviation. This constraint prevents the neighborhood to grow outside the spatial mask defined by D_{Max}. ■

The above definitions have given us a flexible tool for designing fuzzy connected neighborhoods. Different weight functions and constraints can be used depending on the actual application. In Fig. 1 we show the neighborhoods of two adjacent pixels in the Lena image. The black pixel is the first element of the path (p_1), and the path contains 35 pixels. The two pixels are located near an edge, so the two neighborhoods contain pixels from each side of the edge and do not overlap. This is an important property: the region will prefer to grow into areas similar to the first element. The cost of including an edge pixel can be high. By using the previously mentioned constraints, we can force the region to act in a certain way.

PROPERTY 2.1 By not putting any constraint on the maximal number of elements in the path (Constr. 2.2), the fuzzy connected neighborhood will reduce to a $(2 \cdot D_{\mathrm{Max}} + 1) \times (2 \cdot D_{\mathrm{Max}} + 1)$ square mask according to Constr. 2.3. ■

PROPERTY 2.2 The difference of using the weight functions from Eq. (4) and (5) is that the w_{orig} function will result in a neighborhood with pixels as close to the first pixel as possible. The w_{prev} function will allow the pixels to follow an intensity trend in the image. ■

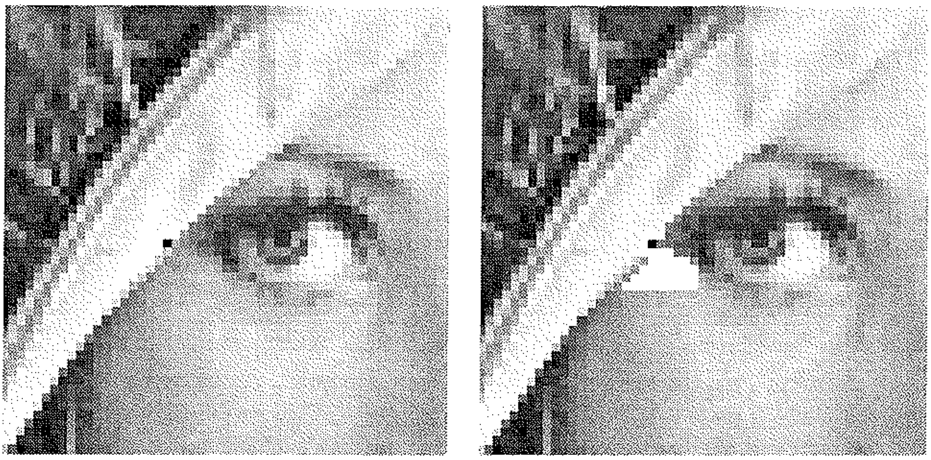
(a) (b)

Figure 1: Fuzzy connected neighborhood of two adjacent pixels. The neighborhood contains 35 pixels, and the weight function in Eq. (5) is used.

PROPERTY 2.3 In order to reduce the computational complexity we can use a N_4 neighborhood instead of a full N_8 neighborhood. The path will not be optimal, but in practice the differences are small. ■

3 Fuzzy connected neighborhood filters

The fuzzy connected neighborhood we defined in the previous section defines the filter window. But unlike the normal $N \times N$ moving window, the fuzzy connected neighborhood window will be different for each pixel in the image. It changes according to the underlying structure in the image, and the idea is that the filter estimate will be based on the neighbor values that resembles the current pixel. We would then expect to have a filter that is to a great extent edge preserving even when filtering with a big window. The fuzzy connected neighborhood will also vary according to the constraints mentioned earlier.

We now have to decide what form the filter function must have in order to take advantage of the fuzzy connected neighborhood window. We propose two techniques: the average filter and the regression filter.

3.1 Average filter

The most straightforward filter function to use is to average the filter values, creating the fuzzy neighborhood average filter (FNA-filter). Since the filter values are a minimum weight path, the effect of an average operation will be quite different from a normal moving window average filter. For a fuzzy connected neighborhood P with pixel values $(p_1, \ldots, p_n)$, the filter has the following form:

$$\hat{p}_1 = \frac{\sum_{i=1}^{n} (p_i \cdot w_U(p_i))}{\sum_{i=1}^{n} w_U(p_i)}. \tag{6}$$

Here, $\hat{p}_1$ is the filter estimate. The values $w_U(p_i)$ are user-defined weights that make it possible to increase the influence of for example the closest pixels in the neighborhood. The default value for this weight is 1, resulting in a simple average function. We can also weight the filter estimate with the Dijkstra distance d_i which is the minimum weight values for each element in the ordered set P:

$$\hat{p}_1 = \frac{\sum_{i=1}^{n} (p_i \cdot w_U(p_i) \cdot e^{-\beta \cdot d_i^2})}{\sum_{i=1}^{n} (w_U(p_i) \cdot e^{-\beta \cdot d_i^2})}. \tag{7}$$

The value β is a constant. The influence from the filtering values will now decrease exponentially with the Dijkstra distance.

3.2 Regression filter

The fuzzy neighborhood regression filter (FNR-filter) is a trend-preserving filter for 2D images, using the multiple linear regression model based on the least-squares estimate [3]. We calculate a regression plane in the fuzzy connected neighborhood using the pixel intensity values. The reason that we can use this model is that our filter window consists of pixels that most likely belongs to the same image structure. If this structure is not constant but involves an intensity change or trend, the regression filter will produce an estimate in conjunction with this trend. Using an average function may produce an incorrect answer, as shown in the 1D example in Fig. 2.

The regression model uses the fuzzy connected neighborhood with pixel values $(p_1, \ldots, p_n)$ and the corresponding coordinates $\boldsymbol{\xi}_{p_i} = (x_i, y_i)$, and is given by the following set of equations:

$$\begin{pmatrix} p_1 \\ p_2 \\ \vdots \\ p_n \end{pmatrix} = \begin{pmatrix} 1 & x_1 & y_1 \\ 1 & x_2 & y_2 \\ \vdots & \vdots & \vdots \\ 1 & x_n & y_n \end{pmatrix} \begin{pmatrix} b_1 \\ b_2 \\ \vdots \\ b_n \end{pmatrix} + \begin{pmatrix} \epsilon_1 \\ \epsilon_2 \\ \vdots \\ \epsilon_n \end{pmatrix}, \tag{8}$$

or equivalently:

$$\boldsymbol{p} = \boldsymbol{X}\boldsymbol{b} + \boldsymbol{\epsilon}, \tag{9}$$

where $\boldsymbol{p}$ is the pixel values, $\boldsymbol{X}$ is the design matrix with the pixel coordinates, $\boldsymbol{b}$ is the plane equation coefficients and $\boldsymbol{\epsilon}$ is the vector of errors. Based on our fuzzy neighborhood values we can now estimate the values $\boldsymbol{b}$ and use them to calculate

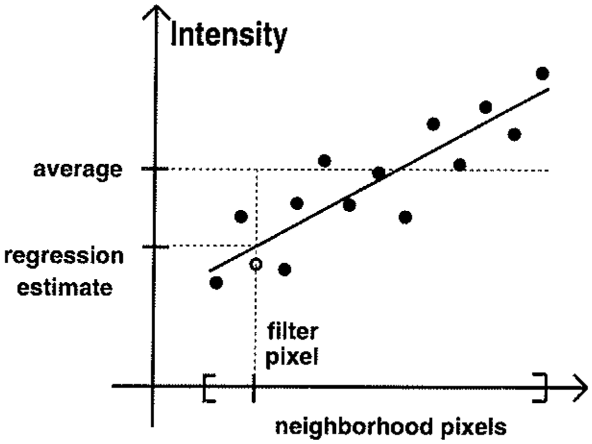

Figure 2: A 1D example showing that the regression filter may produce a better estimate since it takes into account intensity trends.

the estimated value for the pixel p_1. The least-squares estimate $\hat{\boldsymbol{b}}$ for the equation coefficients are then given by the following equation:

$$\hat{\boldsymbol{b}} = (\boldsymbol{X}'\boldsymbol{X})^{-1}\boldsymbol{X}'\boldsymbol{p} = \boldsymbol{X}^{+}\boldsymbol{p}, \tag{10}$$

where $\boldsymbol{X}'$ is the transpose of $\boldsymbol{X}$, and $\boldsymbol{X}^{+}$ is the pseudo-inverse matrix for $\boldsymbol{X}$. This is only valid when the matrix $\boldsymbol{X}'\boldsymbol{X}$ is nonsingular. When the fuzzy connected neighborhood pixel values form a straight line in the intensity space, this matrix will be singular and we can not make an estimate. We may choose not to filter in that situation. The regression filter can be reduced to one dimension as shown in Fig. 2, or to two dimensions as used in our experiments. In the latter case we calculate the filter value by solving the plane equation:

$$\hat{p}_1 = \hat{b}_0 + \hat{b}_1 x_1 + \hat{b}_2 y_1, \tag{11}$$

where $\hat{\boldsymbol{b}} = [\hat{b}_0, \hat{b}_1, \hat{b}_2]'$ and (x_1, y_1) is the coordinate for pixel p_1. The filter can also be applied to 3D data.

4 Applications

4.1 General considerations

One important property for our filters is that they can do very strong filtering and still be able to maintain fine structures in the images. As shown below, neighborhoods with up to 60 pixels can be used without degrading the image too much. In addition, the

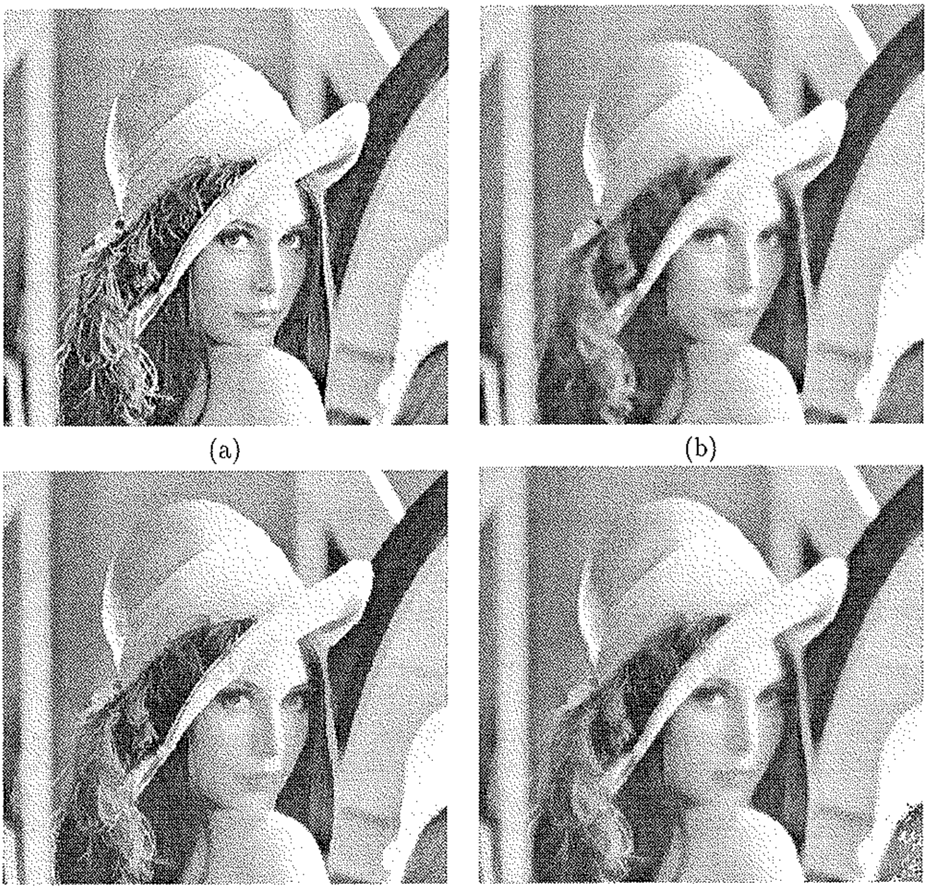

(a) (b) (c) (d)

Figure 3: (a) The original Lena image. (b) Median filtered with 5x5 mask. (c) FNA filtered. (d) FNR filtered.

FNR filter is intensity trend preserving. This means that when the intensity changes monotonically in the picture, the filter will smooth these structures accordingly.

We now apply the filters with large filter masks so that the filter properties can be examined. In Fig. 3(a) we see the original Lena image at resolution 256x240 pixels. In Fig. 3(b) we have applied a median filter with a 5x5 filter mask. The strongest edges were well preserved, but image details were gone because of blurring. In Fig. 3(c) we have applied an FNA filter on the original image. The weight function according to Eq. (5) was used. There were 60 pixels in the filter mask, and the maximum allowed deviation was 11x11 pixels (filter window). Even though this was a very large filter mask, there was not much blurring. The fine structures and the edges were preserved. The reason was that in this noise-free image the neighborhoods will contain pixels that are similar to each other. The filtering was performed based on the underlying structural information.

In Fig. 3(d) we have applied an FNR filter on the original image. The same filter parameters as the FNA filter above was used except that the neighborhood contained only 50 pixels. This filter performed more smoothing than the FNA filter. But it was still able to preserve fine structures. The filter is intensity trend preserving and will smooth the image according to the intensity changes. It will not create streaking which is common in other types of filters.

4.2 Gaussian and impulsive noise

In this section we will look at how the filters respond to image noise both with a synthetic image and the Lena image. Fig. 4(a) shows a synthetic image corrupted by impulse noise. The noise probability was 0.13. In Fig. 4(b) we have applied a 3x3 median filter, and in Fig. 4(c) an FNA filter with a 10 pixel neighborhood, 11x11 window mask, a weight function according to Eq. (4), and α-trimmed so that the first 4 pixels are removed from the neighborhood. We can see that the FNR filter removed all impulses except from one situation where the impulse pixels were situated just beside a step edge. Then the neighborhood evolved into the side similar to the impulse, and the impulse was not removed. This error will be less significant when the image contains more than two gray levels.

In Fig. 5(a) we see the Lena image corrupted with additive white Gaussian noise with standard deviation 25. In Fig. 5(b) the image was filtered with an FNR filter with 40 pixels in the neighborhood, an 11x11 window mask, and a weight function according to Eq. (5). The image noise was smoothed and still the image was not blurred. The fine structures and the edges were well preserved. This is confirmed by the plots in Fig. 5(c) and (d), where the horizontal line no. 90 of the original image is plotted against the Gaussian noise image and the FNR filtered image respectively. The signal-to-noise ratio (SNR) is often used to quantify filter performance. The difference in SNR between a median filtered and a FNR filtered noise image (Fig. 5(a)) is small. However, the qualitative appearance is clearly different. The FNR filter appears sharper with the noise smoothed.

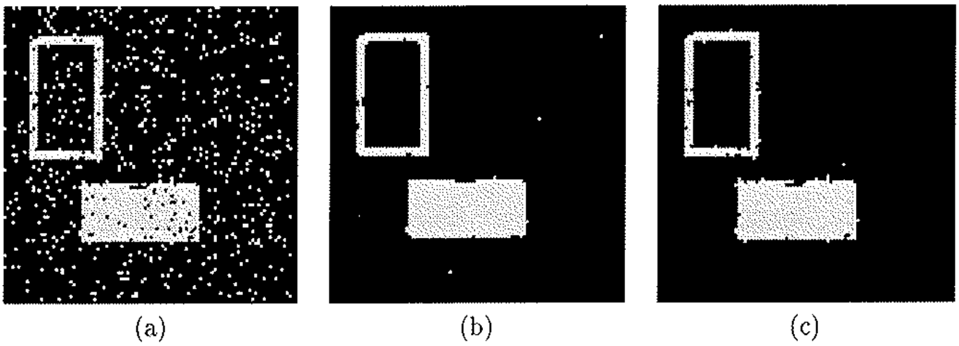

Figure 4: (a) Image with impulsive noise, (b) Median filtered, (c) α-trimmed FNA filtered

4.3 Medical ultrasound

Fig. 6(a) shows an ultrasound image of the left ventricle of the heart with resolution 118x157 pixels. In Fig. 6(b) we have used a 4x4 median filter, in Fig. 6(c) an anisotropic filter [5, 6] according to the nonlinear signal-adaptive anisotropic diffusion model given by Steen [7]. In Fig. 6(d) we used an FNR filter with $N = 40$, maximum deviation 4, and the weight function given by Eq. (1) with $\gamma = 2$. We can see that the anisotropic and FNR filters do not blur the edge. The FNR filter tends to smooth the structures more than the anisotropic filter. The latter creates harder edges.

4.4 Multi-spectral data

So far, we have applied the filters on gray scale images only. However, the fuzzy neighborhood scheme is well suited for images containing multi-valued components, using a multi-spectral definition of the underlying distance metric. In Fig. 7 we show an example of filtering of a MR image of a human brain. The image consisted of three components which were coded as RGB values. Each of these components were filtered separately with a FNA filter before they were mapped back into RGB. An alternative approach is to use the Mahalanobis distance measure to exploit the correlation between the individual multi-spectral components [8].

5 Discussion

We have presented a nonlinear digital filter that uses a fuzzy neighborhood as the filter mask. The filter is defined in a general framework that can incorporate different filter designs. We have described a variant of the average filter and a regression filter. These filters are shown to be well-suited with the fuzzy neighborhood mask. The framework allows for a flexible design of filters in N dimensions and for multi-attribute images. We have discussed the use of the filter in different medical imaging applications. One

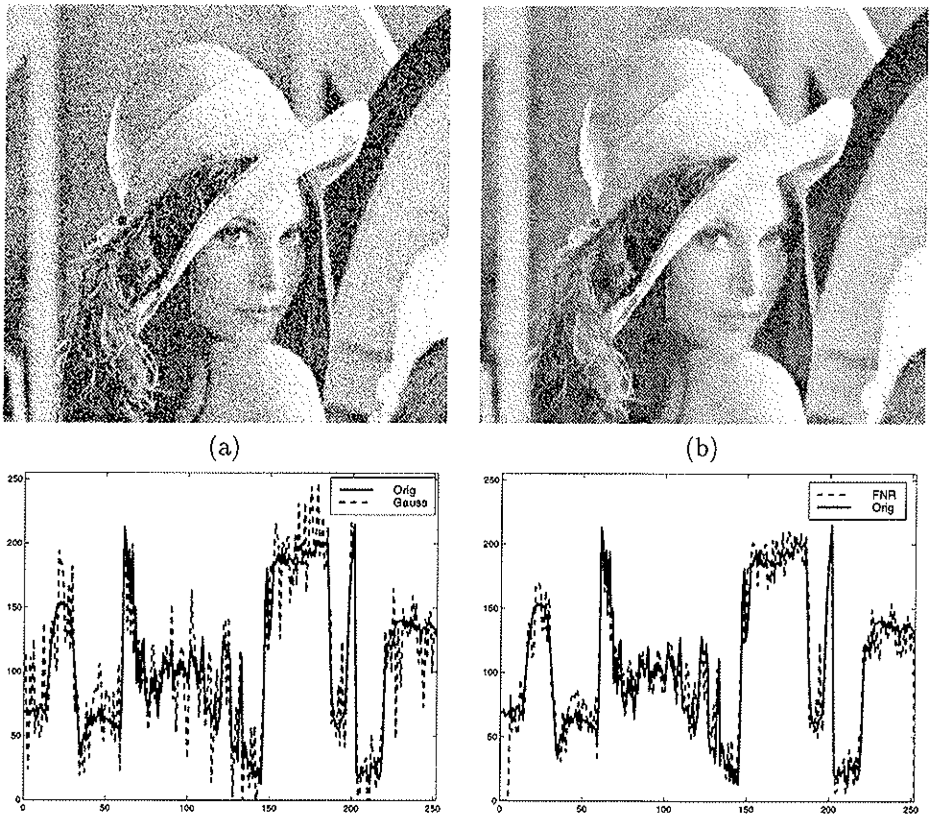

(a) (b)

(c) (d)

Figure 5: (a) Lena with Gaussian noise. (b) FNR filtered. (c) Line 90 of original image (solid) and noise (dotted). (d) Line 90 of original image (solid) and FNR filtered image (dotted).

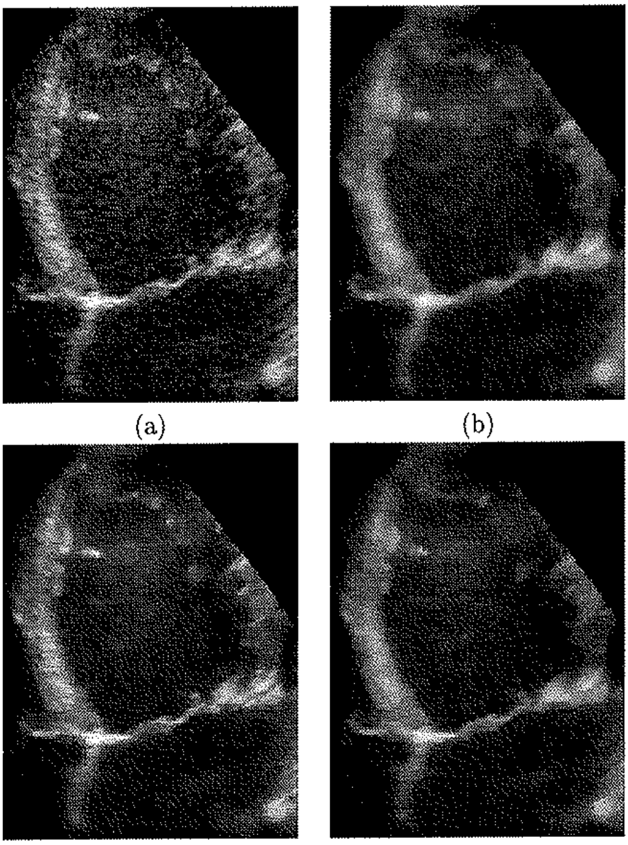

(a) (b)

(c) (d)

Figure 6: Ultrasound image of the heart. (a) The original image. (b) Median filtered. (c) Anisotropic diffusion filtered. (d) FNR filtered.

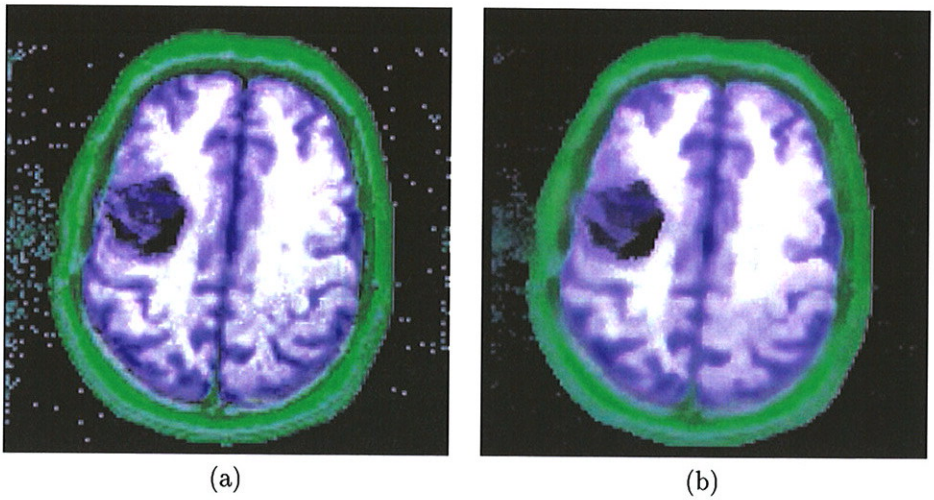

Figure 7: Multi-spectral MR image of a brain with tumor. (a) The original image. (b) FNA filtered image where each color coded component is filtered separately.

important property of the filter is that we can do strong filtering and still maintain thin, fine structures in the image. The regression filter also take into account intensity trends in the image, and filter accordingly.

A comparative study between the presented filters and common filter techniques is required to evaluate the filter performance. Both quantitative measures such as SNR and qualitative evaluation should be performed. Regarding the complexity of the filter algorithms, we have that the run-time changes with a constant factor of the size of the filter region. However, the complexity should be further measured and evaluated.

References

1. R. K. Ahuja, K. Mehlhorn, J. B. Orlin, and R. E. Tarjan. Faster algorithms for the shortest path problem. *Journal of the ACM*, 37(2):213–223, 1990.

2. T. H. Cormen, C. E. Leiserson, and R. L. Rivest. *Introduction to algorithms.* MIT Press, 1992.

3. E. R. Dougherty. *Probability and statistics for the engineering, computing and physical sciences.* Prentice Hall, 1990.

4. A. X. Falcao et al. User-steered image boundary segmentation. In *Proc. of SPIE Medical Imaging*, volume 2710, 1996.

5. G. Gerig, O. Kübler, and F. A. Jolesz. Nonlinear anisotropic filtering of MRI data. *IEEE Trans on Medical Imaging*, 11(2):221–232, 1992.

6. P. Perona and J. Malik. Scale-space and edge detection using anisotropic diffusion. *IEEE Trans on Pattern Analysis and Machine Intelligence*, 12(7):629–639, 1990.

7. E. N. Steen. *Analysis and visualization of multi-dimensional medical images.* PhD thesis, Dept. of Computer Systems and Telematics, Norwegian Institute of Technology, 1996.

8. T. Taxt, J. Olavsdottir, and M. D. hlen. Recognition of handwritten symbols. *Pattern Recognition*, 23:1155–1166, 1990.

9. J. K. Udupa and S. Samarasekera. Fuzzy connectedness and object definition. *Proc. of SPIE Medical Imaging*, 2431:2–10, 1995.

Paper B

3D transvaginal ultrasound imaging for identification of endometrial abnormality

Bjørn Olstad, Sevald Berg, Anders H. Torp,
Klaus P. Schipper[†] and Sturla H. Eik-Nes[‡]

Dept. of Computer Systems and Telematics,
The Norwegian Institute of Technology, Trondheim, Norway
[†]Cardiology Section,
Trondheim University Hospital, Trondheim, Norway
[‡]National Center for Fetal Medicine,
Trondheim University Hospital, Trondheim, Norway

Abstract

A multi-center study has previously evaluated the use of two-dimensional transvaginal ultrasound (TVS) to measure the thickness of the endometrium as a risk indicator for endometrial abnormality in women with postmenopausal bleeding. In this paper we present methods using three-dimensional TVS in order to improve the measurement, shape analysis and visualization of the endometrium. Active contour techniques are applied to identify the endometrium in a 3D dataset. The shape of the endometrium is then visualized and utilized to do quantitative measurements of the thickness. The voxels inside the endometrium are volume rendered in order to emphasize inhomogeneities. Since these inhomogeneities can exist both on the outside and the inside of the endometrium, the rendering algorithm has a controllable opacity function. A three-dimensional distance transform is performed on the data volume measuring the shortest distance to the detected endometrium border for each voxel. This distance is used as a basis for opacity computations which allows the user to emphasize on different regions of the endometrium. In particular, the opacity function can be computed such that regions that violate the risk indicator for the endometrium thickness are highlighted.

In *Proc. of SPIE Medical Imaging*, 2432:543–553, 1995

1 Introduction

The endometrium is the inner surface of the uterus. Observing the endometrium is important for several clinical reasons. Among these is to discover abnormalities by observing endometrial growth and textural changes for women with postmenopausal bleeding. Thickness or irregularity of the endometrium can be a risk indicator for pathological lesions such as hyperplasia, polyps and tumors [3, 10, 16, 29]. Several studies have evaluated the importance of endometrial thickness as a risk indicator for abnormalities for women with postmenopausal bleeding. A Scandinavian multi-center study involving 1168 women concluded that the probability of endometrial abnormality was 5.5 % when the endometrial thickness was less than 4 mm [16]. Granberg et al. [13] showed endometrial thickness of 18.2 ± 6.2 mm for women with endometrial cancer as compared to 3.2 ± 1.2 mm for women with atrophic endometrium. For premenopausal women, a normal thickness value is 8.6 ± 3.5 mm [1]. The study of endometrial development during normal cycles can improve the in-vitro-fertilization (IVF) method [11, 17]. Analyzing the contents of the endometrium after an abortion improves the safety for the patient.

Much interest has been drawn towards the use of ultrasound as a clinical tool for evaluating the endometrium. This offers a method less invasive than dilatation and curettage (D&C) or histological dating [20]. Avoiding the use of these methods reduces unnecessary risks for the patient and lowers the costs of the hospital procedures involved. Many studies have evaluated the use of 2D transabdominal and transvaginal ultrasound methods for analyzing the endometrium. Today, these methods are established clinical procedures.

Recently, the field of 3D and 4D ultrasound has attracted much interest in both technical [24–26, 30–32, 35, 40] and clinical [5, 6, 9, 12, 14] research. Currently, several commercial 3D systems are available [33]. These systems have been applied in several clinical areas including fetal medicine and cardiology. The purpose of this study was to apply 3D transvaginal ultrasound methods for characterization of the endometrium. Our goal has been to:

1. Develop reliable methods for 2D measurements by allowing the user to position the 2D image arbitrarily in a 3D scene relative to a geometrical rendering of the shape of the endometrium. In this way the user can verify that exaggerated distances due to inclined 2D planes are avoided. In addition, the 3D geometrical description of the endometrium is utilized directly in automated shape characterization.

2. Reveal new information to the clinician by supplying methods for visualizing the endometrial texture and form. In this way polyps, tumors and other growing structures can be displayed in relation to the endometrium and the uterus in 3D.

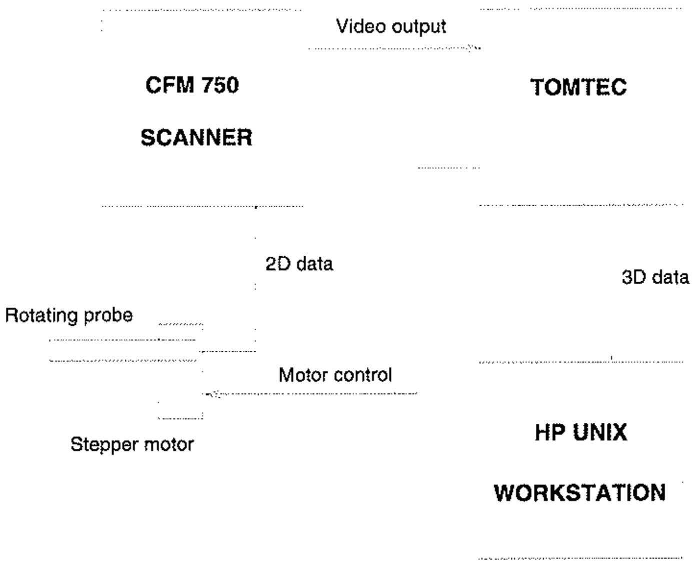

Figure 1: The environment for acquisition of 3D ultrasound images.

2 Methods

2.1 Data acquisition

The data was collected using a 2D sector scanner (CFM-750 from Vingmed Sound), with a mechanical 7.5 MHz annular array transvaginal transducer. The transducer was attached to a rotating stepper motor coupled to a PC-based TomTec Echo-Scan unit (see Fig. 1). During a period of 5 seconds the stepper motor rotated the transducer 180 degrees. During this period a complete 3D scan consisting of 132 two-dimensional sector images rotated around the central axis of the transducer were acquired. Fig. 2 illustrates how the resulting cone with acquired 3D data is related to the uterus. Fig. 3(a) shows one of the 2D sector images that was acquired during the 3D acquisition. Fig. 3(b) is an enlargement of the endometrium inside the uterus in Fig. 2. The output video signal from the Vingmed scanner was frame-grabbed by the TomTec unit during the acquisition. The images were then scan-converted into a regular, isotropic volumetric dataset. We will refer to this dataset as the *cuberille* which consists of volume elements or *voxels* that hold interpolated values in the regions between the captured sector images. The spatial dimension of the cuberille was 256 × 256 × 256. The cuberille data was transferred to a UNIX workstation running AVS, a general purpose computer graphics system from Advanced Visualization Systems, where all the processing described in this work has been implemented.

Normally, movement of the imaged object during the acquisition period can cause motion artifacts in the reconstructed cuberille data. It is, for example, vital that the

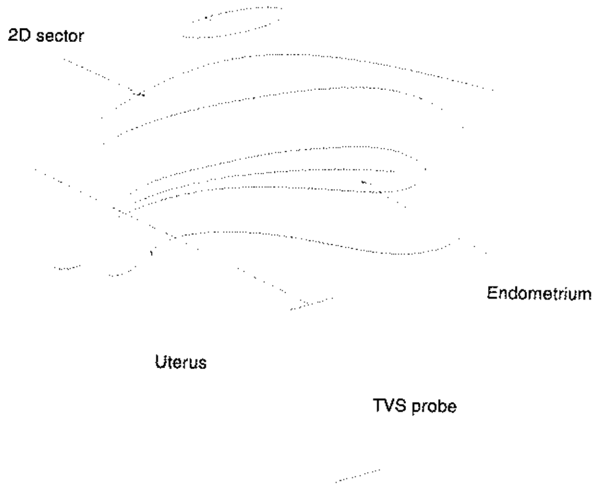

Figure 2: Position of the transducer and acquired cone with 3D ultrasound data relative to the uterus.

fetus doesn't move during a 3D fetal examination. These motion artifacts will appear as geometrical distortions and blurred structures in the 3D renderings that are generated. In contrast to 3D ultrasound in fetal examinations, movement of the imaged objects can be avoided in 3D TVS of the endometrium. The investigation can easily be redone, and the whole endometrium can normally be covered by a single scan. However, during the scan, the transducer must be kept stable either by a steady hand or a special device.

2.2 Edge detection

The endometrium and the myometrium of the uterus are usually distinguishable, as in Fig. 3(a). We have utilized this property to develop semi-automatic edge detection facilities that allow the user to effectively identify the 3D geometry of the endometrium. It should be noted that the echogenicity, size and form of the endometrium varies between individuals, during the menstrual cycles and during the life cycle of a given individual. The endometrium can also contain pieces of the placenta left from a birth or polyps of different sizes and echogenicities. The edge detection environment was made *semi*-automatic due to these observations and the fact that reliable edge detection in ultrasonic images is considered a difficult task due to the presence of severe noise sources and image artifacts such as image dropouts caused by shadowing.

Fig. 4(a) illustrates the edge detection process. The user indicates an approximate outline of the border of the endometrium. This outline is processed with active contour algorithms [2, 23, 27] in order to accurately align it with the underlying image content. As the user moves to neighboring 2D slices, the contour from the previous edge detection result is copied and readjusted to the new 2D image. The user can

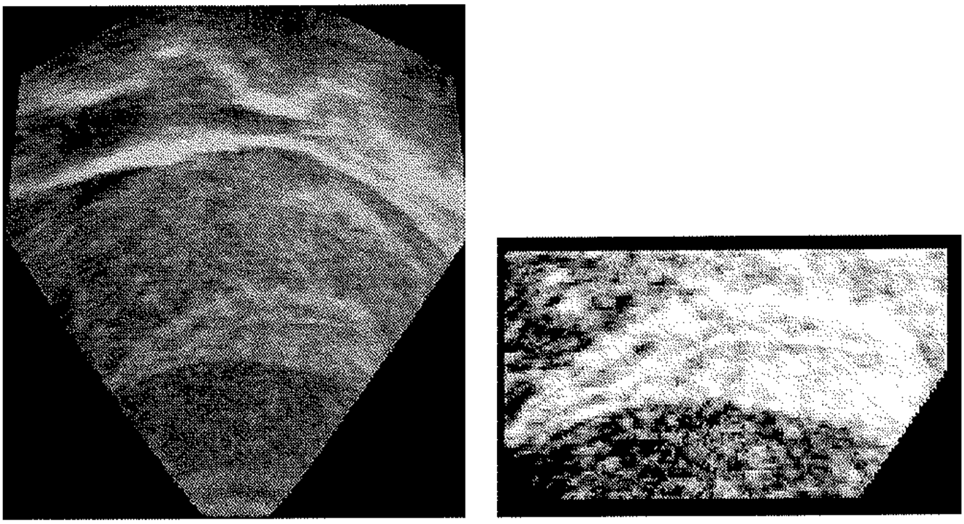
(a) (b)

Figure 3: (a) One of the original 2D slices in the 3D acquisition. (b) An enlargement of the endometrium from (a)

at any time interrupt the process and correct the contour detection. The resulting environment allows for reliable and efficient extraction of a 3D surface representation of the endometrial boundary. Fig. 4(b) shows a surface shading of the endometrial boundary that has been extracted from 3D TVS with the method described here.

2.3 Measurements

Measuring the thickness using 2D TVS can lead to erroneous results since we are not guaranteed that the measurement is done perpendicular to the endometrium. Performing this in 3D, it is much easier to verify that the thickness value is correct. Fig. 5(a) shows how a 2D slice is arbitrarily positioned in the 3D scene and related to the 3D shape of the endometrium extracted in the previous step. In this way, the user can easily verify that the 2D slice is correctly located relative to the endometrium and the resulting slice can then be used for the traditional 2D measurements. Fig. 5(b) illustrates a cut of the endometrium after the 2D slice has been correctly adjusted in 3D.

Thickness measurements can also be performed directly on the 3D surface description of the endometrial boundary. Using the geometric object resulting from the edge tracing routine, we can automatically calculate the thickness value. An AVS module has been developed that receives mouse input from the user telling where the thickness should be calculated. The AVS geometry object representing the endometrial boundary is a collection of points that are combined in a number of polyhedrons which make

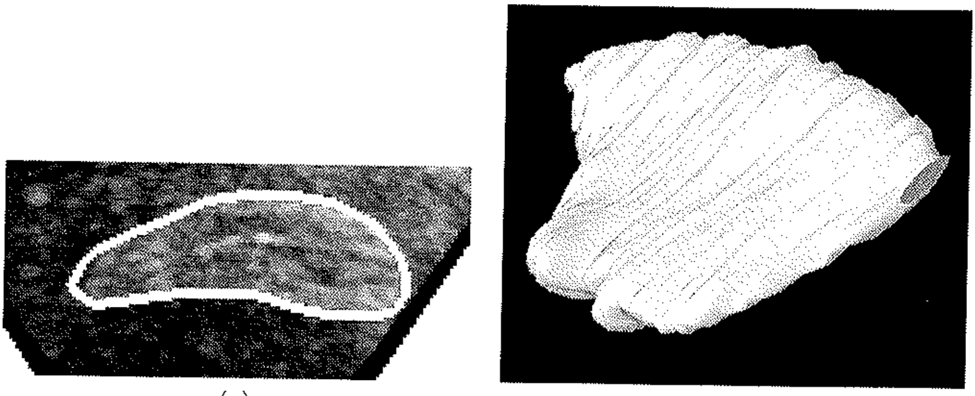
(a) (b)

Figure 4: (a) Active contours applied to the semi-automatic extraction of the endometrium. (b) Visualization of the endometrial boundary obtained by integrating the contours obtained in the edge detection illustrated in Fig. 3(a).

up the surface. By taking a number of normal vectors in a small area around the point on the endometrium surface indicated by the user, we calculate the average vector and define this as the direction vector perpendicular to the surface. This surface normal vector is searched in order to find two points of interception with the geometric object. The line connecting these two points are visualized in the 3D scene and the associated thickness is computed.

The previous discussion indicated how earlier measurement procedures developed for 2D imaging can be made more reliable by 3D validation of the relative orientation between the endometrium and the 2D slice selected for measurements. The cuberille data and the extracted endometrial boundary also allow for new measurements and shape characterizations based on 3D analysis. The volume of the endometrium is obviously one of these parameters. An in vitro evaluation of such a method has been done by Gilja et al. [12]. Anomalies inside the endometrium can in a similar manner be identified and related to the geometry of the endometrium.

2.4 Volume Rendering

Three-dimensional (3D) display techniques have been studied extensively for other medical applications for the past several years and are well established as a clinical tool in X-CT imaging [15, 36, 39]. Visualization techniques for MRI and PET have also been explored [4, 7, 21, 38, 41]. Recently, special techniques have been proposed for multi-modal images with combination of PET and MR-data [18, 37]. Ultrasonic 3D and 4D have also attracted much interest [24–26, 30–32, 35, 40]. The properties of ultrasonic images are quite different from most of the other medical modalities and

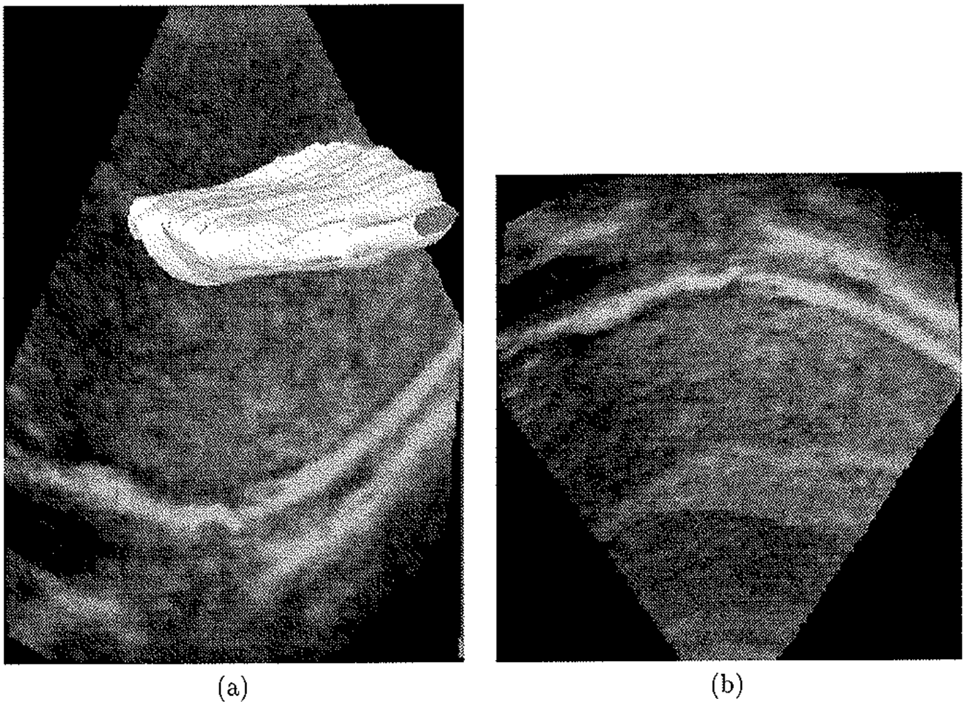
(a) (b)

Figure 5: (a) Visualization of the endometrium together with an arbitrarily positioned 2D slice. (b) The 2D slice associated with Fig. 3(a) which has been correctly positioned for 2D measurements.

most of the general rendering techniques must be adapted before they are useful in ultrasonic imaging.

2.4.1 Surface rendering of the endometrial boundary

There are two basic approaches to visualization of 3D objects: *surface rendering* and *volume rendering.* In surface rendering, an explicit model of the imaged structure is extracted. Typically, a polygonal representation of the boundaries between the various materials or tissue categories is defined and used in the subsequent rendering of the 3D scene. The 3D edge tracing routine generates a 3D object that represents the boundary surface of the endometrium. This object can be used in shape analysis by converting it to an AVS geometric object. The points on the surface are then combined to form a collection of polyhedrons representing the surface. This object can be displayed using, for instance, the Gouraud or Phong shading method. Fig. 4(b) and Fig. 5(a) include surface renderings of the endometrial boundary. Fig. 5(a) combines the surface rendering with 2D slices from the original dataset. This possibility is also useful for validation of the surface definition.

2.4.2 Transparent rendering with direct feature mapping

In order to visualize structures inside or in connection with the endometrium, we have used volume rendering techniques. Generally, it is difficult to render ultrasonic data due to low image quality resulting from acoustic noise and phase anomalies. High density material may absorb the ultrasound waves, leaving structures further from the transducer in the shadow. Several rendering techniques have been studied [31]. The rendering models are based on extracting characteristic parameters from the density evolutions $\rho(t)$ associated with each of the pixels in the view plane where the rendering is accumulated [25]. The success of the rendering technique depends on the particular image signatures that characterize the organ being studied. We have generated transparent renderings of the endometrium with the standard ray-tracing algorithm supported by AVS. The ray-tracing method in AVS is based on an additive light model. In general, transparent views can be constructed by using a scheme introduced by Levoy [19] where each sample location the ray passes through makes a contribution of emitted white light. The contribution is the sampled value ρ multiplied with the corresponding opacity value o. At the same time, incoming light from behind will be filtered by the factor $(1 - o)$. The voxel elements associated with a given location in the view plane are denoted by ρ which consists of the N samples $\rho_1, \rho_2, \ldots, \rho_N$. The following attribute is then extracted:

$$L = \rho_1 o_1 \ + \ \sum_{i=2}^{N} \rho_i o_i \prod_{j=1}^{i-1} (1 - o_j). \qquad (1)$$

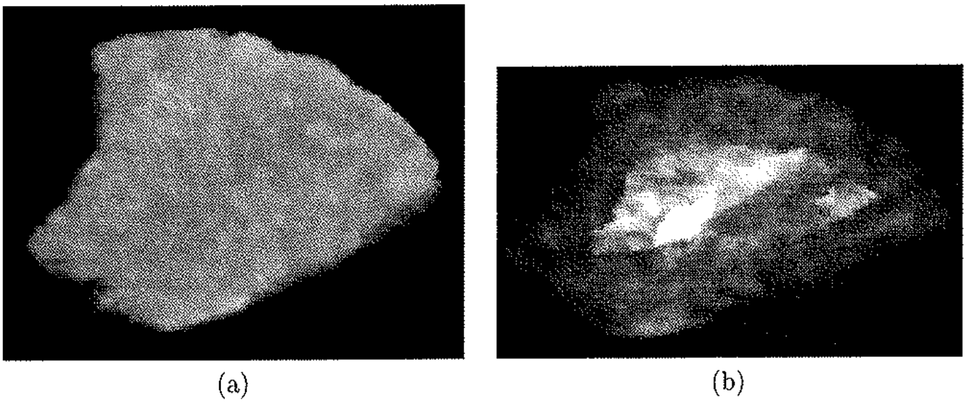
(a) (b)

Figure 6: (a) Volume rendering of the endometrium. It should be noted that no pathological structures are present in the given 3D study. (b) Visualization of the endometrium using opacity assignment based on the distance transform applied to the extracted endometrial boundary.

2.4.3 Computing the distance transform

The AVS geometric object resulting from the edge-tracing method can be used as a region of interest (ROI) in the rendering algorithm. If we in addition calculate the three-dimensional Euclidean vector distance transform [8, 22, 28], we get an extended ROI that can be used in controlling the opacity values. The distance transform (DT) is calculated from a binary volume containing the extracted edge information. The output of the DT algorithm is a vector field where each voxel in the volume contains a vector pointing at its closest point on the extracted edge. This leaves us with a volume where each voxel is associated with its closest point on the endometrium surface. In particular, we can compute the distance to the surface of the endometrium and the inside and outside of the endometrium can be distinguished [34].

We can now use this information in order to change the opacity values in the original dataset. If we want to look inside the endometrium, we can specify that the opacity should be reduced in the area where the length of the DT vectors is less than a certain value. The rendering will now produce a semi-transparent view with the ability to show structures inside the endometrium. In addition, we can specify a certain amount of data to be added to the ROI on the outside of the endometrium in order to visualize structures growing into the uterus.

2.4.4 Fuzzy segmentation of the endometrium

We have previously presented a technique for volume rendering of tumors in 3D ultrasound based on fuzzy segmentation [32]. The user can move a 2D plane arbitrarily in the 3D scene and insert seeds for an automatic segmentation process. The selected seeds are used as the source in a Dijkstra algorithm computing for every voxel the shortest path to one of the selected seeds. The volume is interpreted as a graph with a node for each voxel element and an edge between neighboring voxels. The cost is computed as a function of the difference in image characteristics between each individual voxel and the set of voxels that are used as seeds. Finally, we use the shortest distance computed by the Dijkstra algorithm as a basis for opacity assignments. In this way, fuzzily defined tumors can be visualized in a 3D scene together with a transparent version of the endometrial boundary.

2.4.5 Volume rendering based on Principal Component Analysis (PCA)

The detection of anomalies in the endometrium can mathematically be modeled as a detection of inhomogeneities in the ROI extracted in the edge-tracing. Principal Component Analysis can be used in the rendering pipeline to highlight such inhomogeneities [24]. The meaning of absolute pixel values in the rendered scene are on the other hand usually lost with this technique. Detected anomalies must be inspected and verified with alternative rendering methods or positioning of 2D planes inside the 3D scene.

Figs. 7(a) and (b) contain the results for a reproducible experiment [24]. A synthetic $256 \times 256 \times 128$ cube was generated with intensity values selected randomly from two different normal distributions. Both distributions had a mean value of 128, but the standard deviations were different. A cylinder with a radius of 64 pixels and a length of 42 pixels was inserted in the center of the volume. The main axis of the cylinder was perpendicular to the 256×256 faces of the data cube. The values inside the cylinder had a standard deviation of 16 and the values outside the cylinder had a standard deviation of 32. The volume was viewed such that the cylinder was slightly tilted and extended from the lower left to the upper right. Figs. 7(a) and (b) illustrate how textural variances can be lost in the projection of the 3D data to the 2D view plane. The principal component analysis of the extracted density evolutions recomputes the rendering function such that any inhomogeneity in the rendered scene is highlighted.

3 Results

The work presented in this paper was implemented in C under AVS. The various methods have been integrated in a prototype application that can be used by clinicians in future 3D TVS studies. The prototype provides the clinicians with the following possibilities:

1. The boundary of the endometrium and other objects in the 3D scene can be reliably and efficiently extracted in a semi-automatic edge detection environment.
2. The resulting 3D objects can be visualized in 3D and combined with arbitrarily positioned 2D slices as in Fig. 4(b) and Fig. 5(a). The volumes of the extracted objects are computed.

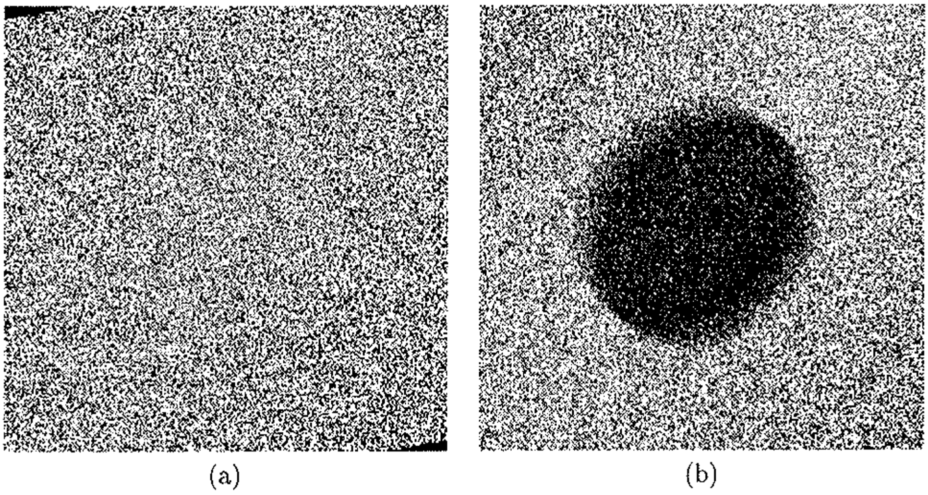
(a) (b)

Figure 7: (a) Volume rendering of synthetic dataset with average value projection. The cylinder inside the cuberille has been lost in the rendering process. (b) Volume rendering of synthetic dataset with principal component analysis of the density distributions extracted in the raytracing process.

3. The 3D scene illustrated in Fig. 5(a) can be interactively modified in order to assure that the 2D slice intercepts the endometrium in a perpendicular manner. Exaggerated thickness estimates due to inclined 2D planes can hence be avoided. As mentioned, measuring endometrium thickness can be of great diagnostic value. Using the AVS geometry object, the user can click with the mouse on the surface where he wants a thickness estimate. This value is calculated as described in the previous section. In this example, the endometrium is from a postmenopausal woman; the thickness of the endometrium is approximately 6 mm, i.e., slightly thicker than the limit at 4 mm reported in a Scandinavian multi-center study [16].

4. Several volume rendering strategies adapted to the current application have been described. In particular, we utilize the extracted endometrial boundary in a distance transform computation in order to allow the user to interactively adjust the opacity assignment based on the distance to the endometrium surface. The user can, for example, make voxels closer than 2 mm to the endometrium surface transparent. Voxels violating the reported 4 mm thickness test would in this case be selected in the volume visualization. An example of this is given in Fig. 6(b). Here we can see an echogenic structure lying inside the endometrium fold. This structure can now be analyzed from several angles. In this example, the structure is an artificial, inhomogenic form containing normal distributed data. Volume rendering techniques that can assist the process of, for example,

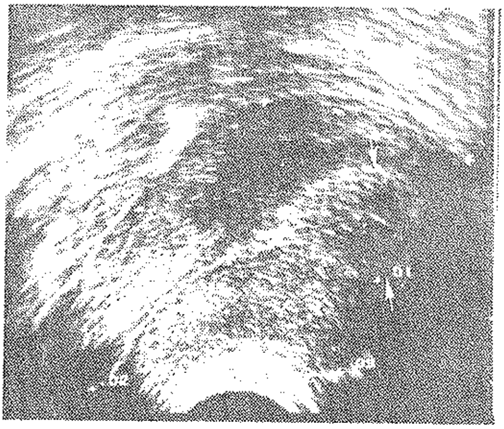

Figure 8: Image of an endometrium containing a polyp (arrow).

tumor characterization have also been described, but real data with the given pathological findings have unfortunately not yet been available for validation of the proposed techniques.

4 Discussion

In this work, we have explored the field of 3D transvaginal ultrasound. TVS is used for various clinical examinations, but we have focused on the endometrium and developed tools for quantitative analysis and volume visualization. A semi-automatic 3D edge detecting environment has been developed. The environment allows the user to reliably and efficiently extract the endometrial boundary surface from the cuberille data. This methodology appears to be important in many different 3D ultrasound applications. We demonstrate how the thickness of the endometrium can be measured using the 3D information to ensure the validity of the thickness estimate. We can also measure the exact volume of the endometrium, something that could not be done using 2D TVS due to the irregular shapes that are often encountered. Further clinical studies will validate the usefulness of this possibility.

For shape analysis, the AVS geometric object gives us a simple tool for 3D visualization. We have also done volume rendering of the original 3D ultrasound data, and we have shown a method of using the 3D Euclidean distance transform in order to produce a semi-transparent visualization where regions relative to the boundary of the endometrium can be interactively selected by the user. In addition, we have described an alternative volume rendering algorithm that can be used both interactively and automatically to characterize for example tumors inside the endometrium. In particular, we can estimate the volume and shape characteristics of such findings inside the endometrium. We have unfortunately not had a 3D study available containing pathological structures that could have been used to validate the proposed techniques. Fig. 8 is a 2D image of an endometrium containing a polyp (arrows). The validation will be done in a clinical follow-up study which will take place in order to further investigate the possibilities of 3D TVS.

5 Acknowledgments

The authors would like to thank Vingmed Sound and the Norwegian Research Council for supporting this study.

References

1. H. I. Abdalla, A. A. Brooks, M. R. Johnson, A. Kirkland, A. Thomas, and J. W. W. Studd. Endometrial thickness: a predictor of implantation in ovum recipients? *Human Reprod*, 9(2):363–365, 1994.
2. A. A. Amini, T. E. Weymouth, and R. C. Jain. Using dynamic programming for solving variational problems in vision. *IEEE Trans on Pattern Analysis and Machine Intelligence*, 12(9):855–867, Sept. 1990.
3. M. Atri, S. Nazarnia, A. Aldis, C. Reinhold, P. Bret, and G. Kintzen. Transvaginal US appearance of endometrial abnormalities. *Radiographics*, 14:483–492, 1994.
4. L. Axel, G. T. Herman, J. K. Udupa, et al. Three-dimensional display of NMR cardiovascular images. *Comput Assist Tomography*, 7:172–174, 1983.
5. H.-G. Blaas, S. Eik-Nes, T. Kiserud, S. Berg, B. Angelsen, and B. Olstad. Three-dimensional imaging of the brain cavities in human embryos. *Ultrasound Med Biol*, 5:228–232, Apr. 1995.
6. K. Boehm and F. U. Niethard. Dreidimensionale ultraschalldarstellung der saeuglingshuefte. *Bildgebung/Imaging*, 61(2):126–129, 1994.
7. M. Bomans, K.-H. Hohne, U. Tiede, and M. Riemer. 3D segmentation of mr images of the head for 3D display. *IEEE Trans on Medical Imaging*, 9(2), June 1990.
8. G. Borgefors. Distance transformations in arbitrary dimensions. *Computer vision, graphics and image processing*, 27:321–345, 1984.
9. A. Delcker and H. C. Diener. 3D ultrasound measurement of atherosclerotic plaque volume in carotid arteries. *Bildgebung/Imaging*, 61(2):116–121, 1994.
10. A. Dørum, G. Kristensen, A. Langebrekke, T. Sørnes, and O. Skaar. Evaluation of endometrial thickness measured by endovaginal ultrasound in women with postmenopausal bleeding. *Acta Obstet Gynecol Scand*, 72:116–119, 1993.

11. A. C. Fleisher, C. M. Herbert, G. A. Sacks, A. C. Wentz, S. S. Entmann, and A. E. James. Sonography of the endometrium during conception and nonconception cycles of in vitro fertilization and embryo transfer. *Fertil Steril*, 46(3):442–447, 1986.

12. O. Gilja, N. Thune, K. Matre, T. Hausken, S. Ødegaard, and A. Berstad. In vitro evaluation of three dimensional ultrasonography in volume estimation of organs. *Ultrasound Med Biol*, 20(2):157–165, 1994.

13. S. Granberg, M. Wikland, B. Karlsson, A. Norstrom, and L. Friberg. Endometrial thickness as measured by endovaginal ultrasonography for identifying endometrial abnormality. *Am J Obstet Gynecol*, 164(1):47–52, 1991.

14. U. M. Hamper, V. Trapanotto, S. Sheth, M. R. DeJong, and C. I. Caskey. Three-dimensional US: Preliminary clinical results. *Radiology*, 191(2):397–401, 1994.

15. D. C. Hemmy, D. J. David, and G. T. Herman. Three-dimensional reconstruction of craniofacial deformity using computed tomography. *Neurosurgery*, 13:534–541, 1983.

16. B. Karlsson, M. Wikland, P. Ylöstalo, et al. Transvaginal ultrasound of the endometrium to identify endometrial abnormality - a nordic multicenter study. To be published, 1995.

17. S. Lenz and S. Lindenberg. Ultrasonic evaluation of endometrial growth in women with normal cycles during spontaneous and stimulated cycles. *Human Reprod*, 5 (4):377–381, 1990.

18. D. N. Levin et al. Integrated three-dimensional display of MR and PET images of the brain. *Radiology*, 172:783–789, 1989.

19. M. Levoy. Volume rendering: Display of surfaces from volume data. *IEEE Computer Graphics and Applications*, pages 29–37, May 1988.

20. T. Li, L. Nuttall, L. Klentzeris, and I. D. Cooke. How well does ultrasonographic measurement of the endometrial thickness predict the results of histological dating? *Human Reprod*, 7(1):1–5, 1992.

21. T. R. Miller, J. B. Starren, and R. A. Grothe. Three dimensional display of positron emission tomography of the heart. *J Nuclear Medicine*, 29(4):530–537, 1988.

22. J. Mullikin. The vector distance transform in two and three dimensions. *CVGIP: Graphical Models and Image Processing*, 54(6):526–535, Nov. 1992.

23. B. Olstad. Automatic wall motion detection in the left ventricle using ultrasonic images. In *Proceedings of SPIE/SPSE Electronic Imaging, Science and Technology*, San Jose, 1991.

24. B. Olstad. Maximizing image variance in rendering of volumetric data sets. *Journal of Electronic Imaging*, 1:245–265, July 1992.

25. B. Olstad, E. Steen, and O. Sandstå. Shell rendering with hardware supported data extraction. In *Proceedings of SPIE Medical Imaging*, San Diego, USA, 1995.

26. B. Olstad and N. Thune. Visualizing 4-D medical ultrasound data. In *Proceedings IEEE Visualization '91*, San Diego, California, Oct. 1991.

27. B. Olstad and H. E. Tysdahl. Improving the computational complexity of active contour algorithms. In *8th Scandinavian Conference on Image Analysis*, 1993.

28. I. Ragnemalm. The euclidean distance transform in arbitrary dimensions. *Pattern recognition letters*, 14:883—888, Nov. 1993.

29. P. Smith, O. Bakos, G. Heimer, and U. Ulmsten. Transvaginal ultrasound for identifying endometrial abnormality. *Acta Obstet Gynecol Scand*, 70:591–594, 1991.

30. E. Steen and B. Olstad. Scale-space and boundary detection in ultrasonic imaging, using signal-adaptive anisotropic diffusion. In *Proceedings SPIE Medical Imaging*, Feb. 1994.

31. E. Steen and B. Olstad. Volume rendering of 3D medical ultrasound data using direct feature mapping. *IEEE Trans on Medical Imaging*, 13(3):517–525, Sept. 1994.

32. E. Steen, B. Olstad, S. Berg, G. Myklebust, and K. P. Schipper. Combined visualization of tumor and vessel geometry. In *Proceedings of IEEE Ultrasonics*, Cannes, 1994.

33. TomTec Systems Inc., USA. *EchoScan User Manual*, 1993.

34. A. Torp and B. Olstad. Multispectral analysis of object surfaces extracted from volumetric data sets. In *Proceedings of IEEE ICIP*, Austin, Texas, 1994.

35. H. Torp, S. Dørum, E. Holm, et al. Real-time three dimensional echocardiography for assessment of valvular function. *Submitted to 11th Symposium on Echocardiology*, 1995.

36. W. G. Totty and M. W. Vannier. Analysis of complex musculoskeletal anatomy using three-dimensional surface reconstruction. *Radiology*, 150:173–177, 1984.

37. D. J. Valentino. Volume rendering of multimodal images: Applications to MRI and PET imaging of the human brain. *IEEE Trans on Medical Imaging*, 10(4): 554–561, 1991.

38. M. W. Vannier, S. Gronemeyer, F. R. Gutierrez, et al. Three-dimensional magnetic resonance imaging of congenital heart disease. *Radiographics*, 8(5):857–871, 1988.

39. M. W. Vannier, J. L. Marsh, and J. O. Warren. Three-dimensional CT reconstruction for craniofacial surgical planning and evaluation. *Radiology*, 150:179–184, 1984.

40. O. T. von Ramm, S. W. Smith, and H. G. Pavy Jr. High-speed ultrasound volumetric imaging system - part i-ii: transducer design and beam steering. *IEEE Trans on Ultrasonics, Ferroelectrics and Frequency control*, 38, Mar. 1991.

41. S. Webb, R. J. Ott, M. A. Flower, et al. Three-dimensional display of data obtained by single photon emission tomography. *Brit J Radiology*, 60:557–562, 1987.

Paper C

Accuracy of in-vitro volume estimation of small structures using three-dimensional ultrasound

Sevald Berg, Hans Torp and Harm-Gerd Blaas[†]

Department of Physiology and Biomedical Engineering,
Norwegian University of Science and Technology, Trondheim, Norway
[†]National Center for Fetal Medicine,
Trondheim University Hospital, Trondheim, Norway

Abstract

We describe an ultrasound probe for three-dimensional transvaginal imaging. The transducer was an annular array with a center frequency of 7.5 MHz which was rotated with an internal stepper motor. The probe had no external moving parts, and the total volume covered by a full rotation defined a half sphere. The raw digital data from the scanner were transferred to an external PC for three-dimensional reconstruction. We evaluated the three-dimensional imaging system by measuring the volumes of phantoms (range 24.8–3362.5 mm^3) in a water tank, and found good correlation with true volumes (two observers measurements gave a linear regression with a slope of 1.010 and $R^2 = 0.993$, and a slope of 0.956 and $R^2 = 0.993$ respectively). The size of the point-spread function was used in the calculations to eliminate the effect of under- or overestimation due to the limited ultrasound beam resolution. An example of data acquisition, volume estimation and imaging of an embryo less than 8 weeks old *in vivo* with the brain cavities and body is given. We conclude that the three-dimensional reconstruction and volume estimation were accurate and reproducible.

Submitted for publication, 1999

1 Introduction

There has been a significant development of medical three-dimensional (3D) ultrasound in the past twenty years, and obstetrics and gynecology has been one of the main areas of application. Brinkley et al. [6] showed that fetal weight estimation was possible using a position locator system for 3D reconstruction. Later, mechanically tilted probes were introduced and successful volume imaging of fetal structures, including malformations, has been performed [10, 13, 16, 18]. Transvaginal 3D imaging based on rotating the ultrasound probe with a stepper motor has been reported [4, 12].

Measurements in 3D ultrasonography may be subject to errors due to the limited resolution of the ultrasound beam, or to errors in the spatial position of the scan planes. The consequence of limited resolution is that small structures and object borders will be smeared out in the image and appear larger than they are. Delineation of these borders may result in overestimation of distances and volumes, or underestimation of the volume of cavities. In addition, patient movement during acquisition or errors in the 3D rotation will result in reconstruction artifacts. Because of these problems, it is important to evaluate 3D ultrasound systems before clinical use.

Volume estimation using 3D ultrasound has been applied *in vivo* on such organs as the kidneys [7] and the heart ventricles [17], showing good correlation with other measurement methods. However, since the reference methods also are subject to measurement errors, *in vitro* validation is necessary to further evaluate the estimation accuracy. One common technique for such validation is to estimate the volumes of balloons in a water tank [9]. The volume estimated by tracing the center line of the balloon border is not much influenced by the limited ultrasound resolution. In the case of *in vivo* measurements, however, it is difficult to identify the exact object border since we have backscattered signals from inside the object as well as from the borders.

The purpose of this study was to describe and evaluate a new transvaginal 3D ultrasound probe. We developed a method for volumetric analysis of small structures that we evaluated *in vivo* using water tank phantoms made of agar gel with kaolin particles. The size of the phantoms covered a large scale. The size of the point-spread function was used to compensate for the overestimation due to the limited ultrasound beam resolution. In this paper, we first describe the data acquisition and the transvaginal 3D probe. The theoretical spatial sampling density requirement is then analyzed followed by a description of the volume measurement method. The results show the accuracy of the phantom volume measurements, and an application of the technique in human embryology is demonstrated.

2 Materials and methods

2.1 Data acquisition

We used a specially developed 3D transvaginal probe, connected to a System Five digital ultrasound scanner (Vingmed Sound, Horten, Norway). Rotation of the transducer was done by an internal stepper motor. The raw digital data were transferred from

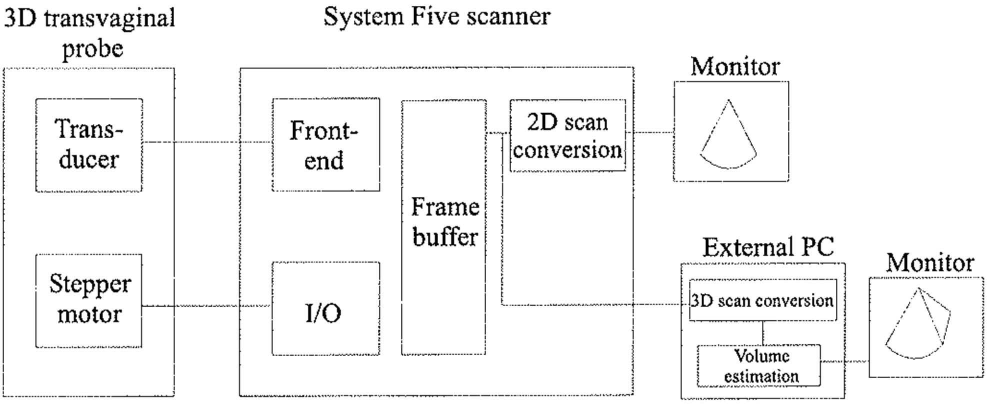

Figure 1: Data flow diagram. The 3D probe was coupled directly to the ultrasound scanner, and the raw digital data from the scanner were transferred to a PC and used in the 3D reconstruction.

the scanner frame buffer to an external PC for 3D reconstruction (Fig. 1). The motor activity was controlled by the scanner. When the motor speed was adapted to the scanner frame rate, one scan took typically 2–5 s depending on the angle of rotation.

2.2 Probe design

The transvaginal 3D probe had a total length of 298 mm and had a 7.5 MHz annular array transducer with an aperture of 11.5 mm (Fig. 2). The transducer mid-position was tilted 45 degrees in the 2D scan plane (azimuth direction), with a maximum azimuth scanning angle of 90 degrees (Fig. 3). The scan plane of the transducer was rotated inside the housing (dome), so that the probe had no external moving parts except for the probe cable connector. The 2D scan plane could be rotated 360 degrees.

2.3 Spatial resolution

The accuracy of measurements in ultrasound images is limited by the ultrasound beam resolution. The resolution can be measured by the size of the image point-spread function which is given by the beam width and the pulse length. For an annular array transducer the focus is symmetrical and the focal diameter D_F at the focal distance F is given by:

$$D_F = \Theta_{X\mathrm{dB}} \cdot F = k_X \cdot \frac{\lambda}{D} \cdot F, \tag{1}$$

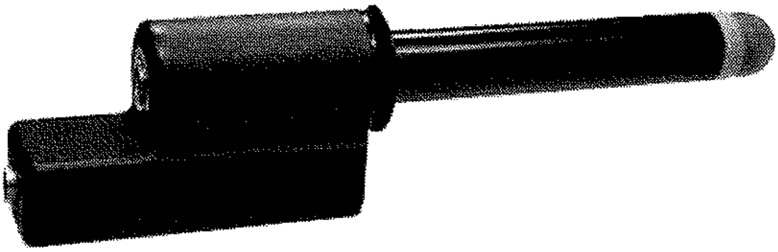

Figure 2: The transvaginal 3D probe. Dome length: 175 mm, total length: 298 mm, dome diameter: 25.6 mm, transducer center frequency: 7.5 MHz. The probe had no external moving parts except for the cable connector.

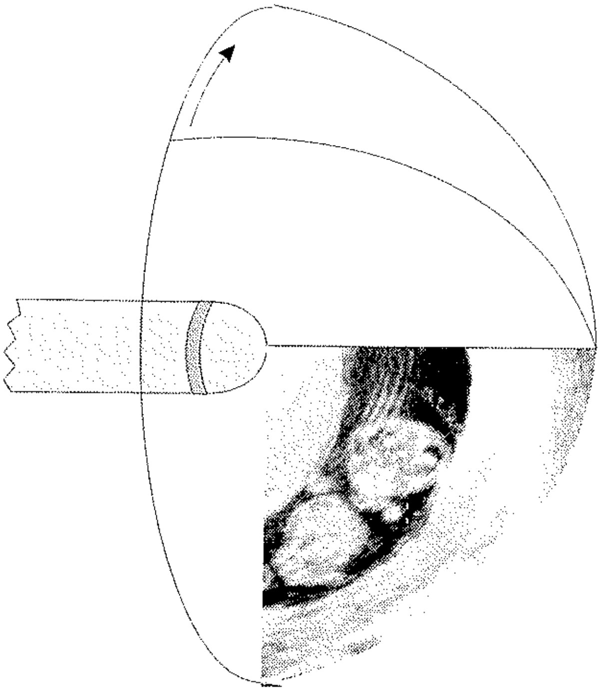

Figure 3: The data volume covered by rotation of the scan plane with an azimuth scanning angle of 90 degrees. The transducer mid-position was tilted 45 degrees. The scan plane could be rotated 360 degrees.

where $\Theta_{X\mathrm{dB}}$ is the opening angle defined by the X dB beam amplitude reduction. We used 12 dB two-way reduction to define the lower amplitude value limit. Furthermore, λ is the ultrasound wavelength, and D is the aperture diameter. The parameter k_X is the amplitude reduction factor, and for 12 dB two-way reduction we get $k_{12\mathrm{dB}} = 1.4$ [1]. The depth of focus, L_F, is defined as the region where the beam diameter is limited by diffraction, and can be expressed as where the on-axis beam amplitude has dropped 1 dB:

$$L_F(1\mathrm{dB}) = 2 \cdot D_F(12\mathrm{dB}) \cdot \frac{F}{D}. \tag{2}$$

The resolution in the radial direction was given by the length of the transmitted pulse T_p:

$$\Delta r_p = c \cdot \frac{T_p}{2} = \frac{\lambda}{2} \cdot f \cdot T_p, \tag{3}$$

where c is the sound velocity and f is the transmit frequency. Here, $c = 1540$ m/s was used as the mean value for tissue. The product $f \cdot T_p$ is the number of periods in the transmitted pulse.

The spatial sampling density must be sufficient in all three dimensions to prevent under-sampling in the reconstructed 3D data. The lateral sampling density was determined by the angle increment in the original scan plane, and in our setup we used 60% overlap. We used the same overlap in the elevation direction, so the corresponding 3D rotation angle increment was $\theta = 0.4 \cdot \Theta_{12dB}$. The radial sampling density was determined by the radial resolution. The rotational speed w (degrees/s) depended on the scanner frame rate, fr (frames/s): $w = fr \cdot \theta$.

2.4 Volume reconstruction

The data were scan converted and interpolated into a regular 3D volume using the EchoPAC-3D software (Vingmed Sound, Horten, Norway), and visualized by extracting 2D slices at different positions [15]. The accuracy of the rotation was evaluated by measuring the actual probe movement, and by imaging a grid phantom placed in a water bath. The probe was kept in a fixed position during rotation, and the grid was placed at a 45 degree angle to the probe rotation axis. Since the probe needed a few milliseconds to accelerate, a few frames were left out from the reconstruction at the start and at the end of the rotation to avoid artifacts.

2.5 Volume measurement

In this study we used manual delineation of the object borders; this was performed by manually tracing contours in different 2D slices of the data. The contours did not have to be parallel, as long as they did not intersect. This resulted in a set of planar contours which were converted into a polyhedron created by a triangulation of consecutive contours. The volume of this polyhedron was calculated, giving an estimate of the object volume. This volume estimation algorithm has been described in detail [19].

The value D_p defined the size of the point-spread function, i.e., the lateral image resolution, and Δr_p defined the radial image resolution. All structures in the ultrasound image were smeared out or blurred with an amount corresponding to these values. An object of true length l had length $l + D_p$ when positioned horizontally, and length $l + \Delta r_p$ when positioned vertically in the image. In the focal zone L_F, $D_p = D_F$.

If the lengths of the object for all directions are known, the measurement error caused by the limited resolution of the ultrasound beam can be corrected by appropriate scaling of the object. If the lengths are almost equal, we can use the volume of a cube to approximate the measured volume, V_m. Here, such a cube was oriented in the radial/lateral dierection. The length of each side was then $l_m = V_m^{\frac{1}{3}}$. The true length l in the lateral direction and r in the radial direction was corrected to be $l = l_m \pm D_p$ and $r = l_m \pm \Delta r_p$. The minus sign was used for overestimated organ volumes, and the plus sign was used for underestimated cavity volumes. The following correction factor, k_{psf}, was introduced to estimate the true measured volume, $\hat{V}_m$:

$$\hat{V}_m = k_{psf} \cdot V_m. \tag{4}$$

Using the scaled dimensions of the cube, the correction factor for the point-spread function was:

$$k_{psf} = l^2 \cdot r / V_m. \tag{5}$$

2.6 Phantom volumes

Ten cylindrical phantoms were made out of agar gel mixed with kaolin (range 24.8–3362.5 mm^3) and placed in a water bath on top of a block of clear agar gel. Each object was scanned three times from different, random angles ($n = 30$), with the 3D rotation angle in the range 27–111 degrees. The water had a temperature of 21°C. At this temperature, the sound velocity was 1485.4 m/s [14]. To compensate for the difference in sound velocity for the water and the scanner setting of 1540 m/s, we scaled each measured volume by a factor $k_{vel} = (1485.4/1540)^3$. The outer boundary of the object was traced by two observers and the corresponding volume was estimated from the following equation:

$$\hat{V}_m = V_m \cdot k_{psf} \cdot k_{vel}. \tag{6}$$

The true volume, V_t, was calculated by measuring the diameter and the height of each object with a vernier caliper. We used the same phantoms as described in an earlier study [3], but in this study the contours were retraced by different observers, thus we obtained new volume estimates.

2.7 Statistical analysis

All volumes were traced once by two observers blinded for each other's results. The estimates were compared with the true volumes by linear regression with the line fit curve passing through zero. The mean percentage error ± standard deviation (SD) was calculated for two ranges of the volumes: larger and smaller than 500 mm^3. The mean percentage error was defined as the mean of the percentage difference between true and estimated volumes. Interobserver variability was expressed as the SD of the difference of the two observers' estimates divided by the true values. The volumes were also analyzed according to Bland and Altman [5]. We compared the percentage difference between the estimated and true measured volumes with the true measured volumes. Similarly, we found the impact of the mathematical corrections by comparing the estimated values without any corrections with the true volumes.

2.8 Measurement of embryonic volumes *in vivo*

Transvaginal 3D data were acquired of an embryo from a healthy pregnant woman with no pregnancy complications. The gestational age based on the last menstrual period was seven and a half weeks. The image was first adjusted for optimal quality and range. Then the probe was manually rotated so that the scan plane was placed to the side of the embryo. Finally, the motor rotated the scan plane to cover just the embryo. The outer border of the embryo body, the embryonic brain cavities, the yolk sac and the amnion sac were all manually outlined. The estimated volumes were then given by: $\hat{V}_m = V_m \cdot k_{psf}$.

3 Results

3.1 Spatial resolution

In Table 1 the ultrasound resolution values for the 3D transvaginal probe are shown. The length of the transmitted pulse, T_p, is a function of the transducer response. We assumed that the propagating pulse had 3 periods. The radial resolution was then $\Delta r_p = 0.32$ mm. In the original scan plane the radial sampling density was less than 1 mm, and the lateral angle increment was less than 0.5°. The rotation step angle increment was: $\theta = 0.4 \cdot \Theta_{12dB} = 0.84°$. This means that the 3D data were recorded with no loss of resolution. With a typical frame rate of 23.7 frames/s, the rotational speed was: $w = 23.7 \cdot 0.84$ degrees/s $= 19.9$ degrees/s.

3.2 Volume reconstruction accuracy

After the raw data were transferred to the computer, the 3D reconstruction was performed within 3 s. Figure 4 shows a slice of the reconstructed grid phantom data. Within the area of the phantom, the reconstruction error was less than the ultrasound beam resolution. This was also confirmed by measuring the amount of rotation on the probe itself.

Transmit frequency (f)	7.5 MHz
Wavelength (λ)	0.21 mm
Aperture diameter (D)	11.5 mm
Focal distance (F)	25 mm
Radial resolution (Δr_p)	0.32 mm
Elevation opening angle ($\Theta_{12\mathrm{dB}}$)	2.1°
Focal diameter (D_F(12dB))	0.64 mm
Focal depth (L_F(1dB))	2.6 mm
Rotation angle increment (θ)	0.84°

Table 1: Ultrasound resolution and sampling density values for the 3D transvaginal probe.

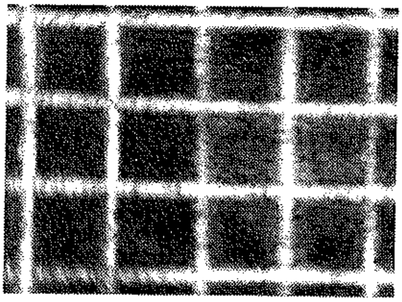

Figure 4: Slice through the 3D reconstruction of a grid phantom. The grid size is 1 cm; the grid is placed 45 degrees to the probe rotation axis.

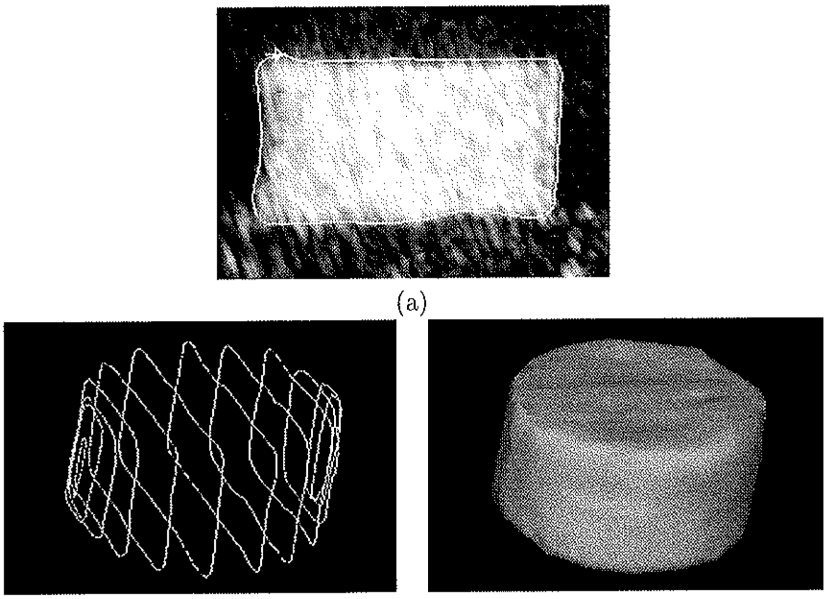

(a)

(b)

(c)

Figure 5: Volume estimation of phantom object with true volume 3094.7 mm^3. (a) The contour of a manually delineated border. (b) All planar contours. (c) Reconstruction of phantom based on contours.

3.3 Volumes of phantoms in a water tank

The delineation of a phantom object is shown in Fig. 5. The resolution correction parameters were set to the values of the point-spread function: $D_p = 0.64$ mm and $\Delta r_p = 0.32$ mm. The correlation between the estimated and the true volumes for the two observers gave linear regression with a slope of 1.010 and $R^2 = 0.993$, and a slope of 0.956 and $R^2 = 0.993$ respectively. In Fig. 6, the percentage difference between the estimated and true measured volumes are plotted against the true measured volumes. The impact of the mathematical corrections can be seen from Fig. 6(a). The mean percentage error of the volume estimates was higher for the volumes <500 mm^3 (12.1% ± 8.6%, and 8.1% ± 8.1%) compared to the volumes >500 mm^3 (0.6% ± 4.3%, and -3.8% ± 4.1%). The interobserver variability for the volumes <500 mm^3 was 6.8% and for the volumes >500 mm^3 it was 3.4%.

3.4 Embryonic brain cavities and body volumes

Figure 7 shows the delineation and 3D reconstruction of an embryo with brain cavities and the yolk sac. The embryo had a crown-rump length (CRL) of 13 mm. The CRL is the greatest length of the embryo from the top of the head to the caudal end of the

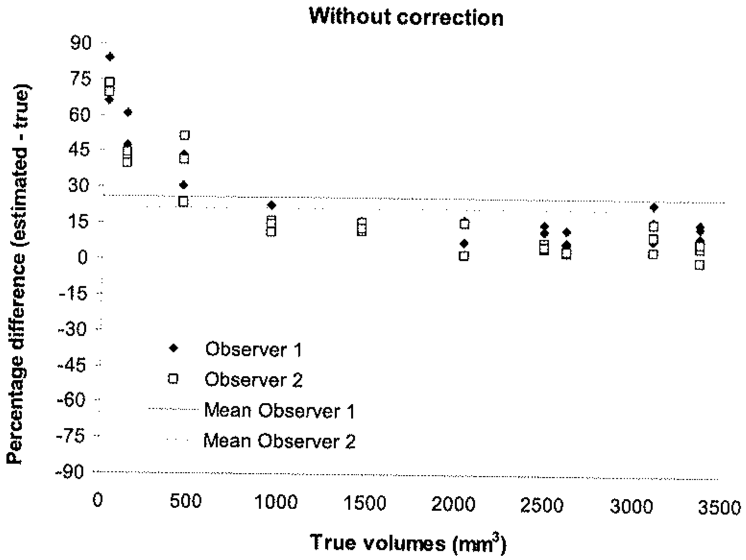

(a)

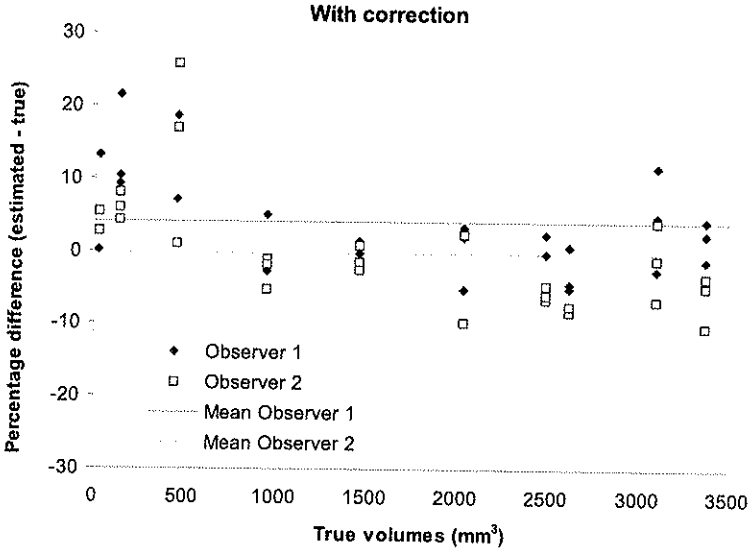

(b)

Figure 6: The percentage difference between the estimated and true volumes compared to the true volumes. (a) The mathematical corrections for the point-spread function has been removed from the estimated volumes. (b) The estimated volumes with the mathematical corrections.

body. The 3D reconstruction is compared with a photograph of an aborted embryo (Fig. 7d).

4 Discussion

In this study we have shown that it was possible to estimate volumes of phantoms >500 mm^3 *in vitro* with excellent accuracy using a transvaginal 3D probe. The estimates were less accurate for the phantoms <500 mm^3 illustrating the problem of measuring very small structures with ultrasound. The percentage error was a function of the volume size since the volume correction was based on the ultrasound beam resolution. The size of the smallest volumes was comparable to the beam resolution giving higher uncertainty, while the impact of the beam resolution was smaller for the larger volumes. The interobserver variability for the volumes >500 mm^3 was small indicating that the volume estimation method was repeatable. The exact placement of the contours was subject to individual variation as is shown by the small bias between the two observers. Such differences are inevitable using manual segmentation of ultrasound images and are in this case regarded as small.

The volume estimation algorithm used in this study has previously been tested on the stomach and kidney *in vitro* [8]. Using a 3D tilting probe, the percentage error ± SD between estimated and true volume was at most mean 9.8% ± 3.1%. The method has also been applied on human kidneys *in vivo*, and compared with 3D magnetic resonance imaging (MRI) [7]. Compared to MRI, the 3D ultrasound method underestimated the volumes (-9.4% ± 8.4%). Other methods for estimating volumes from 3D ultrasound have been reported. King et al. [11] estimated volumes with a mean error of 1.6%, and Basset et al. [2] reported a maximum error of 10%.

The results from the current study indicate that our 3D ultrasound system is adequate for volume estimations. However, we must be aware of the following measurement pitfalls: 1) Volume measurement with ultrasound can give large estimation errors due to the limited resolution of the beams. In this study we have reduced this error by including a measure for the beam resolution in the estimation algorithms. 2) The speed of sound in water tank experiments must be considered with caution. A small deviation of this value compared to the listed value results in a different volume. It is affected by several factors such as the contents of gas (air), salt and temperature. The measured volume must be compensated for the differences in sound velocity in the tank and in the scanner setting. The consequence of different sound velocities inside the phantoms was not regarded as significant in the experiments.

In an *in vivo* study including 34 embryos and fetuses, with CRLs ranging from 9.3–39.0 mm, we measured brain cavities and body volumes and found that the estimates corresponded well with the earlier findings from classic human embryology [3]. In the present study, slightly different resolution correction parameters were used because the contours were traced at the outermost boundary of the object with the gain set at a high value. In a previous study [3] a different observer traced the contours closer to the object. This compensated to a certain extent the blurring of the object borders

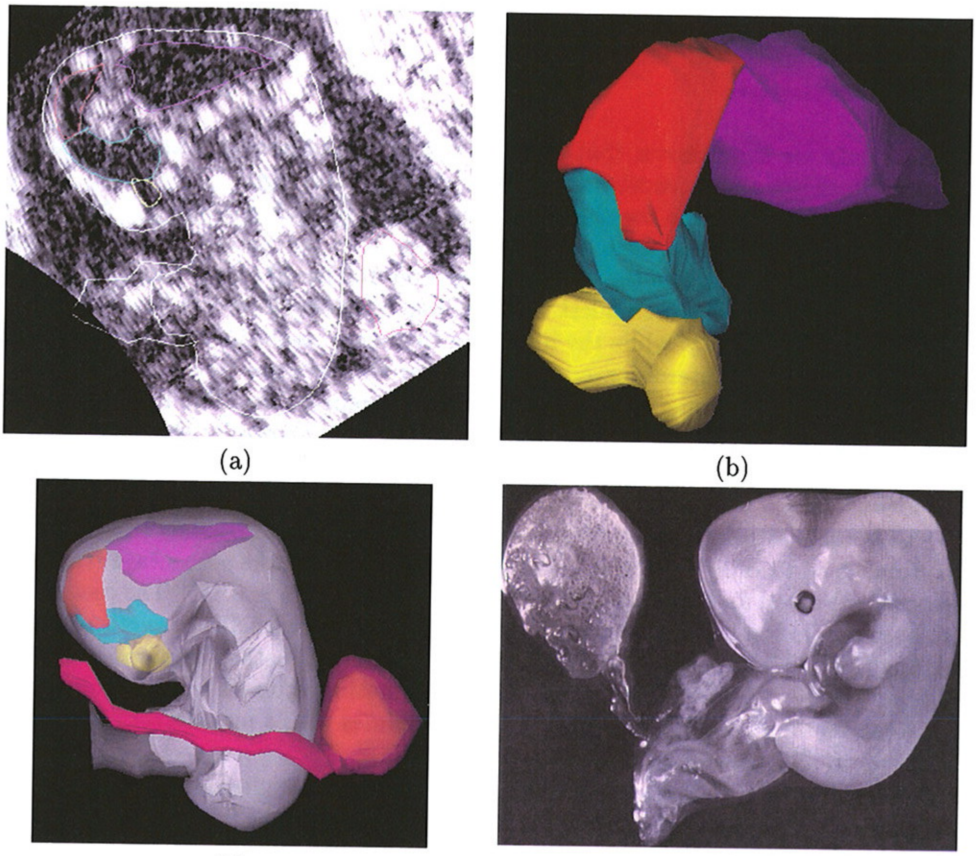

(a) (b)

(c) (d)

Figure 7: (a) The delineation of brain cavities and body of an embryo with CRL 13 mm, age seven and a half weeks based on the last menstrual period. (b) Reconstruction of the brain cavities. Hemispheres (yellow) 5.5 mm^3, diencephalon (green) 6.0 mm^3, mesencephalon (red) 4.0 mm^3, and rhombencephalon (violet) 17.8 mm^3. (c) Reconstruction of the embryo (329.4 mm^3) with part of the umbilical cord; the yolk sac and the vitelline duct lie in front (rose). (d) For comparison: photography of an aborted embryo. The umbilical cord and the vitelline duct leading to the yolk sac on the left side ("The first twelve weeks of gestation", p. 196, E. R. Barnea et. al. (eds.), Springer-Verlag, 1992. Printed with permission from the authors).

caused by the limited beam resolution.

There are several advantages of having the transducer mid-position tilted 45 degrees instead of being aligned with the rotation axis. In the latter case, it is often necessary to do a full 180 degree rotation to cover a sufficiently large volume. Objects that are in the rotation center of a 180 degree rotation are likely to be distorted, since the first and the last 2D images must be at the exact same position; this is difficult to achieve due to movement of the probe and the patient. The tilted mid-position transducer may be rotated a smaller angle to cover the same volume, and the object does not have to be placed in the rotation center. The total volume that is covered in a full 360 degree rotation is $2\sqrt{2}$ times larger than for the probes with the transducer aligned with the rotation axis, when the transducer's scan planes are 90 degrees.

5 Conclusion

With a specially developed 7.5 MHz 3D probe for transvaginal imaging, ultrasound data could be acquired and volume reconstructed with high accuracy. The 3D data were reconstructed with no loss of spatial resolution using the raw digital data from the scanner. Accurate and repeatable *in vitro* volume estimations were achieved for small phantoms (500–3400 mm^3) by including a measure for the ultrasound beam resolution in the volume estimation algorithm. For even smaller phantoms (25–500 mm^3), the estimations were less accurate, but satisfactory considering the small sizes and the limited resolution of the ultrasound beams. Successful reconstruction and visualization of a seven and a half week embryo *in vivo* shows the potential application of studying organ development of embryos and fetuses at an early stage of gestation.

6 Acknowledgments

We thank Ditlef Martens, Christian Michelsen Research, Bergen, Norway, for software support, and Nancy Eik-Nes for revision of the paper.

References

1. B. A. J. Angelsen. *Waves, signals and signal processing in medical ultrasonics. Volume I.* NTNU, Dept. of Physiology and Biomedical Engineering, The Norwegian University of Science and Technology (NTNU), Trondheim, Norway, 1995.

2. O. Basset, G. Gimenez, J. L. Mestas, D. Cathignol, and M. Devonec. Volume measurement by ultrasonic transverse or sagittal cross-sectional scanning. *Ultrasound Med Biol*, 17(3):291–296, 1991.

3. H.-G. Blaas, S. Eik-Nes, S. Berg, and H. Torp. In-vivo three-dimensional ultrasound reconstructions of embryos and early fetuses. *Lancet*, 352(9135):1182–1186, 1998.

4. H.-G. Blaas, S. Eik-Nes, T. Kiserud, S. Berg, B. Angelsen, and B. Olstad. Three-dimensional imaging of the brain cavities in human embryos. *Ultrasound Obstet Gynecol*, 5:228–232, Apr. 1995.
5. J. M. Bland and D. G. Altman. Statistical methods for assessing agreement between two methods of clinical measurement. *Lancet*, pages 307–310, 1986.
6. J. F. Brinkley, W. D. McCallum, S. K. Muramatsu, and D. Y. Liu. Fetal weight estimation from ultrasonic three-dimensional head and trunk reconstructions: Evaluation in vitro. *Am J Obstet Gynecol*, 144(6):715–721, 1982.
7. O. Gilja, A. Smievoll, N. Thune, et al. In vivo comparison of 3D ultrasonography and magnetic resonance imaging in volume estimation of human kidneys. *Ultrasound Med Biol*, 21(1):25–32, 1995.
8. O. Gilja, N. Thune, K. Matre, T. Hausken, S. Ødegaard, and A. Berstad. In vitro evaluation of three dimensional ultrasonography in volume estimation of abdominal organs. *Ultrasound Med Biol*, 20(2):157–165, 1994.
9. S. W. Hughes, T. J. D'Arcy, D. J. Maxwell, et al. Volume estimation from multiplanar 2D ultrasound images using a remote electromagnetic position and orientation sensor. *Ultrasound Med Biol*, 22(5):561–572, 1996.
10. A. D. Hull and D. H. Pretorius. Fetal face: what we can see using two-dimensional and three-dimensional ultrasound imaging. *Semin Roentgenol*, XXXIII(4):369–374, Oct. 1998.
11. D. L. King, D. L. King Jr, and M. Y.-C. Shao. Evaluation of in vitro measurement accuracy of a three-dimensional ultrasound scanner. *J Ultrasound Med*, 10:77–82, 1991.
12. A. Kyei-Mensah, J. Zaidi, R. Pittrof, A. Shaker, S. Campbell, and S.-L. Tan. Transvaginal three-dimensional ultrasound: accuracy of follicular volume measurements. *Fertil Steril*, 65(2):371–376, 1996.
13. A. Lee, A. Kratochwil, J. Deutinger, and G. Bernaschek. Three-dimensional ultrasound in diagnosing phocomelia. *Ultrasound Obstet Gynecol*, 5:238–240, Apr. 1995.
14. J. Lubbers and R. Graaff. A simple and accurate formula for the sound velocity in water. *Ultrasound Med Biol*, 24(7):1065–1068, 1998.
15. D. Martens, T. Hausken, O. H. Gilja, E. N. Steen, H. J. Alker, and S. Ødegaard. 3D processing of ultrasound images using a novel EchoPAC-3D software. *Ultrasound Med Biol*, 23(S1):136, 1997.
16. E. Merz, F. Bahlmann, and G. Weber. Volume scanning in the evaluation of fetal malformations: a new dimension in prenatal diagnosis. *Ultrasound Obstet Gynecol*, 5:222–227, Apr. 1995.

17. Y. F. M. Nosir, P. M. Fioretti, W. B. Vletter, et al. Accurate measurement of left ventricular ejection fraction by three-dimensional echocardiography. *Circulation*, 94(3):460–466, Aug. 1996.

18. E. Steen and B. Olstad. Volume rendering of 3D medical ultrasound data using direct feature mapping. *IEEE Trans on Medical Imaging*, 13(3):517–525, Sept. 1994.

19. N. Thune, O. H. Gilja, T. Hausken, and K. Matre. A practical method for estimating enclosed volumes using 3D ultrasound. *European Journal of Ultrasound*, 3:83–92, 1996.

Paper D

Early reports

In-vivo three-dimensional ultrasound reconstructions of embryos and early fetuses

Harm-Gerd Blaas, Sturla H Eik-Nes, Sevald Berg, Hans Torp

Summary

Background Three-dimensional (3D) imaging of the living human embryo has become possible in the monitoring of embryological development, as described by classic human embryology. We aimed to create 3D images of organs in embryos on early pregnancy.

Methods We used a specially developed 7·5 MHz annular array 3D transvaginal probe to examine embryos. We included 34 women at 7–10 weeks' gestation. We measured the crown-rump length (CRL) of the embryos and fetuses and transferred the 3D ultrasound data to an external computer for further processing to calculate volume.

Findings The CRLs ranged from 9·3 mm to 39·0 mm. The quality of the images of the embryos and fetuses made it possible to outline in detail the outer contours and the contours of the brain cavities, and the calculated volumes corresponded well to the descriptions from classic human embryology.

Interpretation Our 3D imaging system allowed visualisation of structures of less than 10 mm. Therefore, development and abnormal development of fetuses can be monitored.

Lancet 1998; 352: 1182–86

Introduction

Classic human embryology was established by Wilhelm His in 1880–85.[1] His realised the need for magnified three-dimensional (3D) imaging and the need for a model of the dissected object.[1] He made 3D reconstructions from free-hand drawings of histological slices.[2] Born,[3] who in 1876 was the first to describe the technique of making solid reconstructions by stacking wax plates of histological slices, made use of the camera lucida, a device that aided the accurate sketching of small objects. Wax was later substituted by more durable materials such as wood, plaster, glass, or plastic.[1]

Imaging by graphic reconstructions with the aid of special devices has commonly been used in modern human embryology.[4-8] The development of computer technology has opened new possibilities for 3D reconstructions.[9] The first attempt at constructing 3D images of the fetus from ultrasound recordings was made in the early 1980s.[10] The introduction of real-time high-frequency ultrasonography with transvaginal transducers led to improved resolution and allowed detailed imaging of the living embryo.[11,12] The subsequent longitudinal ultrasound studies of the embryological development[13-15] were in agreement with the descriptions from human embryology.[16] Real-time ultrasonography linked with computer technology has made 3D representation of embryonic structures feasible.[17]

We aimed to design a system that used a specially developed transvaginal transducer to enable the study of small embryonic organs in 3D from 7 weeks' to 10 weeks' gestation. We also wanted to describe the development of the living human embryo with emphasis on the shape and the volume of the body and of the brain compartments.

Methods

We developed a 7·5 MHz annular array 3D transvaginal probe to enable the creation of 3D images of very small structures. The probe had an axial resolution of 0·4 mm and a lateral resolution of 0·8 mm. The scan-plane of the transducer was tilted 45° from the end-fire position, rotating inside a fixed dome. The data acquisition (181 frames/volume, range 89–297) took an average of 5·3 s (2·3–8·6). We stored the digital data in the frame buffer of the scanner (System Five, Vingmed Sound, Horten, Norway) and transferred them to an external computer for further processing with Vingmed EchoPAC-3D software (version 1.1). The rotated 2D planes were converted into a 3D dataset. The objects to be studied were segmented by manual drawing of contours in several parallel 2D slices. The parallel 2D slices could be obtained in any plane, so optimum drawing positions for each object could be determined. From these contours, polyhedrons were created to define the surface and the volume of the objects.[18] The objects could be rotated, scaled, and visualised with different colours and different opacity values.

We recruited 35 healthy pregnant women without any previous pregnancy complications from among women who were referred early in their pregnancy for a routine second-trimester

National Center for Fetal Medicine, Department of Obstetrics and Gynaecology, Trondheim University Hospital, N-7006 Trondheim, Norway (H G Blaas MD, S H Eik-Nes MD), **and Department of Physiology and Biomedical Engineering, University of Trondheim** (S Berg MSc, H Torp Dr techn)

Correspondence to: Dr Harm-Gerd Blaas

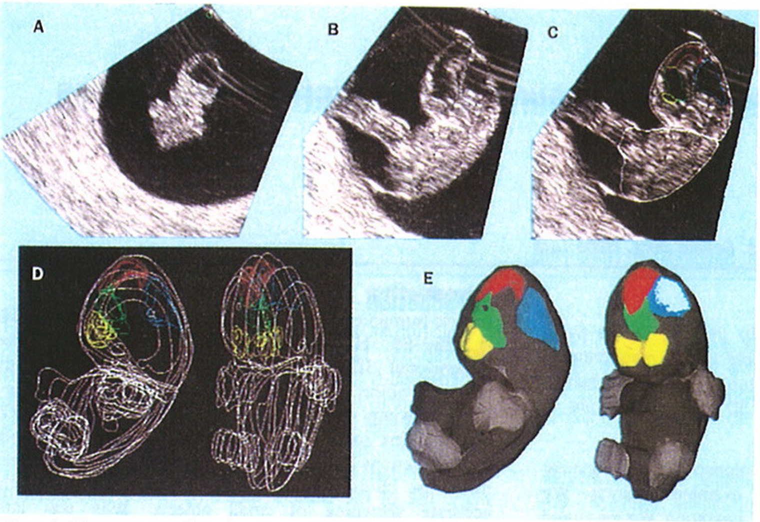

Figure 1: **3D reconstruction of embryo with CRL 17 mm (8 weeks 2 days)**

A=original scan plane through gestational sac and embryo; oblique horizontal section through head with hypoechogenic fourth ventricle, and upper part of thorax. B=rotated 2D sagittal section through embryo in amniotic cavity; umbilical cord leads to left. C=contours drawn manually around head and body (white), lateral ventricles (yellow), third ventricle (green), cavity of mesencephalon (red), and fourth ventricle (blue). D=3D graph of contours. E=3D graph of volumes of body and brain cavities. Opacity of volume reconstruction of body is decreased to show brain cavities.

ultrasonography at our centre. None of the women had used any hormonal treatment during the 3 months before the pregnancy. All were non-smokers. All women gave written informed consent, and the study was approved by the regional committee for medical ethics. We excluded one woman because the baby died of anomalous pulmonary venous return a few days after delivery. The 34 women included in the study gave birth to 17 boys and 17 girls at a mean of 40 weeks 3 days' gestation (range 38–43 weeks), based on the crown-rump length (CRL). The mean birthweight was 3652 g (2770–4970). All but three women delivered spontaneously. Two babies were delivered by caesarean section at 39 weeks 2 days and at 39 weeks 4 days, respectively; the first because of pre-eclampsia, the second because of mechanical disproportion. For one woman with a fetus in breech presentation, delivery was induced with oxytocin at 39 weeks 3 days. All children were healthy.

The gestational age at imaging ranged from 7 weeks to 10 weeks. The CRL measurement is the greatest length of the embryo or fetus from the top of the head to the caudal end of the body. We included the limbs and the physiological midgut herniation in the measurement of the volume of the embryonic or fetal body. We chose the hypoechogenic brain cavities for reconstruction of 3D casts of the brain compartments (figure 1). We included the choroid plexuses in the outlining of the brain cavities. All ultrasound examinations and 3D reconstructions were done by the same person. All statements of gestational age are made in completed weeks and days, based on the date of the last menstrual period. The sonographic appearance of the surface of an object in a fluid is defined by the point-spread function that depends on the resolution of the ultrasound beam. The surface of an embryo will appear, therefore, not as a sharp silhouette, but as a blurred line. Especially small structures will appear larger than they are on the scan, and the outlining will result in overestimation of volume proportional to the surface of the object being scanned, whereas cavities with inner surfaces may be underestimated. We corrected for the point-spread function by modelling the surface with the formula for a cube.

We tested the validity of the volume measurements with ten cylindrical objects of known volumes ranging from 24·8 mm^3 to 3362·5 mm^3 (table 1). The cylinders had different radii and heights, and were made from a mixture of agar gel and kaolin. Each object was measured three times from different positions in a water bath at 21°C; adjustments were made to allow for ultrasound velocity in water bath at 21°C. The deviation distance for the point spread function was calculated to be 0·2 mm, and all volume estimations were corrected by this factor. The correlation between the volume estimates and the true volumes gave a linear regression with a slope of 0·994 (SE 0·0087), and R^2=0·998. The percentage error of the volume estimations was mean 15·6% (9·1) for the three smallest test volumes (<500 mm^3), and mean −0·2% (5·0) for the seven largest test volumes (≥500 mm^3).

We used cross-sectional regression analysis to assess the relation between the estimated volumes and CRL. Simple models to fit the data were searched for, but transformation

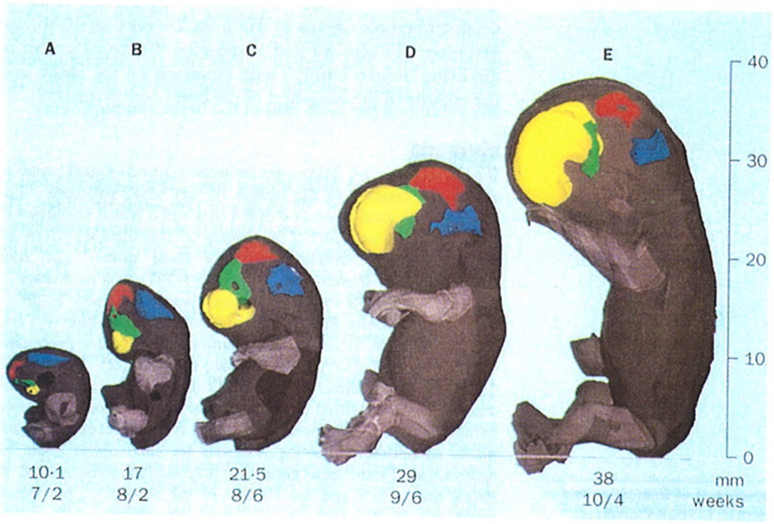

Figure 2: **3D graph of five embryos and fetuses showing development of shape and size from 7 to 10 weeks of gestation**

Cavities of hemispheres (lateral ventricles)=yellow, cavity of diencephalon (third ventricle)=green, cavity of mesencephalon=red, cavity of rhombencephalon (fourth ventricle)=blue.

Measured volumes (mm^3)	Estimated volumes (mm^3)		
	A	B	C
24·8	27·8	30·6	28·1
132·3	175·8	159·6	149·8
449·3	509·6	492·8	454·6
950·8	892·6	1039·6	1007·6
1458·0	1406·2	1385·9	1448·4
2029·0	2112·7	2201·5	1989·7
2483·1	2480·4	2440·6	2383·0
2607·5	2531·2	2514·4	2528·2
3094·7	2991·6	3341·9	3252·5
3362·5	3166·9	3418·7	3173·0

Table 1: **Comparison of measured volumes with 3D volume estimates of test objects**

of the responses were necessary in all six analyses to remove the heteroscedasticity. The normality of the residuals was confirmed by visual inspection and by the Shapiro Francia W test. The assumption of independency and constant variance of the residuals was confirmed by the residual plots.

Results

The CRL of the 34 embryos or fetuses ranged from 9·3 mm to 39 mm. It was possible to describe the development of the embryo based on the assessment of the 3D reconstructions from the 34 individuals. The shape of the embryonic bodies altered substantially from the smallest to the largest embryos and fetuses (figure 2). Initially, the embryonic body was slender in the coronal plane. In embryos with 16–24 mm CRL (figure 2), the body gradually grew thicker, becoming cuboidal and finally ellipsoid shaped with a large head in embryos of 25 mm or more CRL. The limbs were short paddle-shaped outgrowths in the smallest embryos. In an embryo of CRL 14·8 mm, the hands were distinct; the elbows became obvious in an embryo of CRL 20·6 mm (figure 2). The hand angled from the sagittal plane in embryos of 20·5 mm CRL and larger. The soles of the feet touched in the midline in 25 mm embryos. In the largest fetuses, the soles of the feet rotated from the sagittal plane. In the smallest embryos (CRL 9·3–17·0 mm), the rhombencephalic cavity was broad and shallow and lay on top, representing the largest brain cavity (figure 2). The cavity deepened gradually with the growth of the embryos, simultaneously decreasing in length. The position in the head changed as embryos grew, moving posteriorly (CRL 17 mm and larger, figure 2). The rhombencephalic cavity (future fourth ventricle) had a pyramid-like shape with the central deepening of the pontine flexure as the peak of the pyramid. In the fetuses of 25 mm CRL and more, there was a clear gap between the rhombencephalic and the mesencephalic cavity due to the growing cerebellum (figure 2). The isthmus rhombencephali was thin; in most cases it was not visible in its complete length.

In the small embryos, the curved tube-like mesencephalic cavity (future Sylvian aqueduct) lay anteriorly, its rostal part pointing caudally. The cavity of the diencephalon (future third ventricle) ran posteriorly. As the size of the embryos increased, the mesencephalic cavity changed its position posteriorly. The transition from the third ventricle to the mesencephalic cavity and to the lateral ventricles was wide in the early embryos. The cavity of the mesencephalon was large in relation to total volume in all embryos or fetuses. The largest volume of the future third ventricle (11·7 mm^3) was found in an embryo with 20·5 mm CRL (figure 3), but was smaller in the larger embryos and fetuses (CRL≥25 mm) with a narrow upper anterior part.

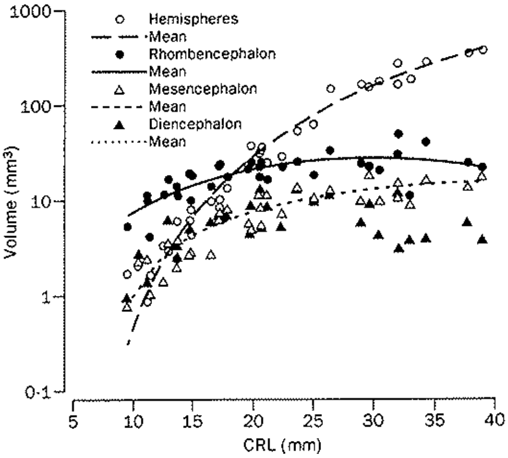

Figure 3: **Measurements and mean volume of lateral ventricles, cavities of diencephalon, mesencephalon, and rhombencephalon**

In the smallest embryos, the medial telencephalon formed a continuous cavity between the lateral ventricles. The future foramina of Monro became distinct in embryos of 19·5 mm CRL. The lateral ventricles gradually changed shape from small round vesicles (CRL 9·3–13·6 mm) via thick round slices originating anterocaudally from the third ventricle (CRL 14·6–17·7 mm) into the crescent shape of the larger embryos (CRL≥20·4 mm, figure 2). In the early fetuses, the thick crescent lateral ventricles filled the anterior part of the head and concealed the diencephalic cavity (figure 2), which became smaller.

The range of the estimated volumes was: bodies 122·0–4987·6 mm^3; all cavities of the brain 6·6–354·1 mm^3; cavities of the hemispheres 0·8–323·8 mm^3; cavities of the diencephalon 0·9–11·7 mm^3; cavities of the mesencephalon 0·7–15·9 mm^3, and cavities of the rhombencephalon 3·8–42·4 mm^3. The estimates of the regression coefficients are shown in table 2.

We combined the measurement of the CRL with the external form of the embryos and the casts of the brain cavities;[8,16] this approach gave an estimate of the development stages (table 3). The correlation of the volumes of the embryo/fetuses and their brain cavities to the CRL are presented in figures 3 and 4.

Response	Intercept	CRL	CRL^2	Residual SE	R^2
Body*	-10·7 (1·1)	2·05 (0·048)	··	2·33	0·983
Cavities of brain*	-3·25 (0·47)	0·554 (0·020)	··	0·986	0·958
Cavity of hemispheres†	-1·34 (0·14)	0·215 (0·0061)	··	0·293	0·975
Cavity of diencephalon*	-1·22 (0·59)	0·316 (0·056)	-0·0063 (0·0012)	0·446	0·526
Cavity of mesencephalon*	-1·17 (0·51)	0·257 (0·048)	-0·0035 (0·0010)	0·385	0·826
Cavity of rhombencephalon*	··	0·325 (0·017)	-0·0054 (0·0006)	0·641	0·978

*Square root transformed, cubic root transformed. †Residual and multiple R^2 are shown.

Table 2: **Estimates (SE) of regression coefficients by linear regression analysis**

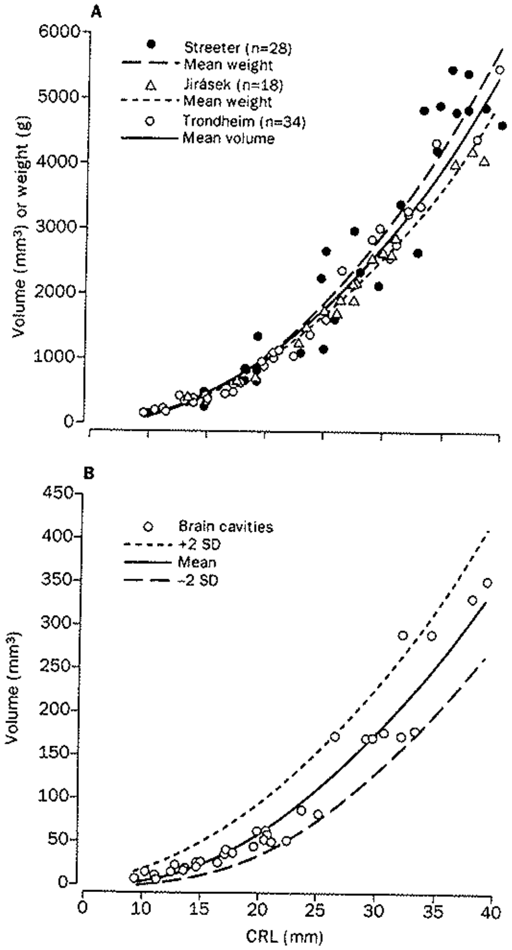

Figure 4: **Volumes of embryos and fetuses and brain cavities**
A=mean volume of embryos and fetuses compared with mean weights from Streeter[23] and Jirásek[24] in embryos CLR ≤40 mm.
B=measurements of total volume of brain cavities, regression line, and ±2 SD.

Discussion

3D reconstructions and measurements of embryos and their brain cavities showed similar results to those from classic embryology, and estimations of the stage of embryos could be made. We confirmed the classic descriptions of the external appearance of the embryonic body and limbs, and of the shape, size, and position of the brain compartments.[6,8]

In previous studies, volume reconstruction of large structures was tested in vitro and in vivo.[18-21] The objects we measured were small, some of them near the limits of the ultrasonographic resolution. Therefore, even small errors in the surface-setting would lead to incorrect volumes. Our test study showed that 3D reconstructions were acceptable, with only a small correction to account for the point-spread function. We believe that the relatively high percentage error in the volume estimation of the small test object of less than 500 mm³ was due to the surface setting in the segmentation procedure, and we may assume that the volumes of embryos up to 17 mm CRL (<500 mm³) became overestimated, whereas volumes of all brain cavities may have been underestimated. We assume that the volume estimations of the embryos of 17 mm CRL and more (≥500 mm³) are good, since the percentage error in the test study only was mean –0·2%, with an acceptable SE of 5·0.

Because of the difference between the embryonic tissue and the amniotic fluid and between the brain tissue and the fluid-filled brain cavities we could analyse the embryonic structures very early, despite their small size. Limitations were set mainly by the resolution of the ultrasonographic equipment. The short duration of the recordings (2·3–8·6 s) was enough to obtain pictures of the fetuses in a quiet phase. Movements of the pregnant woman, such as breathing or pulsation of the abdominal aorta, did not affect the quality of the images.

The difference between the fetal weight (g) and the volume (mm³) is less than 2%.[22] We compared the volumes of the body with measurements of embryos and fetuses that had a corresponding size (CRL ≤40 mm) from two other studies.[23,24] The regression curves were best fitted by a square-root transformation in all three studies (figure 4). The comparison of these different studies involved several possible biases. Streeter[23] studied fresh and formalin-fixed samples; the latter were substantially heavier and longer.[23] In addition, the largest fetuses in Streeter's group were reported to be flexed, and the CRL might have been larger. Drumm and O'Rahilly[25] analysed the relation between measurements of the CRL in vivo by ultrasonography and measurement of the embryo or fetus after abortion. They found that the lengths of embryos in embryological studies was about 1–5 mm less than equivalent in-vivo CRL measurements.[25] Therefore, the condition of the embryos and fetuses in the different studies was not uniform, which may have affected the shape of the curves.

If the mesencephalic cavity had a cylindrical shape, the volume could be calculated by the formula $\pi r^2 \times$length. The embryos in O'Rahilly and Müller's study[6] (Carnegie stage 23 is about 10 weeks 0 days gestational age and CRL 30 mm) would then have a mean volume of 15 mm³ based in the measurements indicated from graphic reconstructions, or 23 mm³ based on the values corrected for shrinkage, whereas the mean volume of the mesencephalic cavity at 10 weeks 0 days in a 2D ultrasound study was only 7·4 mm³.[15] In our study the mean volume in embryos and fetuses of 30 mm CRL was calculated to be 11 mm³ (figure 3). As the rhombencephalic cavity moved posteriorly, it shortened in the sagittal section. In 1890, His showed the changes of the pontine flexure with a decreasing angle in older fetuses.[26] The growth of the cerebellar hemispheres further restricted the volume of the fourth ventricle. In this way, the rhombencephalic cavity did not increase in volume despite the rapid growth of the brain (figure 3). In a previous study, the volumes of the lateral ventricles were estimated

Carnegie stage	Number of embryos and fetuses	CRL range (mm)
16	6	9·3–12·8
17	5	13·5–14·8
18	4	16·4–17·7
19	2	19·5–19·7
20	4	20·4–21·0
21	2	22·3–23·6
22	2	25·0–26·4
≥23	9	≥29·0

Table 3: **Distribution of embryos and fetuses according to Carnegie staging system**

by the formula of two ellipsoids and the rhombencephalic cavity by the formula of a pyramid.[14] Our sonographic 3D reconstructions of the lateral ventricles were in the range of the estimated values from the 2D study; our 3D reconstructions of the rhombencephalic cavity were larger than the range of the estimated values from the 2D study, in which the measurements of the width involved only the main part of the fourth ventricle, not the lateral recesses. The size of the diencephalic cavity has not been measured before. Through the growth of the dorsal and ventral thalami, the lateral walls of this cavity narrow, giving it a slit-like shape. This change in shape explains the decreasing volume of the cavity in the older embryos and fetuses in our study, in which only part of the third ventricle between the dorsal thalamus and the mesencephalon, which is the region near the pineal gland, was discernible. According to embryologists, the recesses of the pineal region and near the infundibulum are distinct in older fetuses.[27]

In 1921, Jenkins[28] carried out a volumetric study of the developing brain. Only two of the embryos he studied were smaller than 40 mm (CRL 16 mm and 25 mm), and the volumes of the brains were calculated to be 41 mm^3 and 126 mm^3. In our study, the mean volume of the brain cavities (figure 4) was 37 mm^3 at 16 mm CRL, and 112 mm^3 at 25 mm CRL; these measurements must be taken to be in agreement with Jenkins' measurements. Jenkins also looked at the proportional growth of the brain compartments, finding a larger share of the diencephalon and the mesencephalon than our measurements showed. At the same time he found less of a shift of the share of the telencephalon and the rhombencephalon between the 16 mm and the 25 mm embryo than we showed (figure 4).

Classic human embryology is based on aborted human embryos and fetuses, as previously summarised.[16] In the Carnegie staging system, embryos are classified by external form and development of the organ system analysed by light microscopy. Such exact staging by ultrasonongraphy is not possible, but we could estimate the stages in the embryos by comparing the external form of the body, the limbs, and the casts of the brain cavities with embryological descriptions.

We showed that it was possible to develop a dedicated transducer system and additional software for 3D imaging of objects of less than 10 mm. The quality of the images allowed description of the outer contours and the development of organ systems, as well as the staging of the embryos between 7 weeks' and 10 weeks' gestation. Our system will also make possible study of abnormal development of the embryo or early fetus and elucidate its progression. The 3D imaging system will help in the avoidance of artefacts and other difficulties in in-vitro assessment of the aborted embryos and may revitalise human embryology.

Contributors

Harm-Gerd Blaas planned the study, did the ultrasound examinations and the 3D-reconstructions, and wrote the paper. Sturla H Eik-Nes supervised the planning and revision of the study and its results. Sevald Berg assisted with the technical performance of the 3D reconstructions of the test series and of the study objects. Hans Torp assisted with the mathematical assessment of the 3D analysis and the validity of the method.

Acknowledgments

We thank Nancy Lea Eik-Nes for revision of the paper.

References

1 His W. Anatomie menschlicher Embryonen. Leipzig: Vogel: 1880–85.
2 His W. Über Methoden plastischer Rekonstruktion und über deren Bedeutung für Anatomie und Entwicklungsgeschichte. *Anat Anz* 1887; **2:** 382–94.
3 Born G. Die Plattenmodellirmethode. *Arch Mikr Anat* 1883; **22:** 584–99,
4 Gaunt PN, Gaunt WA. Solid reconstruction. In: Gaunt PN, Gaunt WA, eds. Three dimensional reconstruction in biology. Kent: Pitman Medical, 1978: 63–73.
5 Müller F, O'Rahilly R. The human brain at stages 21–23, with particular reference to the cerebral cortical plate and the development of the cerebellum. *Anat Embryol* 1990; **182:** 375–400.
6 O'Rahilly R, Müller F. Ventricular system and choroid plexuses of the human brain during the embryonic period proper. *Am J Anat* 1990; **189:** 285–302.
7 O'Rahilly R, Müller F. General embryology and teratology: introduction and general concepts. In: O'Rahilly R, Müller F, eds. Human embryology and teratology. New York: Wiley-Liss, 1992.
8 O'Rahilly R, Müller F. The embryonic human brain: an atlas of developmental stages. New York: Wiley-Liss, 1994.
9 el-Gammal S. ANAT3D: a computer program for stereo pictures of three dimensional reconstructions from histological serial slices. In: Elsner N, Creutzfeld O, eds. New frontiers in brain research. Stuttgart, New York: Thieme, 1987: 46.
10 Brinkley JF, McCallum WD, Muramatsu SK, Liu DY. Fetal weight estimation from ultrasonic three-dimensional head and trunk reconstructions: evaluation in vitro. *Am J Obstet Gynecol* 1982; **144:** 715–21.
11 Timor-Tritsch IE, Farine D, Rosen MG. A close look at the embryonic development with the high frequency transvaginal transducer. *Am J Obstet Gynecol* 1988; **159:** 678–81.
12 Timor-Tritsch IE, Peisner DB, Raju S. Sonoembryology: and organ-oriented approach using a high-frequency vaginal probe. *J Clin Ultrasound* 1990; **18:** 286–98.
13 Blaas HG, Eik-Nes SH, Kiserud T, Hellevik LR. Early development of the forebrain and midbrain: a longitudinal ultrasound study from 7 to 12 weeks of gestation. *Ultrasound Obstet Gynecol* 1994; **4:** 183–92.
14 Blaas HG, Eik-Nes SH, Kiserud T, Hellevik LR. Early development of the hindbrain: a longitudinal ultrasound study from 7 to 12 weeks of gestation. *Ultrasound Obstet Gynecol* 1995; **5:** 151–60.
15 Blaas HG, Eik-Nes SH, Kiserud T, Hellevik LR. Early development of the abdominal wall, stomach and heart from 7 to 12 weeks of gestation: a longitudinal ultrasound study. *Ultrasound Obstet Gynecol* 1995; **6:** 240–49.
16 O'Rahilly R, Müller F. Developmental stages in human embryos. Washington: Carnegie Institution Publishing, 1987.
17 Blaas HG, Eik-Nes SH, Kiserud T, Berg S, Angelsen B, Olstad B. Three-dimensional imaging of the brain cavities in human embryos. *Ultrasound Obstet Gynecol* 1995; **5:** 228–32.
18 Thune N, Gilja OH, Hausken T, Matre K. A practical method for estimating enclosed volumes using 3D ultrasound. *Eur J Ultrasound* 1996; **3:** 83–92.
19 Gilja OH, Thune N, Matre K, Hausken T, Ødegaard S, Berstad A. In vitro evaluation of three dimensional ultrasonography in volume estimation of organs. *Ultrasound Med Biol* 1994; **20:** 157–65.
20 Gilja OH. In vivo comparison of 3D ultrasonography and magnetic resonance imaging in volume estimation of human kidneys. *Ultrasound Med Biol* 1995; **21:** 25–32.
21 Riccabona M, Nelson TR, Pretorius DH. Dreidimensionale Sonographie: zur Genauigkeit sonographischer Volumsbestimmungen. *Ultraschall Klin Prax* 1995; **10:** 35–39.
22 Meban C. The surface area and volume of the human fetus. *J Anat* 1983; **137:** 217–78.
23 Streeter GL. Weight, sitting height, head size, foot length, and menstrual age of the human embryo. *Contr Embryol Carneg Instn* 1920; **11:** 143–70.
24 Jirásek JE, Uher J, Uhrová M. Water and nitrogen content of the body of young human embryos. *Am J Obstet Gynecol* 1966; **96:** 868–71.
25 Drumm JE, O'Rahilly R. The assessment of prenatal age from the crown-rump length determined ultrasonically. *Am J Anat* 1977; **148:** 555–60.
26 His W. Die Entwickelung des menschlichen Rautenhirns vom Ende des ersten bis zum Beginn des dritten Monats. *Abhandl KS Gesellsch Wissensch* 1890; **29:** 3–74.
27 Kostovic I. Zentralnervensystem. In: Hinrichsen KV, ed. Humanembryologie. Berlin: Springer-Verlag, 1990: 381–448.
28 Jenkins GB. Relative weight and volume of the component parts of the brain of the human embryo at different stages of development. *Contr Embryol Carneg Instn* 1921; **13:** 41–60.

Paper E

Quantitative wall motion coding in three-dimensional echocardiography

Sevald Berg[1,2], Anders H. Torp[1], Klaus P. Schipper[3] and Bjørn Olstad[1]

[1]Dept. of Computer Systems and Telematics,
The Norwegian Institute of Technology, Trondheim, Norway
[2]The National Center for Fetal Medicine,
Trondheim University Hospital, Trondheim, Norway
[3]Division of Cardiology,
Trondheim University Hospital, Trondheim, Norway

Abstract

In two-dimensional echocardiography, wall motion analysis is important in detection of heart dysfunction. The methods used suffer from being only approximations due to the complex movement of the heart. The purpose of our study is to use three-dimensional ultrasound in order to improve the quantitative analysis of the left ventricular wall motion. The wall motion is calculated using the three-dimensional Euclidean distance transform, resulting in a set of vectors normal to the endocardial surface. The endocardial wall velocity values are color coded and the surface is rendered creating a cineloop of the left ventricle with color intensities indicating the wall motion. The three-dimensional motion coding technique allows for a precise quantitative analysis of the heart function. Infarcted areas are shown to be marked out with different color intensities due to the muscle activity reduction in that region. The three-dimensional reconstruction improves the diagnosis by visualizing and localizing the whole dysfunctional region in relation to the rest of the ventricular structure.

In *Proc. of SPIE Medical Imaging*, 2709:424–432, 1996

1 Introduction

Much interest has been attracted to the use of three-dimensional (3D) medical ultrasound, and new techniques are evolving addressing the problems of acquisition and visualization. Until now, the main focus has been to visualize structures using different volume rendering techniques [11, 33]. We have seen applications in gynecology and obstetrics [8, 20, 22, 26, 29], for abdominal organs [19], intra-vascular ultrasound [13], brain surgery and cardiology [17, 18, 25, 27, 30, 31]. In most fields, the new modality has yet to be fully accepted as an everyday clinical tool. This due to the cumbersome acquisition, the time and cost of post-processing and the lack of real-time visualization. 3D echocardiography has perhaps been the most successful application where we have commercial systems available. It is possible to do 3D data acquisition for a whole heart cycle generating a 4D dataset. Heart valve reconstruction has been performed for heart surgery in order to improve the pre-operative knowledge.

In two-dimensional ultrasound, quantitative analysis is an important tool, and is achieved by using various imaging techniques for area calculations, ejection fraction estimation [3], Doppler imaging [2, 34] for blood flow velocity and wall motion analysis [4, 16, 32]. However, in 3D medical imaging, quantitative analysis is dominated by research in other modalities such as MRI [5, 35, 37]. These methods range from physical-based modeling of the heart to geometrical techniques. The 3D ultrasonic imaging is a fast evolving field, and quantitative techniques are emerging with volume calculation applications [15, 19, 24] and wall motion estimation [23].

Precise localization of dysfunctional heart regions is a goal in quantitative analysis. In 2D echocardiography much work has been done related to this problem. Manually traced end-diastolic and end-systolic contours are used to calculate the endocardial wall movement using different coding schemes such as the centerline method. With the advances in ultrasound technology, automatic techniques for contour extraction and color motion coding are presented [6, 7, 14]. However, in 2D imaging we are not able to capture the whole heart movement and we may fail to measure the exact ventricle contraction due to the complexity of this movement, as illustrated in Fig. 1. In addition, the size and placement of such regions are difficult to measure with conventional methods. We present a new method for calculating and visualizing heart wall movement in three dimensions. These techniques provide information on regional wall form, size, motion and phase characteristics.

We present a result with a normally functioning human heart. We have also tested the algorithms on phantom 3D data where we know exactly the shape and movement.

2 Methods

2.1 Data acquisition

For our clinical results, the acquisitions were done using a Vingmed CFM-800 ultrasound scanner coupled to the commercially available PC-based TomTec Echo-Scan

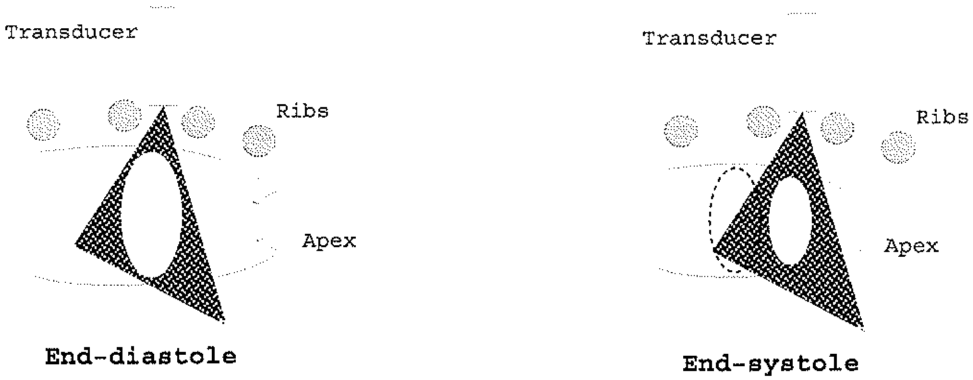

Figure 1: The figure illustrates why 2D acquisition can be insufficient in quantitative analysis. In this transthoracic acquisition, the slice plane is not at the same physical location during the heart cycle because of the global translation of the heart during contraction.

system, with a Vingmed multi-plane transesophageal probe. During acquisition, the system uses ECG-gating to collect 4D data. The transducer is coupled to a stepper motor and is rotated 180 degrees while collecting 2D slices at the same place in the heart cycle. These images are then reconstructed resulting in a four-dimensional dataset consisting of temporally sampled three-dimensional volumes (cuberilles) representing one heart cycle. The data was processed and visualized using AVS from Advanced Visual Systems.

2.2 Edge detection with active contours

Active contours are defined as energy-minimizing splines under the influence of internal and external forces [1, 21]. The internal forces of the active contour serve as smoothness constraints and the external forces guide the active contour towards image features such as high intensity gradients. The optimal contour position is computed such that the total energy is minimized. The contour can hence be viewed as a reasonable balance between geometrical smoothness properties and local correspondence with the intensity function of the image. The optimization process is done by a dynamic programming algorithm. This is an attractive approach in terms of computational complexity and assures global optimality with respect to the energy function.

The total energy of a contour is a sum of local internal and external energy contributions along the contour. The external energy is computed from the image pixel values, and the internal energy represents the shape of the contour.

The 2D active contour energy minimization algorithm can be implemented with the total complexity of $O(nm)$, where n is the number of vertices along the contour and m is the number of candidate points at each vertex [7]. The 2D algorithm is run on the 2D slices of each 3D volume in the dataset. To make the contours smooth from slice to slice, one can use the contour from the previous slice.

2.3 The three-dimensional distance transform

Given a binary dataset of any dimension, where 1 is within a feature, 0 elsewhere. Then, the distance transform [9, 12, 28] is the process of turning this dataset into an equally sized map where each point corresponds to a point in the dataset, and gives the shortest distance from this point to a feature. The distance transform can be utilized in image processing algorithms such as curve smoothing [36], and in computer vision algorithms for characterizing a shape [10]. In this work, we will use the transform to calculate heart wall movement, and we are using the three-dimensional Euclidean vector distance transform.

We have to treat each volume in the heart cycle separately. The 3D surface resulting from a contour extraction algorithm, is used to define a binary space (in our case, a cuberille). We have the binary mapping: $S(\mathbf{x}) : \ \mathbb{N}^3 \longrightarrow \{0, 1\}$, and we define the set $A_S = \{\mathbf{x} \in \mathbb{N}^3 \mid S(\mathbf{x}) = 1\}$. Then, the endocardial surface is the *feature* in this space, defined as $F_S = \{\mathbf{x} \in \mathbb{N}^3 \mid \mathbf{x} \in A_S \ \wedge \ \exists \mathbf{y} \in N(\mathbf{x}) \ \text{ with } \ S(\mathbf{x}) = 0\}$. The neighbor operator $N(\mathbf{x})$ defines the $3 \times 3 \times 3$ neighborhood of $\mathbf{x}$.

The vector distance transform is a mapping giving the vector space $\mathbf{L}(F_S^C)$, where F_S^C is the complement of F_S. For each point $\mathbf{x} \in F_S^C$, we have a corresponding point in $\mathbf{L}(F_S^C)$, which is a vector: $\mathbf{L}(\mathbf{x}) = \vec{z}$. This vector is given by the minimum distance to the feature F_S:

$$\mid \vec{z} \mid = \min_{\mathbf{y} \in F_S} (d[\mathbf{x}, \mathbf{y}]). \tag{1}$$

Here we are using the Euclidean metric. This is illustrated in Fig. 2(a).

The implementation is based on the work by Ye [36] and Mullikin [28]. We use a 6-neighbor 3D mask, i.e., the non-diagonal neighbors, where each element contains the coordinates relative to the center of the mask. For implementation efficiency, the mask is split into a set of six sub-masks, letting us use lookup-tables during execution and reducing the complexity by using a six-pass algorithm. These masks acts as a kind of convolution masks, running over the cuberille and incrementing a distance counter. The calculation is still quite computational intensive and there is a lot to gain in reducing the area of interest as much as possible.

The errors reported by using this algorithm are so small that they have no practical consequences in this application. We have tried with varying mask sizes, and have concluded that it Is sufficient to use a six neighbor mask structure. However, we must be aware not to let the outer limits of the cuberille produce errors when the feature points lay close to these limits.

2.4 3D wall dynamics

In order to calculate the wall motion, we extend our notation to include the temporal dimension. The vector space is then represented by $\mathbf{L}(\mathbf{x}, t_i)$, where i is typically in the

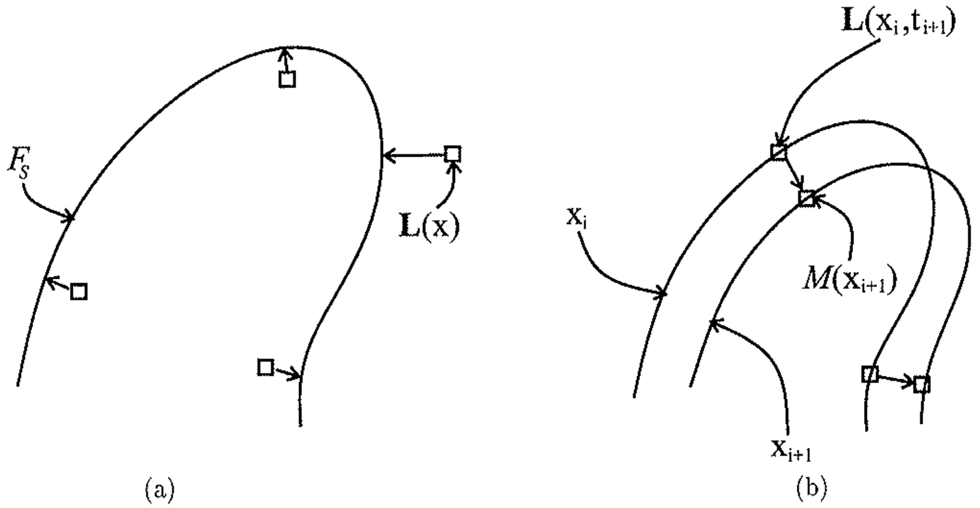

Figure 2: (a) The distance transform gives a vector field with vectors pointing at the feature. (b) Wall motion vectors are calculated for two successive frames, and the vector magnitude is stored at the feature location.

range 10..20. The number of volume frames depends on the heart rate, and the frame rate and motor speed capabilities of the equipment. The feature at frame i is then given by $\mathbf{x}_i \in F_{S,t_i}$. As illustrated in Fig. 2(b), we now find the endocardial surface movement by considering two consecutive vector spaces. To calculate the movement at frame $i+1$, we use the feature point indexes at frame i to extract the correct vector for frame $i+1$. The length of this vector is mapped into the motion space by the function M at the feature points for frame $i+1$:

$$M(\mathbf{x}_{i+1}) = \mid \mathbf{L}(\mathbf{x}_i, t_{i+1}) \mid . \tag{2}$$

The velocity in mm/sec can now be calculated by using the number of frames and image resolution. By repeating this operation for each cuberille, we get a series of surfaces with values describing the movement from one frame to the next.

In order to visualize the surface data, we surface render each cuberille creating a cineloop of the moving surface color coded with the velocity information. We create a color map where blue indicates expanding motion and red indicates contraction. The saturation of the colors is reduced with decreasing velocity ending up with gray for no movement.

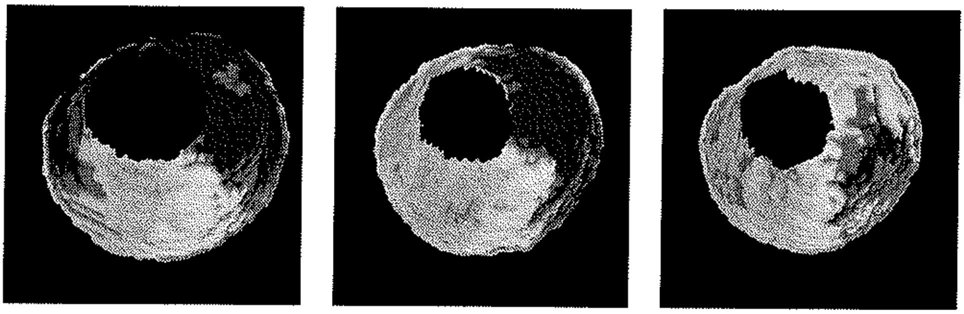

Figure 3: Surface rendering of a balloon at three different time steps.

3 Results

Volume rendering of ultrasonic data has attracted much interest as acquisition of multidimensional ultrasound data has become more feasible. The properties of the ultrasonic images differ significantly from other medical modalities such as MRI, X-CT and PET, and rendering techniques must incorporate the noisy nature of the ultrasound signals. In the application presented here, we use standard surface rendering techniques applied directly on the surface volumes.

In order to verify our algorithms, we collected a series of volume data from a water filled balloon in a water tank. The transducer was mounted in a device, and the balloon had a well defined form and was given different volumes generating a simulated heart cycle. Examples of the resulting velocity renderings are shown in Fig. 3. The rendering view is the same as looking down into a cup. The upper, right part is contracting while the lower, left part is first contracting and then expanding. This is in agreement with the qualitative and quantitative information we had.

Applied on real 4D ultrasound data, we get images as in Fig. 4. This sequence is taken from a cineloop showing the contraction of the right atrium. Playing the cineloop, we clearly see regional parts of the endocard contracting faster than others. The blue color indicates contractive movement, and red color expanding movement. The visualization is intuitive, and by changing the rendering view parameters, e.g., clipping, viewpoint and perspective, we can improve the quality of the visualization. This method has the obvious advantage that a whole 3D region is displayed and regions of dysfunctional tissue can be observed in relation to surrounding structure.

4 Discussion

In this work we have explored the possibilities of calculating and visualizing 3D wall motion in multidimensional echocardiographic data. The characteristics of these data depend on ultrasound beam scale resolution, scanner frame-rate, the 3D motor speed, the patient heart rate and desired time resolution. What we struggle for in ultra-

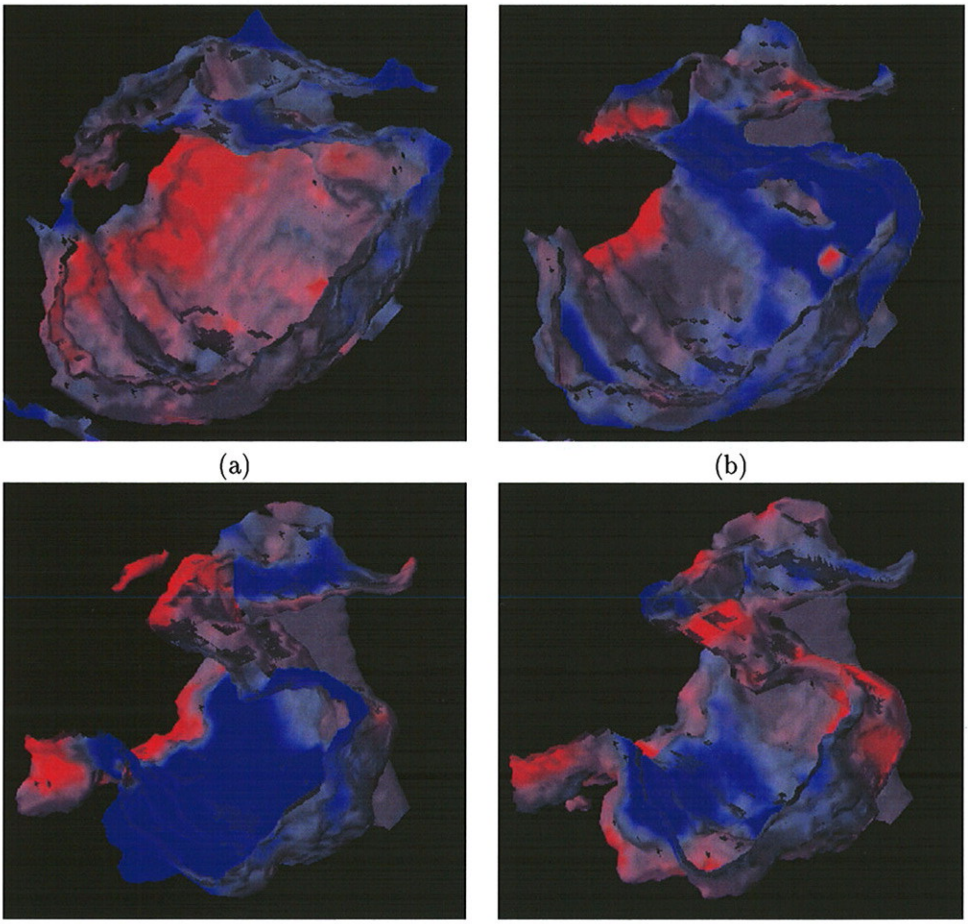

(a) (b)

(c) (d)

Figure 4: Surface rendering of the right atrium wall motion. Blue indicates contraction, and red expansion.

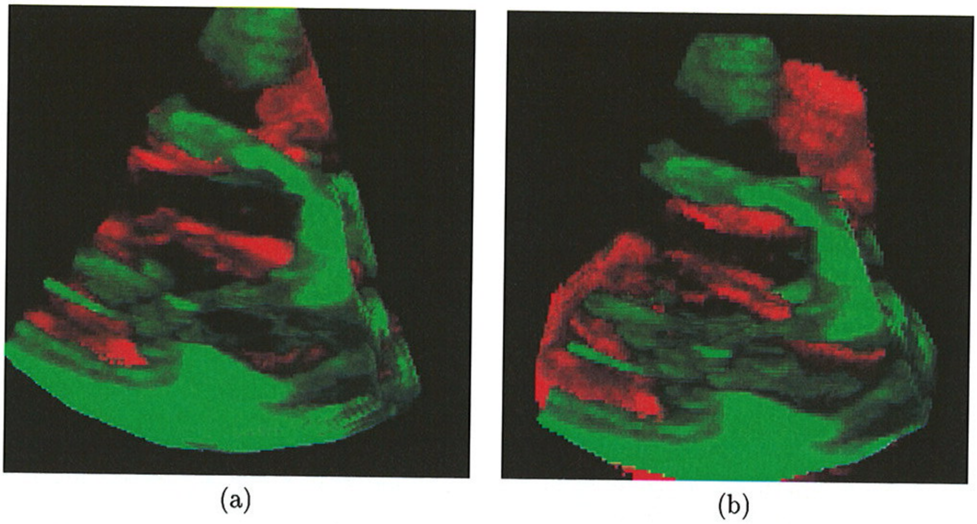
(a) (b)

Figure 5: Volume rendering of the left ventricle from a transthoracic acquisition. Green is end-diastole, and red is late systole. (a) No compensation. (b) With axis compensation.

sound imaging is higher resolution, making the amount of data to process in our 4D ultrasound pipeline quite large. The evolution of the digital ultrasound scanners will enable specialized image processing operations to be performed by dedicated hardware. Improvements in acquisition technology will also change the post-processing requirements.

We have shown that quantitative 3D ultrasound is possible. Working correctly, the 3D wall motion technique presented here is superior to quantitative analysis performed in 2D echocardiography. It simplifies the diagnosis by the intuitive visualization which improves the understanding of the wall movement. Ideally, infarcted regions can be localized in three dimensions. However, the method relies heavily on the edge detection algorithms, and we face the same problems regarding cardiac translation and rotation. One way to approach these problems is to incorporate a geometrical correction method. This is shown to be useful in 2D echocardiography. By using an acquisition setup as in Fig. 1, we interactively marked the main axis for the end-diastolic and end-systolic ventricle, interpolated the mid-frames, and then aligned the volumes according to these lines. Fig. 5 shows the lower part of the left ventricle with aortic valves where we have adopted a color coding technique evaluated by Bates et al. [6], extended into 3D by using a volume rendering technique. Here, the heart frames are displayed in relation to the end-diastolic frame which is colored with a different color. Fig. 5(a) is the normal display and Fig. 5(b) when using geometrical correction. The translation (in 3D) is eliminated, and the true contraction is displayed. We will in the future focus on the clinical applicability of the method, and we have to overcome the acquisition difficulties in 4D echocardiography.

5 Acknowledgments

The authors would like to thank Vingmed Sound and the Norwegian Research Council for supporting this study. Thanks to Prof. Hans Torp, Dept. Physiology and Biomedical Engineering, University of Trondheim, for help in the laboratory experiments, and to TomTec GmbH, Germany for the cooperation.

References

1. A. A. Amini, T. E. Weymouth, and R. C. Jain. Using dynamic programming for solving variational problems in vision. *IEEE Trans on Pattern Analysis and Machine Intelligence*, 12(9):855–867, Sept. 1990.

2. B. A. J. Angelsen. *Waves, signals and signal processing in medical ultrasonics. Volume I.* NTNU, Dept. of Physiology and Biomedical Engineering, The Norwegian University of Science and Technology (NTNU), Trondheim, Norway, 1995.

3. P. E. Assmann, C. J. Slager, et al. Quantitative echocardiographic analysis of global and regional left ventricular function: A problem revisited. *J Am Soc Echocardiogr*, 3(6):478–487, 1990.

4. P. E. Assmann, C. J. Slager, et al. Comparison of models for quantitative left ventricular wall motion analysis from two-dimensional echocardiograms during acute myocardial infarction. *Am J Cardiol*, 71:1262–1269, June 1993.

5. L. Axel, R. C. Gonçalves, and D. Bloomgarden. Regional heart wall motion: Two-dimensional analysis and functional imaging with MR imaging. *Radiology*, 183(3): 745–750, 1992.

6. J. R. Bates et al. Color coding of digitized echocardiograms: Description of a new technique and application in detecting and correcting for cardiac translation. *J Am Soc Echocardiogr*, 7(4):363–369, 1994.

7. S. Berg, A. H. Torp, K. P. Schipper, and B. Olstad. Real-time quantitative wall motion coding in two-dimensional echocardiography. In *Proc. of SPIE Medical Imaging*, volume 2709, pages 413–423, Newport Beach, 1996.

8. H.-G. Blaas, S. Eik-Nes, T. Kiserud, S. Berg, B. Angelsen, and B. Olstad. Three-dimensional imaging of the brain cavities in human embryos. *Ultrasound Obstet Gynecol*, 5:228–232, Apr. 1995.

9. G. Borgefors. Distance transform in arbitrary dimensions. *Computer vision, graphics, and image processing*, 27:321–345, 1984.

10. G. Borgefors. Centres of maximal discs in the 5-7-11 distance transform. In *Proc. of the 8th Scand. Conf. on Image Analysis, Tromsø, Norway*, volume 1, pages 105–111, May 1993.

11. J. F. Brinkley, W. E. Moritz, and D. W. Baker. Ultrasonic three-dimensional imaging and volume from a series of arbitrary sector scans. *Ultrasound Med Biol*, 4(4):317–327, 1978.

12. P. Danielsson. Euclidean distance mapping. *Computer Graphics and Image Processing*, 14:227–248, 1980.

13. C. Di Mario, C. von Birgelen, F. Prati, et al. Three dimensional reconstruction of cross sectional intracoronary ultrasound: clinical or research tool? *Br Heart J*, 73:26–32, 1995.

14. C. L. Donovan, W. F. Armstrong, et al. Quantitative Doppler tissue imaging of the left ventricular myocardium: Validation in normal subjects. *Am Heart J*, 130 (1):100–104, 1995.

15. D. Fine, D. Sapoznikov, M. Mosseri, and M. S. Gotsman. Three-dimensional echocardiographic reconstruction: qualitative and quantitative evaluation of ventricular function. *Comput Methods Programs Biomed*, 26:33–44, 1988.

16. T. Force and A. F. Parisi. Quantitative methods for analyzing regional systolic function with two-dimensional echocardiography. *Echocardiography A review of cardiovascular ultrasound*, 3(4):319–331, 1986.

17. E. A. Geiser, M. Ariet, D. A. Conetta, S. M. Lupkiewicz, L. G. Christie Jr, and C. R. Conti. Dynamic three-dimensional echocardiographic reconstruction of the intact human left ventricle: Technique and initial observations in patients. *Am Heart J*, 103(6):1056–1065, 1982.

18. E. A. Geiser, S. M. Lupkiewicz, L. G. Christie, M. Ariet, D. A. Conetta, and C. R. Conti. A framework for three-dimensional time-varying reconstruction of the human left ventricle: sources of error and estimation of their magnitude. *Comput Biomed Res*, 13:225–241, 1980.

19. O. Gilja, N. Thune, K. Matre, T. Hausken, S. Ødegaard, and A. Berstad. In vitro evaluation of three dimensional ultrasonography in volume estimation of abdominal organs. *Ultrasound Med Biol*, 20(2):157–165, 1994.

20. D. Jurkovic, A. Geipel, K. Gruboeck, E. Jauniaux, M. Natucci, and S. Campbell. Three-dimensional ultrasound for the assessment of uterine anatomy and detection of congenital anomalies: a comparison with hysterosalpingography and two-dimensional sonography. *Ultrasound Obstet Gynecol*, 5:233–237, Apr. 1995.

21. M. Kass, A. Witkin, and D. Terzopoulos. Snakes: Active contour models. *International Journal of Computer Vision*, 1(4):321–331, 1988.

22. A. Lee, A. Kratochwil, J. Deutinger, and G. Bernaschek. Three-dimensional ultrasound in diagnosing phocomelia. *Ultrasound Obstet Gynecol*, 5:238–240, Apr. 1995.

23. J. Mæhle, K. Bjoernstad, S. Aakhus, H. G. Torp, and B. A. J. Angelsen. Three-dimensional echocardiography for quantitative left ventricular wall motion analysis. *Echocardiography Am Jrnl of CV Ultrasound & Allied Tech*, 11(4):397–408, 1994.

24. R. W. Martin et al. Ventricular volume measurement from a multiplanar transesophageal ultrasonic imaging system: An in vitro study. *IEEE Trans Biomed Engin*, 37(5):442–449, 1990.

25. M. Matsumoto, M. Inoue, S. Tamura, K. Tanaka, and H. Abe. Three-dimensional echocardiography for spatial visualization and volume calculation of cardiac structures. *J Clin Ultrasound*, 9:157–165, 1981.

26. E. Merz, F. Bahlmann, and G. Weber. Volume scanning in the evaluation of fetal malformations: a new dimension in prenatal diagnosis. *Ultrasound Obstet Gynecol*, 5:222–227, Apr. 1995.

27. W. Moritz et al. Computer generated three-dimensional ventricular imaging from a series of two-dimensional ultrasonic scans. *IEEE: Computers in Cardiology*, pages 19–24, 1982.

28. J. Mullikin. The vector distance transform in two and three dimensions. *CVGIP: Graphical Models and Image Processing*, 54(6):526–535, Nov. 1992.

29. B. Olstad, S. Berg, A. Torp, K. Schipper, and S. Eik-Nes. 3D transvaginal ultrasound imaging for identification of endometrial abnormality. In *Proc. of SPIE Medical Imaging*, volume 2432, pages 543–553, San Diego, 1995.

30. A. Salustri and J. Roelandt. Three dimensional reconstruction of the heart with rotational acquisition: methods and clinical applications. *Br Heart J*, 73:10–15, 1995.

31. H. Sawada, J. Fujii, K. Kato, M. Onoe, and Y. Kuno. Three dimensional reconstruction of the left ventricle from multiple cross sectional echocardiograms. *Br Heart J*, 50:438–442, 1983.

32. I. Schnittger, P. J. Fitzgerald, et al. Computerized quantitative analysis of left ventricular wall motion by two-dimensional echocardiography. *Circulation*, 70(2): 242–254, 1984.

33. E. Steen and B. Olstad. Volume rendering of 3D medical ultrasound data using direct feature mapping. *IEEE Trans on Medical Imaging*, 13(3):517–525, Sept. 1994.

34. H. Torp. *Signal processing in real-time, two-dimensional Doppler color flow mapping.* PhD thesis, Department of Physiology and Biomedical Engineering, Faculty of Medicine, The University of Trondheim, 1990.

35. F. P. van Rugge et al. Magnetic resonance imaging during dobutamine stress for detection and localization of coronary artery disease. *Circulation*, 90(1):127–138, 1994.

36. Q. Ye. The signed Euclidean distance transform and its applications. In *Proc. of the 9th Int. Conf. on Pattern Recognition, Rome*, pages 495–499, 1988.

37. A. A. Young and L. Axel. Three-dimensional motion and deformation of the heart wall: Estimation with spatial modulation of magnetization - a model-based approach. *Radiology*, 185:241–247, Oct. 1992.

Paper F

Ultrasound in Med. & Biol., Vol. 25, No. 5, pp. 745–753, 1999

0301-5629/99/$–see front matter

ELSEVIER

PII S0301-5629(99)00012-5

● *Original Contribution*

DYNAMIC THREE-DIMENSIONAL FREEHAND ECHOCARDIOGRAPHY USING RAW DIGITAL ULTRASOUND DATA

SEVALD BERG,[†] HANS TORP,[†] DITLEF MARTENS,[‡] ERIK STEEN,* STEIN SAMSTAD,[†]
INGE HØIVIK* and BJØRN OLSTAD*
[†]Department of Physiology and Biomedical Engineering, Norwegian University of Science and Technology, Trondheim, Norway; [‡]Christian Michelsen Research, Bergen, Norway; and *Vingmed Sound AS, Horten, Norway

(*Received* 3 *September* 1998; *in final form* 13 *January* 1999)

Abstract—In this paper, we present a new method for simple acquisition of dynamic three-dimensional (3-D) ultrasound data. We used a magnetic position sensor device attached to the ultrasound probe for spatial location of the probe, which was slowly tilted in the transthoracic scanning position. The 3-D data were recorded in 10–20 s, and the analysis was performed on an external PC within 2 min after transferring the raw digital ultrasound data directly from the scanner. The spatial and temporal resolutions of the reconstruction were evaluated, and were superior to video-based 3-D systems. Examples of volume reconstructions with better than 7 ms temporal resolution are given. The raw data with Doppler measurements were used to reconstruct both blood and tissue velocity volumes. The velocity estimates were available for optimal visualization and for quantitative analysis. The freehand data reconstruction accuracy was tested by volume estimation of balloon phantoms, giving high correlation with true volumes. Results show *in vivo* 3-D reconstruction and visualization of mitral and aortic valve morphology and blood flow, and myocardial tissue velocity. We conclude that it was possible to construct multimodality 3-D data in a limited region of the human heart within one respiration cycle, with reconstruction errors smaller than the resolution of the original ultrasound beam, and with a temporal resolution of up to 150 frames per second. © 1999 World Federation for Ultrasound in Medicine & Biology.

Key Words: **Three-dimensional ultrasound, Echocardiography, Magnetic position sensor, Freehand acquisition.**

INTRODUCTION

The great potential of three-dimensional (3-D) medical ultrasound imaging has led to a considerable amount of research in this area. The ability to process structures from ultrasound as 3-D objects is exploited in most fields where ordinary two-dimensional (2-D) ultrasound is used. Usually, the acquisition is done by moving an ordinary 2-D probe in a predefined manner (*e.g.*, by rotation or translation), and then combining these slices into a 3-D dataset. These data can be analyzed both qualitatively and quantitatively. Realistic images of fetal malformations have been rendered (Merz et al. 1995), brain cavity volumes of embryos have been estimated (Blaas et al. 1998), as well as volumes of abdominal organs (Gilja et al. 1995).

The image quality is reduced by patient movement (particularly for the fetus) or inaccurate probe movement. The accessibility is limited because the probe is not allowed to move freely, resulting in nonoptimal object definitions. The intrinsic properties of ultrasound images consisting of speckle and reverberation noise, or shadowing artefacts, makes 3-D visualization even more difficult. For the most part, video-grabbed signals from ultrasound scanners are used in freehand 3-D imaging. These signals have lower spatial and temporal resolutions than the actual ultrasound beams.

The development of 2-D transducer arrays for ultrasound volume acquisition has resulted in scanners capable of recording 3-D volumes real-time (Smith et al. 1991). Stroke volume estimation has been reported with this technique (Shiota et al. 1998), but there are limitations to these systems regarding spatial and temporal resolutions and hardware complexity. However, in the future, this technique will probably play an important role in image acquisition.

Today, the state-of-the-art method for dynamic 3-D ultrasound acquisition of the heart is by rotating the probe one small step for each cardiac cycle. The 2-D

Address correspondence to: Sevald Berg, Dept. of Physiology and Biomedical Engineering, Norwegian University of Science and Technology, N-7489 Trondheim, Norway. E-mail: sevald@idi.ntnu.no

slices are reorganized according to their positions in the cycle, and a set of 3-D ultrasound volumes is generated. Successful dynamic rendering of valves can be performed using commercially-available systems (Salustri et al. 1996). For optimal quality, cardiac cycles can be rejected if they deviate too much from the normal cycles. The acquisition time for this method is long, which necessitates respiration gating. The total acquisition time can be more than 3 min, augmenting the risk of motion artefacts. The predefined rotation path results in access problems when the probe is positioned between two ribs. In addition, when digitizing the video output signal from the scanner, the data will suffer from several limitations that degrade the reconstruction and reduce the clinical value: 1. Low frame rate (25 frames per second for the PAL video standard) that introduces jitter artifacts, and low accuracy in reconstruction of rapidly moving valves. 2. Reduced image resolution reduces the quality of the ultrasound volume. 3. Large data storage is needed because the data are stored in a scan-converted format. This also increases the computer performance requirements for postprocessing. 4. Reduced postprocessing flexibility because reconstruction algorithms using direct 3-D scan conversion are not possible. 5. Analyzing Doppler velocities quantitatively is not possible because the exact Doppler measurements cannot be extracted from the video data.

The introduction of position-sensing devices for freehand volume acquisition provides a flexible alternative to the rotational devices. The ultrasound probe is coupled to a sensor that registers the spatial coordinates inside a magnetic field. Already, in the early 1980s, both acoustical and mechanical position locator devices were used for ultrasound volume imaging (Geiser et al. 1982; Moritz et al. 1983). Recently, this methodology regained interest by the advances in computer and ultrasound scanner technology and the development of accurate magnetic locator systems (Detmer et al. 1994; Hughes et al. 1996). King et al. (1990) have built a system based on an acoustic sensor with interactive feedback during acquisition. Quantization of heart volume and mass using position locator systems has been reported to give high precision and good reproducibility (Barry et al. 1997; Gopal et al. 1993; Leotta et al. 1997b).

In this paper, we present a method for freehand dynamic echocardiographic acquisition and reconstruction using raw digital ultrasound data. The high temporal resolution from the scanner data was preserved in the 3-D reconstructions, and the spatial reconstruction errors were smaller than the ultrasound beam resolution. The raw data provided total flexibility in the postprocessing of the data consisting of radiofrequency (RF) samples, grey-level tissue values, or Doppler velocities used for color-flow imaging (CFI) (Kasai et al. 1985), tissue Doppler imaging (TDI) (Miyatake et al. 1995) or strain rate imaging (SRI) (Heimdal et al. 1998).

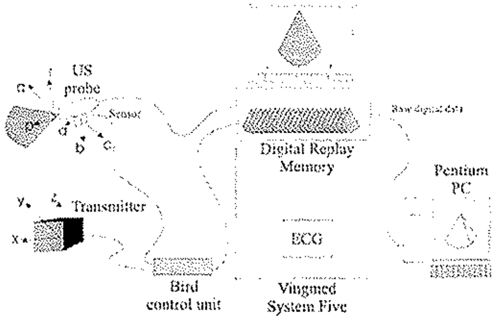

Fig. 1. The data acquisition setup. The Bird control unit was coupled directly to the scanner, which outputs raw digital data for postprocessing. The individual reference systems used in the calibration are indicated on each device.

First, the data acquisition is described, followed by a brief description of the position sensor calibration. The volume reconstruction algorithm is described in detail, together with an analysis of the spatial and temporal resolutions. Then, the reconstruction accuracy of water tank phantoms is evaluated by volume measurements. Examples of *in vivo* transthoracic 3-D cardiac reconstructions of tissue, CFI and TDI are given.

MATERIALS AND METHODS

Data acquisition

The data were acquired using a System Five digital ultrasound scanner (Vingmed Sound, Horten, Norway). The position sensor system was a Flock of Birds (Ascension Technology Corp., Burlington, VT), consisting of a magnetic field transmitter and a sensor (receiver) that was mounted directly on a standard ultrasound probe with a 2.5-MHz or 3.5-MHz phased array transducer. The transmitter and receiver were both coupled to an electronic control unit, and the receiver had to be located inside the magnetic field of the transmitter. Three translational and three rotational position vector components were generated by the control unit. The optimal operating range of the sensor was 25–60 cm from the transmitter (Leotta et al. 1997a). As illustrated in Fig. 1, the control unit was coupled directly to the scanner, where the sensor position coordinates were sampled at 100 positions/s, and stored in the digital replay memory (frame buffer) together with the corresponding image frames. All other relevant scanner parameters, including the ECG signal from the patient, were also recorded simultaneously. The data flow is shown in Fig. 2.

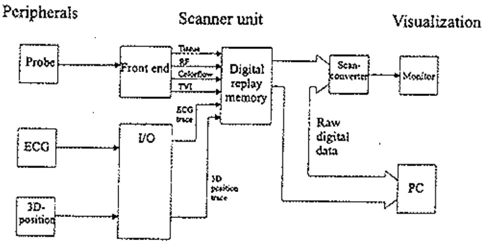

Fig. 2. The data flow diagram. Data from the probe, the ECG and the Bird were collected and stored in the digital replay memory in the scanner. The data were transferred to an external PC as individual beam samples before scan conversion.

For a typical left ventricle acquisition, the probe was placed apically between two ribs and then tilted slowly, covering the area of interest (Fig. 3). The total recording was done during suspended end-expiration, and lasted typically for 10–20 cardiac cycles. This was sufficient for constructing 3-D volumes of the ventricle. The data were sampled continuously all the time, so the operator did not have to interact to start a recording. When the 3-D recording was finished, the scanner frame buffer data, which represented the tilted movement, were transferred to an external computer for postprocessing.

Position sensor calibration

The position vector output from the Bird control unit had to be calibrated against the ultrasound scan plane orientation. Different calibration procedures and phantoms have been described for this purpose (Detmer et al. 1994; Prager et al. 1998). Common for all methods is to image a known geometrical structure in the phantom, and to identify positions in this structure in the ultrasound image. We used a calibration phantom consisting of a fixed jagged membrane with five corners in a water bath (Fig. 4). To identify the five corners of the phantom, we sampled the positions by pointing at them with a precalibrated pointer attached to the Bird sensor. The sensor position and orientation (a, b, c), were measured in the transmitter coordinate system (x, y, z) (see Fig. 1). We then had to find the transformation from the coordinate system (p, q, r) of the ultrasound scan plane to the sensor coordinate system (a, b, c). The sensor was mounted on the probe with the 2-D scan plane positioned in the plane of the membrane. The five fixed positions on the membrane were identified in the ultrasound image. The same five points were identified in the physical phantom with the precalibrated pointer. The transformation between the coordinate systems (p, q, r) and (a, b, c) was found from the pseudo-inverse of the position matrices.

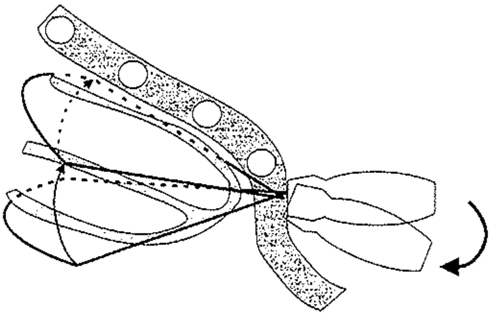

Fig. 3. The probe was tilted slowly during 10–20 cardiac cycles in suspended end-expiration.

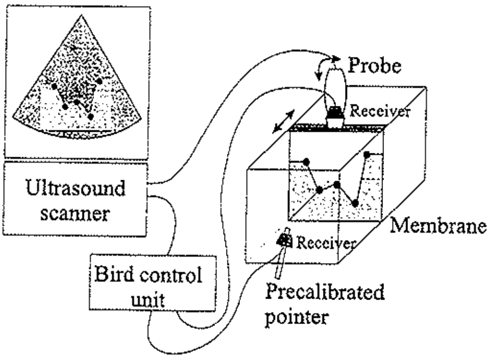

Fig. 4. The calibration phantom with the jagged membrane and the holder for the ultrasound probe. The precalibrated pointer is used to identify the five points on the phantom.

Phantom setup

To verify the reconstruction accuracy, volume estimations of a series of water-filled balloon phantoms were performed. The water had a temperature of 33°C, which resulted in a sound velocity close to the ultrasound scanner setting (1540 m/s). After each 3-D volume acquisition, the balloons were weighed, emptied, and reweighed. The weight difference gave the actual weight of the water. At this temperature, the water mass density was 0.9939 g/mL. Using manual segmentation in consecutive, parallel slices, a volume was built up by a triangulation process. This volume estimation technique has been described and verified by other authors, and the traces were outlined in the center of the balloon edge (Gilja et al. 1994; Thune et al. 1996).

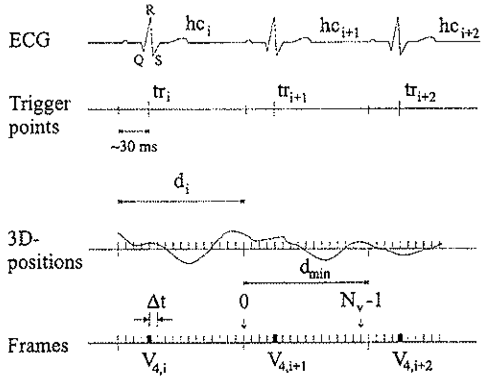

Fig. 5. The system traces used in the volume reconstruction. The trigger points, tr_i, were found from the QRS complex in the ECG signal. The reconstructed cardiac cycle had its starting position right in front of the P-wave. The number of frames used in each cycle was given by the length of the shortest cycle, $d_{\min}$. The frames used for reconstruction of the fourth volume, V_4, are marked out. The 3-D position trace indicates that the probe position and orientation in space were continuously recorded during the scanning.

Volume reconstruction and resolution

The raw digital data from the scanner frame buffer were transferred to a standard Pentium PC for postprocessing. The 2-D scan plane resolution was up to 512 samples for each beam, with up to 128 beams. Because the frames were stored in a raw format (*i.e.*, before scan conversion), the file size was reduced to a minimum. Typically, the amount of data was between 20–50 Mb, depending on the frame rate, the data type (tissue or color flow) and the number of cardiac cycles used.

The data were reorganized, scan-converted into regular geometries, and visualized using the EchoPAC-3-D software (Vingmed Sound, Horten, Norway). As illustrated in Fig. 5, the cardiac cycles are labeled hc_i, $i \in [0, N_c - 1]$, where N_c is the total number of cycles. The ultrasound scanner calculated one trigger point from the QRS complex, tr_i, which was stored together with the corresponding image frame. Based on these trigger positions, the individual frames were reorganized so that each frame located at the same position relative to the trigger point was combined into one unit:

$$V_j = \bigcup_i V_{j,i} \quad j \in [0, N_v - 1],\ i \in [0, N_c - 1], \tag{1}$$

where N_v is the total number of 3-D volumes. V_j represents the 3-D ultrasound volume at time position j. Unfortunately, the duration of each cardiac cycle, d_i, is not constant. The number of 3-D volumes, N_v, was made dependent on the length of the minimal cardiac cycle, $d_{\min}$. Recorded frames outside this range were discarded. Most of the cardiac cycle length variations were due to variations of diastole, before atrial contraction. In this phase, the heart movement was minimal and least sensitive to frame removal. Thus, the starting point for each cycle was defined right before the P-wave, about 30 ms before the trigger point (adjustable). When fr is the frame rate, we get:

$$N_v = d_{\min} \cdot fr = \min_i \{d_i\} \cdot fr = \min_i \{tr_{i+1} - tr_i\} \cdot fr. \tag{2}$$

The probe was tilted in a fan-like manner, shown in Fig. 3. The pace of this motion and the patient heart rate decided the sampling density for each volume (*i.e.*, the distance between the 2-D frames). The temporal resolution was the inverse of the frame rate: $\Delta t = 1/fr$. This was both the resolution between each recorded 2-D frame and between each reconstructed 3-D volume. If the probe was tilted with an average velocity v (degrees/s) during the cycle hc_i, the distance between two frames in the reconstructed volume was $\Delta w_i = v \cdot d_{\min}$ (degrees). As indicated in Fig. 5, frame number four after each starting point contributed to volume number four, V_4.

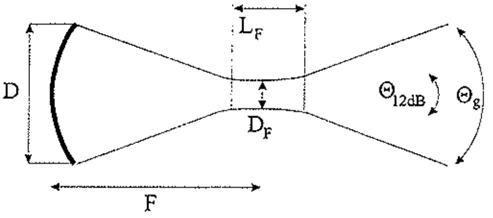

Fig. 6. The focusing of the ultrasound beam. D is the aperture diameter, F is the focal length, $\Theta_{12\text{dB}}$ is the dual sided opening angle where the amplitude has fallen 12 dB off from the axial value, Θ_g is the geometrical opening angle, D_F is the focal diameter, and L_F is the depth of focus (the focal zone).

Another important factor influencing the resolution of the reconstructed volume is the property of the ultrasound beams. By analyzing the beam resolution, we can get an idea of the resolution to expect in 3-D imaging. The ultrasound beam propagates in three dimensions where the radial direction is along the beam, the azimuth direction is in the scanning plane and normal to the beam, and the elevation direction is normal to the scanning plane and normal to the beam. For the phased-array transducer, the depth of focus in the elevation direction is constant and, in Fig. 6, the focusing of the beam is illustrated. At a given focus F, the ultrasound beam resolution, D_F, is given by:

$$D_F = \Theta_{X\,\mathrm{dB}} \cdot F = k_{X\,\mathrm{dB}} \cdot \frac{\lambda}{D} \cdot F, \tag{3}$$

where $\Theta_{X\,\mathrm{dB}}$ is the the opening angle defined by the X dB beam amplitude reduction, as illustrated in the figure. We used 12-dB reduction, defining the lower amplitude value limit. Furthermore, λ is the ultrasound wavelength, and D is the aperture diameter. The parameter $k_{X\mathrm{dB}}$ is the amplitude reduction factor and, for 12-dB reduction, we get $k_{12\mathrm{dB}} = 1.2$ (Angelsen 1995). The depth of focus, L_F, is defined as the region where the beam diameter is limited by diffraction, and can be expressed as where the on-axis beam amplitude has dropped 1 dB:

$$L_F(1\ \mathrm{dB}) = 2 \cdot D_F(12\ \mathrm{dB}) \cdot \frac{F}{D}. \tag{4}$$

The next step was to convert each volume into a regular geometry, which easily could be manipulated by different visualization tools. This consisted of scan-converting all beam samples into a grid of voxels, and interpolating to fill in the gaps. The interpolation was done in two ways, depending on the angle between the 2-D scan planes. If the maximum angle between two scan planes was less than 20°, a simple linear interpolation was used. The interpolation direction was set orthogonal to the scan plane in the middle. If the maximum angle was greater than 20°, another method was used, where each 2-D scan plane had a certain thickness that defined the region where it contributed to the interpolation. Each point in space that was located inside one or more such regions was interpolated using a linear weight, decreasing with the distance to the scan plane (Fig. 7). If several regions were overlapping, an average of the sum of weights was used.

Tissue visualization

The volume reconstruction was performed within 2 min after the data transfer. The user could interactively browse the ultrasound volumes by selecting individual frames and time positions. These slices cut the volume in random positions and were displayed as cineloops cycling through the cardiac cycle. Volume rendering is another technique to project 3-D information onto a 2-D image (Steen and Olstad 1994). Realistic 3-D images of the tissue surface is possible by using surface-shading methods. Dynamic 3-D rendering of heart valves is described below.

Doppler visualization

Ultrasound color flow imaging (CFI) estimates the blood velocity vector component along the ultrasound beam and displays the velocity values as a color-coded overlay on the tissue image. To measure the correct blood flow velocity with 2-D ultrasound, the probe should be placed so that the ultrasound beams are as parallel to the flow direction as possible. This also applies for 3-D acquisition. In the examples in this paper, an apical position was used for the left ventricle mitral and aortic flow. The Doppler samples consisted of the pulse-to–pulse complex autocorrelation function values. Spatial interpolation and averaging were performed on the raw Doppler and tissue values separately. The Doppler values were then given colors, reflecting the signal frequency, power and bandwidth, and combined with the tissue signal properly to define the flow region. The data were visualized by interactively selecting different 2-D slices from the volume. It is important to note that the colors were proportional to a given blood velocity in the direction of the ultrasound beams. If the 2-D slice was selected orthogonal to the scanning direction, the velocity vectors were directed in or out of the slice.

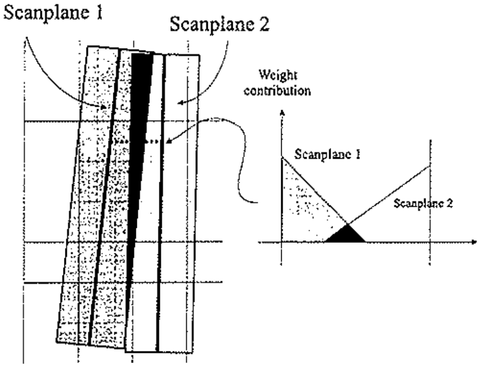

Fig. 7. The interpolation between two image planes, shown here as a cross-section (thick lines), was done by defining a region where the plane contributed to the interpolation. The values along the dotted line were weighted by the distance from the planes.

Using the same Doppler principle as with CFI, the tissue velocity can be estimated by adjusting the velocity range to typical muscular movement velocities (10 cm/s). The 3-D TDI reconstruction is similar to 3-D CFI. The colors represent the tissue velocity in the direction of the ultrasound beams.

RESULTS

All examples of *in vivo* cardiac reconstructions are from healthy adults.

Reconstruction resolution

In our setup, the spacing between two beams was 0.4 times the beam width. Table 1 summarizes the data

Table 1. Elevation beam resolution values for the 2.5-MHz and 3.5-MHz phased-array transducers.

Transmit frequency (f)	2.5 MHz	3.5 MHz
Wavelength (λ)	0.616 mm	0.440 mm
Elevation aperture (D)	13.0 mm	13.0 mm
Elevation focus (F)	60.0 mm	60.0 mm
Focal depth, L_F (1 dB)	31.4 mm	22.2 mm
Beam width at focus, D_F (12 dB)	3.4 mm	2.4 mm
Plane distance at depth F	1.4 mm	1.0 mm
n planes per 10 mm at depth F	7.1	10.0
Plane distance at depth $2 \times F$	5.2 mm	5.2 mm
n planes per 10 mm at depth $2 \times F$	1.9	1.9

for the 2.5-MHz and 3.5-MHz phased-array transducers used in this paper. In the elevation focus for the 2.5-MHz probe, the beam width was 3.4 mm, giving an optimal plane distance of $0.4 \cdot 3.4$ mm. To cover a 10-mm distance with this resolution in the elevation direction, we had to sample seven evenly spaced planes (*i.e.*, during seven cardiac cycles). The above resolution could only be achieved in the elevation focal zone. Outside this region, the beam width increased with the distance from the focus and, at $2 \cdot F$, it was equal to the aperture diameter of 13 mm. At this depth, it was sufficient to sample 1.9 planes per 10 mm to obtain maximum resolution. These results show that the accuracy of the position sensor system, which was found to be around 1 mm (Leotta et al. 1997b), was better than the elevation resolution of the ultrasound beam.

Figure 8 shows resolution effects from reconstructed *in vivo* data. The first image is the high-resolution 2-D scan plane image, where the angle between two beams was 0.95°. The image shows an apical long-axis view of the left ventricle in end-systole. The mitral valve is located at 11 cm depth, where the interbeam distance was 1.8 mm. Figure 8b shows the plane perpendicular to the image in Fig. 8a. At this depth, the volume covered 6 cm by 25 image frames, which gave a mean interplane distance of 2.4 mm in the elevation direction. The closed mitral valve structure can be seen, together with the myocardial tissue, at relatively high resolution. Figure 8c shows the same slice as Fig. 8b but, here, the volume covered 7 cm by only 9 image planes, giving a mean interplane distance of 7.8 mm. Here, the myocardial resolution is lower and we have dominating stripes in the image. Because it was difficult to move the probe at a constant speed, a slight oversampling was necessary to ensure optimal quality.

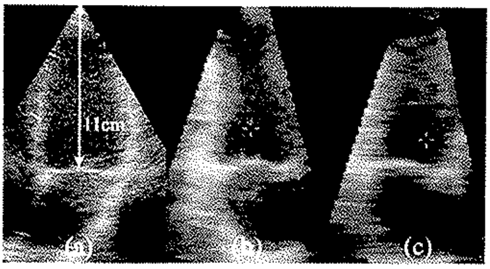

Fig. 8. (a) Original apical four-chamber 2-D slice. The mitral valve is located at 11 cm depth. (b) Slice in the elevation direction with high sampling density. (c) Same slice as (b), but with lower resolution.

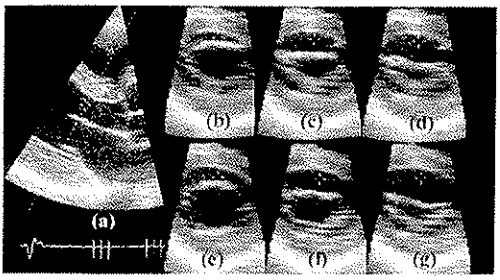

Fig. 9. (a) The original 2-D slice of a parasternal long axis view of the mitral valve. (b)–(g) One slice orthogonal to the azimuth direction (indicated by the dotted line) in six different time steps, giving a short axis view. The time positions are indicated in the ECG trace.

Temporal resolution

The image in Fig. 9a shows a parasternal long axis view of the open mitral valve. This is one of the original 2-D images from a dynamic 3-D recording. Figure 9b–g shows a short axis slice of this volume at six time-steps in the diastole, as shown by the vertical markers in the ECG trace. The spatial position of the slices is indicated by the dotted line. The recording was performed during 14 cardiac cycles, giving a mean distance of 3.5 mm between the scan planes in the area of the valve (8 cm depth). The data consisted of 121 volumes through the cardiac cycle, giving high temporal resolution for valve analysis (9.3 ms). In Fig. 9b–d, the mitral valve is closing after the diastolic filling and, in Fig. 9e–g, the valve is closing after the atrial contraction. We can observe that there are very few reconstruction artefacts, even for the fast-moving mitral valve throughout the whole cardiac cycle.

Position sensor accuracy

Six balloon phantoms (161–601 mL) were used in the *in vitro* recordings. The resulting volumes in milliliters are shown in Table 2. The first column gives the true volumes from the measured weights. The second column is the corresponding estimates from 3-D ultrasound, and

Table 2. Balloon phantom volumes (mL).

Measured volume (mL)	Estimated volume (mL)	Error (%)
161.2	159	−1.4
239.8	239	−0.3
414.9	418	0.7
257.0	260	1.2
372.0	380	2.2
601.4	617	2.6

The first column gives the measured volume from the weight of water. The second column is the corresponding volume estimated from the ultrasound data. The relative error in percent is given in the last column.

the third column is the error in percent between the measured weight and the estimated volume. The mean difference was −4.5 mL, with a standard deviation of 6.5 mL. The errors are small indicating high precision in the reconstruction.

Transthoracic in vivo *cardiac reconstructions*

Tissue morphology. For the 2.5-MHz probe, it was possible to record a tissue volume containing the mitral valve at about 12 cm depth with no loss of temporal resolution. At this depth, the pyramid-shaped volume covered about 7 cm in the azimuth plane and 6 cm in the elevation plane. The total depth of the volume was 10 cm, the temporal resolution was less than 7 ms, and the volume was recorded during 12 cardiac cycles.

In Figs. 10a and b, the surface of the mitral valve tissue in early diastole is visualized by volume rendering. The image in Fig. 10a is seen from the left ventricle and b is from the left atrium. The images were recorded parasternally, with a temporal resolution of 6.7 ms, resulting in a total of 169 volumes. On a 300-MHz Pentium PC, a cineloop of the total cardiac cycle was calculated within 2 min (reconstruction and rendering). Similarly, in Figs. 10c and d, the aortic valve is visualized. The open valve is seen at late systole in Fig. 10c, and the closed valve, in early diastole in Fig. 10d.

Color flow and tissue Doppler imaging. Figure 11a–c shows three almost orthogonal slices through the left ventricle aortic outlet during the outflow in the systole. The image in Fig. 11a shows the flow as given in the original 2-D image. The two dotted lines indicate the position of the images in Figs. 11b and c. Figure 11c shows a cross-section of the aortic flow profile. This image is not possible to reproduce using ordinary 2-D imaging. Figure 12a–c shows cross-sectional images at different positions of the mitral inflow in mid-diastole. Again, the flow vectors are directed in and out of the plane (red and blue), and the images indicates an oval shape of the inflow, which can be explained by the shape of the mitral valve.

Using the apical position as above, similar volumes as in Fig. 12 were reconstructed with TDI data. Figures 13a and b show a cross-section of the left ventricle, giving a short axis view from the start-systole and the mid-diastole, respectively. The color now represents tis-

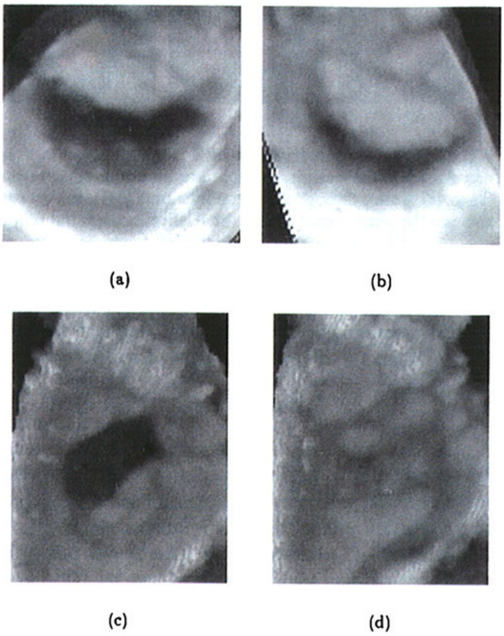

Fig. 10. Surface-shaded volume rendering of the valves. (a) The mitral valve seen from the ventricle. (b) The mitral valve seen from the atrium. (c) The aortic valve open, and (d) closed.

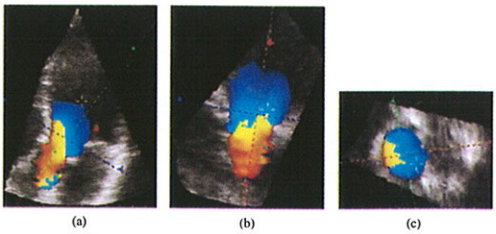

Fig. 11. 3-D color flow images of the aortic outflow during the systole. The dotted lines indicate the slice positions. (a) The original 2-D scan plane. (b) The slice through the green line in (a). (c) The slice through the blue line in (a); here, the velocity vectors are normal to the image.

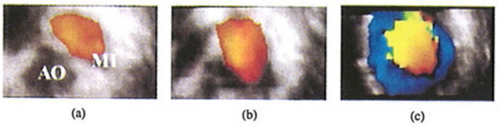

Fig. 12. Cross-sectional images of 3-D mitral color flow in mid-diastole. The velocity vectors are almost normal to the plane. (a) A slice through the mitral inlet tract (MI), and we can also see the aortic outlet (AO). (b) A slice through the mitral orifice. (c) A slice inside the left ventricle.

sue movement in and out of the plane (red and blue). In this example, the temporal resolution was 16.9 ms.

DISCUSSION

Echocardiographic 3-D acquisition and processing has yet to become an everyday clinical tool, mainly due to the complicated recording procedure and the question as to whether 3-D ultrasound improves the diagnosis compared to 2-D ultrasound. We have shown that, with a magnetic position sensor integrated with the ultrasound scanner, 3-D acquisition and reconstruction can be performed in a considerably shorter time than previously described. The clinical value depends on the amount of quantitative information that can be extracted from the data, and the quality of the tissue rendering. Compared to video-based systems, both these factors were improved in the present study using raw digital tissue and Doppler data. The reconstruction accuracy was verified with balloon phantoms, giving estimated volume error of less than 3%, and the accuracy of the Bird was better than the ultrasound beam elevation resolution. Dynamic 3-D data were produced with temporal resolution up to 150 frames/s, and with spatial reconstruction errors smaller than the ultrasound beam resolution. Thus, 3-D volumes were optimally sampled with respect to the beam resolution. But there were other factors that could produce reconstruction errors: 1. Irregular patient movement; 2. Heart beat variability; 3. Jitter artefacts; and 4. Magnetic field distortions.

Fig. 13. 3-D tissue Doppler imaging. Cross-sectional slices through the left ventricle in (a) start-systole and (b) mid-diastole. The tissue velocity vectors are perpendicular to the slices.

Patient movement implies irregular heart movement (*i.e.*, the heart is not at exactly the same place at the same position in each cardiac cycle). This error increases with increasing acquisition time. By having a full left ventricular scan in only 10–20 cardiac cycles, patient movement errors were reduced compared to a 3-min recording. With the conventional rotating stepper motor acquisition, geometrical distortions are introduced due to irregular movement of the motor device, which must be kept in the exact same position during 3 min. This distortion did not occur using the freehand scanning technique because the probe movement was measured continuously. This flexibility also made it easier to select the best acoustic window possible during acquisition.

Despite heart beat-to-beat variations, it was possible to do volume reconstruction by exploiting the fact that the variations were most prominent in the diastolic phase, where the heart movements were minimal. Still, errors occurred due to the lack of synchronization between the ECG trigger and the image sampling. These jitter artefacts were minimized by using high frame rate, demonstrated by the reconstructions in Fig. 9.

Problems with interference in the magnetic field were eliminated by not using ferromagnetic materials in proximity to the transmitter and the sensor of the position system. The actual size of the sensor was 25.4 · 25.4 · 20 mm and did not limit the accessibility of the probe. Smaller sensors do exist, however, having sufficient accuracy for 3-D ultrasound (Leotta et al. 1997a).

Attempts have been made to reconstruct 3-D color Doppler data based on the scanner video signal (Picot et al. 1993; Belohlavek et al. 1994). These methods were limited by the fact that they could not access the original Doppler measurements. With the introduction of digital 3-D Doppler acquisition, improved 3-D reconstruction was achieved by processing the individual Doppler and tissue signals separately. The velocity values were also available for quantitative analysis of, for instance, the instantaneous volume blood-flow rate. This can be calculated from the velocities defined by the flow region in Fig. 11c.

The low frame rate of the video-based systems limits the possibility of imaging the dynamic properties of the heart valves (Salustri et al. 1995). The temporal resolution in our 3-D data was equal to the resolution in the original 2-D data, and exceeded 100 frames per s. Reconstruction and visualization of a complete cardiac cycle was achieved without any mismatch between the start and the end of the cycle, which can occur using too low a frame rate.

Limitations

For patients with severe arrhythmias, the method described will result in reconstruction errors. Nonrepresentative cardiac cycles need to be eliminated during acquisition. For patients only able to have short breath-holds, there may not be sufficient time to cover the area of interest. Combining several 3-D scans may solve this problem.

At the time of performing the experiments, the data storage and transfer to computer hard disk took several min. This is currently being improved with a high-speed link from the scanner digital replay memory to the memory on the PC. This enables the 3-D data to be reconstructed immediately after scanning (1 min), and verification of each scan will be possible during patient examination.

CONCLUSION

From the results, we conclude that freehand 3-D acquisition of digital ultrasound data can produce dynamic volume reconstructions with temporal resolution up to 150 frames/s, with reconstruction errors smaller than the ultrasound beam resolution. We achieved high frame rate 3-D reconstructions with reduced jitter artefacts. Dynamic 3-D reconstruction of a 6 · 7 cm area containing the mitral valve at 12 cm depth was recorded with full temporal (less than 7 ms) and spatial resolutions in 12 cardiac cycles. The digital ultrasound data made it possible to reconstruct 3-D Doppler measurements of both blood flow velocity and tissue velocity. The velocity values could be extracted for quantitative analysis. In future systems, nonrepresentative cardiac cycles should be excluded from the reconstruction, and have the possibility to combine several scans.

Acknowledgements — We thank Thomas Langø, SINTEF Unimed, Trondheim, Norway, for the assistance with the position sensor calibration, and Stig A. Slørdahl, Department of Physiology and Biomedical Engineering, NTNU, Trondheim, Norway, for help with the phantom experiments.

REFERENCES

Angelsen BAJ. Waves, signals and signal processing in medical ultrasonics. Dept. of Physiology and Biomedical Engineering, The Norwegian University of Science and Technology (NTNU). Vol. 1. Trondheim, Norway: NTNU, 1995.

Barry CD, Allott CP, John NW, et al. Three-dimensional freehand ultrasound: image reconstruction and volume analysis. Ultrasound Med Biol 1997;23:1209–1224.

Belohlavek M, Foley DA, Gerber TC, et al. Three-dimensional reconstruction of color Doppler jets in the human heart. J Am Soc Echo 1994;7:553–560.

Blaas HG, Eik-Nes S, Berg S, Torp H. In-vivo three-dimensional ultrasound reconstructions of embryos and early fetuses. Lancet 1998;352:1182–1186.

Detmer PR, Bashein G, Hodges T, et al. 3-D ultrasonic image feature localization based on magnetic scanhead tracking: in vitro calibration and validation. Ultrasound Med Biol 1994;20:923–936.

Geiser EA, Ariet M, Conetta DA, et al. Dynamic three-dimensional echocardiographic reconstruction of the intact human left ventricle: Technique and initial observations in patients. Am Heart J 1982; 103:1056–1065.

Gilja O, Smievoll A, Thune N, Matre K, Hausken T, Ødegaard S, Berstad A. In vivo comparison of 3-D ultrasonography and magnetic resonance imaging in volume estimation of human kidneys. Ultrasound Med Biol 1995;21:25–32.

Gilja O, Thune N, Matre K, Hausken T, Ødegaard S, Berstad A. In vitro evaluation of three dimensional ultrasonography in volume estimation of abdominal organs. Ultrasound Med Biol 1994;20: 157–165.

Gopal AS, Keller AM, Rigling R, King DL Jr, King DL. Left ventricular volume and endocardial surface area by three-dimensional echocardiography: comparison with two-dimensional echocardiography and nuclear magnetic resonance imaging in normal subjects. J Am Coll Cardiology 1993;22:258–270.

Heimdal A, Støylen A, Torp H, Skjærpe T. Real-time strain rate imaging of the left ventricle by ultrasound. J Am Soc Echo 1998; 11:1013–1019.

Hughes SW, D'Arcy TJ, Maxwell DJ, et al. Volume estimation from multiplanar 2D ultrasound images using a remote electromagnetic position and orientation sensor. Ultrasound Med Biol 1996;22:561–572.

Kasai C, Namekawa K, Koyano A, Omoto R. Real-time two-dimensional blood flow imaging using an autocorrelation technique. IEEE Trans Sonics Ultrason 1985;SU-32:458–464.

King DL, King DL Jr, Shao MYC. Three-dimensional spatial registration and interactive display of position and orientation of real-time ultrasound images. J Ultrasound Med 1990;9:525–532.

Leotta DF, Detmer PR, Martin RW. Performance of a miniature magnetic position sensor for three-dimensional ultrasound imaging. Ultrasound Med Biol 1997a;23:597–609.

Leotta DF, Munt BM, Bolson EL, et al. Quantitative three-dimensional echocardiography by rapid imaging from multiple transthoracic windows: in vitro validation and initial in vivo studies. J Am Soc Echo 1997b;10:830–839.

Merz E, Bahlmann F, Weber G. Volume scanning in the evaluation of fetal malformations: A new dimension in prenatal diagnosis. Ultrasound Obst Gynecol 1995;5:222–227.

Miyataka K, Yamagishi M, Tanaka N, et al. New method for evaluating left ventricular wall motion by color-coded tissue Doppler imaging: in vitro and in vivo studies. J Am Coll Cardiol 1995;25:717–724.

Moritz WE, Pearlman AS, Cabe DHM, et al. An ultrasonic technique for imaging the ventricle in three dimensions and calculating its volume. IEEE Trans Biomed Engin 1983;30:482–492.

Picot PA, Rickey DW, Mitchell R, Rankin RN, Fenster A. Three-dimensional colour Doppler imaging. Ultrasound Med Biol 1993; 19:95–104.

Prager RW, Rohling RN, Gee AH, Berman L. Rapid calibration for 3-D freehand ultrasound. Ultrasound Med Biol 1998;24:855–869.

Salustri A, Becker AE, Van Herwerden L, Vletter WB, Ten Cate FJ, Roelandt JRTC. Three-dimensional echocardiography of normal and pathologic mitral valve: a comparison with two-dimensional transesophageal echocardiography. J Am Coll Cardiol 1996;27: 1502–1510.

Salustri A, Spitaels S, McGhie J, Vletter W, Roelandt JRTC. Transthoracic three-dimensional echocardiography in adult patients with congenital heart disease. J Am Coll Cardiol 1995;26:759–767.

Shiota T, Jones M, Chikada M, et al. Real-time three-dimensional echocardiography for determining right ventricular stroke volume in an animal model of chronic right ventricular volume overload. Circulation 1998;97:1897–1900.

Smith SW, Pavy HG Jr, von Ramm OT. High-speed ultrasound volumetric imaging system—Part I: transducer design and beam steering. IEEE Trans Ultrason Ferrelec Freq Contr 1991;38:100–108.

Steen E, Olstad B. Volume rendering of 3-D medical ultrasound data using direct feature mapping. IEEE Trans Med Imaging 1994;13: 517–525.

Thune N, Gilja OH, Hausken T, Matre K. A practical method for estimating enclosed volumes using 3-D ultrasound. Eur J Ultrasound 1996;3:83–92.

Paper G

Volumetric blood flow measurement using dynamic three-dimensional ultrasound color flow imaging

Sevald Berg, Hans Torp, Bjørn Olav Haugen[†] and Stein Samstad[†]

Department of Physiology and Biomedical Engineering,
Norwegian University of Science and Technology, Trondheim, Norway
[†]Department of Cardiology and Lung Medicine,
Norwegian University of Science and Technology, Trondheim, Norway

Abstract

A new method for measuring blood volume flow using freehand dynamic three-dimensional echocardiography was developed. During 10–20 cardiac cycles the ultrasound probe was slowly tilted while its spatial position was continuously recorded with a magnetic position sensor system. The ultrasound data were acquired in color flow imaging mode, and the separate raw digital tissue and Doppler data were transferred to an external PC for post-processing. From each time step in the reconstructed three-dimensional data, one cross-sectional slice was extracted with the measured and recorded velocity vector components perpendicular to the slice. The volume flow rate through these slices was found by integrating the velocity vector components, and was independent of the angle between the actual flow direction and the measured velocity vector. Allowing the extracted surface to move according to the movement of anatomical structures, an estimate of the flow through the cardiac valves was achieved. The temporal resolution was preserved in the three-dimensional reconstruction, and with a frame rate of up to 104 frames/s the reconstruction jitter artifacts were reduced. Examples of *in vivo* blood volume flow measurement are given, showing the possibilities of measuring the cardiac output and analyzing blood flow velocity profiles.

Submitted for publication, 1999

1 Introduction

Ultrasound Doppler is a widely used clinical tool for estimating blood volume flow and cardiac output. In the most commonly used technique, the velocity in the Doppler spectrum is traced during the systole, and the integral of this curve is multiplied with the aortic area defined by the diameter as measured by B-mode ultrasound. This calculates the stroke volume. One such method was proposed by Skjærpe [14] and consists of measuring the blood velocity by pulsed wave (PW) Doppler in the distal left ventricular outflow tract (LVOT). The modal velocity in the Doppler spectrum is traced during the systole, and the diameter is measured in the LVOT close to the insertion of the aortic valves. This technique assumes a nearly flat velocity profile, which may not reflect the actual flow distribution. It is also sensitive to errors in the Doppler sample volume placement, in the tracing of the spectrum and in the diameter measurement.

A different approach was described by Tsujino et al. [17] using two-dimensional (2D) color flow imaging (CFI). A line was placed across the flow region, and the flow volume was calculated from the corresponding velocity profile. Shiota et al. [13] applied this method to quantification of aortic regurgitation.

The aortic blood flow measurement method as described using the PW Doppler technique, is based on a Doppler sample volume placed at a constant depth throughout the cardiac cycle. This probably leads to an underestimation of the stroke volume, since the blood flow is only measured during systole where the aortic annulus moves in the opposite direction. The movement of the annulus relative to the measurement position describes a blood volume which ideally could be measured during the diastole where the annulus moves back the same distance together with the corresponding blood pool. This blood volume is lost due to the low sensitivity of the PW Doppler technique.

Since the introduction of three-dimensional (3D) ultrasound, there have been several attempts to visualize blood volume flow from 3D data containing Doppler measurements. An early attempt by Miyagi et al. [9] showed the possibility of creating 3D color flow images from the umbilical cord. Picot et al. [10] described a 3D color flow system for visualizing the carotid artery. Visualizations of dynamic 3D intracardiac color flow jets have also been performed[1, 4].

Most methods presented so far have been based on the video output signal from the ultrasound scanner. This makes it difficult to do quantitative analysis of the flow data, since the color values from the video signal are results of a mapping from the original Doppler frequencies. This mapping includes processing with the purpose to give optimal visualization of the flow and is not necessarily optimal for flow quantization.

The video data also suffer from poor temporal resolution (25 frames/s for the PAL video standard). This causes reconstruction jitter artifacts due to the lack of synchronization between the ECG signal and the video signal sampling. As a result, the reconstructed data will consist of neighboring image frames deviating up to 20 ms relative to the ECG trigger position. With the limited temporal resolution in the ultrasound scanner itself this error will increase since the ultrasound image sampling and the video grabbing are not synchronized. This jitter introduces errors when the

3D color flow data are used quantitatively. In addition, low temporal resolution may under-sample the flow velocities.

Most of the work presented on quantitative 3D flow has been performed *in vitro*. Guo et al. [5] described how flow through a test phantom could be quantified using 3D color Doppler. However, when measuring Doppler frequencies in the heart *in vivo*, additional problems arise due to the moving heart walls. Recently, the possibility of calculating regurgitant jet volume has been demonstrated [3, 18].

The purpose of this work was to develop a new method for calculating the cardiac blood volume flow *in vivo* using 3D color Doppler data, where the data were acquired using a freehand position sensor, and where the raw digital data from the scanner were captured at high frame rates.

The development of dynamic 3D echocardiography has made it possible to reconstruct 3D cardiac sequences of separate tissue and color flow data with no loss of temporal resolution, and with small spatial reconstruction errors [2]. The volume flow algorithm was based on an angle-independent measurement method [11, 15]. The general idea was to extract the measured velocity vector components that were perpendicular to a cross-sectional slice through the flow tract and estimate the volume flow independent of the flow direction. Haugen et al. [6] has validated the method *in vivo*, and one example showing the possibilities of blood volume flow measurements is given in the present paper.

2 Materials and methods

2.1 Data acquisition

Raw digital data were acquired using a System Five ultrasound scanner (GE Vingmed Ultrasound, Horten, Norway) with a 2.5 MHz phased array transducer. The spatial position and orientation of the probe was continuously recorded with a position sensor system (Flock of Birds, Ascension Technology Corp., Burlington, USA), consisting of a magnetic field transmitter and a sensor (receiver) which was mounted directly on the probe. The transmitter and the sensor were both coupled to an electronic control unit, and the sensor had to be located inside the magnetic field of the transmitter. The operating range of the sensor was 25–60 cm from the transmitter. The control unit was coupled directly to the scanner. The sensor position coordinates were stored in the digital replay memory together with the corresponding image frames and all other relevant scanner parameters including the ECG signal.

The data were acquired with frame rates up to 104 frames/s in color flow imaging mode. From a transthoracic apical position, the probe was tilted slowly during held end-expiration (Figure 1). Typically, one complete scan lasted 10–20 cardiac cycles. The raw digital ultrasound data consisting of separate 8-bit tissue values and 16-bit color flow values, were transferred to an external PC for 3D reconstruction.

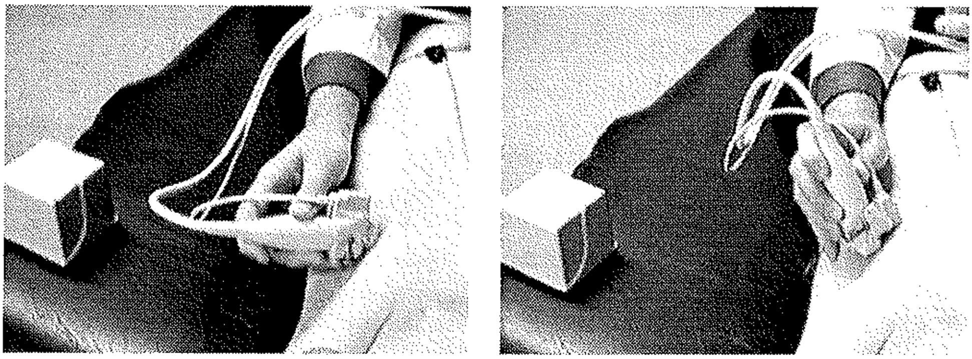

Figure 1: The probe was slowly tilted from the start to the end position during 10–20 cardiac cycles through the left ventricle from an apical position, covering the LVOT. The patient must not breathe or move during the data acquisition.

2.2 Volume flow measurement data

To reconstruct volumetric data from each consecutive time step, the raw scan line data from the 2D scan planes were reorganized according to their position in the cardiac cycle using a prototype version of the EchoPAC-3D software (GE Vingmed Ultrasound, Horten, Norway). The data from the first scan plane in each cycle (defined by the ECG), were used to build up the first volume, and data from the second scan plane the second volume and so on [2].

One 2D slice was extracted from the 3D data for all the different time steps (Figure 2). Both the raw tissue and the Doppler values were resampled on this surface. Since the ultrasonic beam was perpendicular to this surface at all points, the measured blood flow velocity component was perpendicular to the surface. The position of this surface was then given only by the depth, which was manually positioned while browsing the 3D data.

The probable underestimation of the aortic outflow due to the moving annulus was avoided using the described cross-sectional surface. The blood volume that passed through the same anatomical structure (e.g., the aortic annulus) was calculated. The surface was manually positioned at the desired depth at start- and end-systole. Between these positions, the surface depths were interpolated resulting in a surface that followed the movement of the selected structure. The velocity of this movement was recorded and added to the blood velocity.

The extracted surface data were represented by two $U \times V \times N$ matrices for the raw tissue values and Doppler values respectively, where $U \times V$ was the size of the surface and N was the number of time steps. The Doppler values were the pulse-to-pulse complex autocorrelation function values for zero and unity lags, $R(0)$ and $R(1)$. These values were used to estimate the signal power, $P = R(0)$, and the center

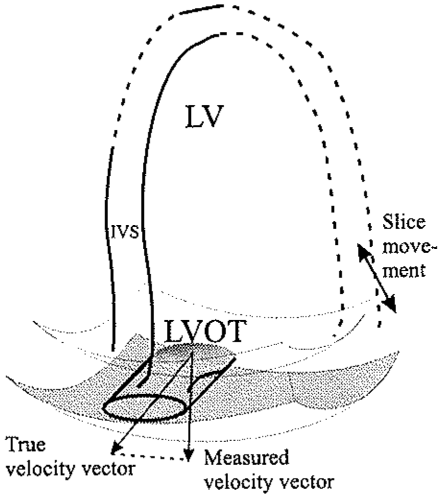

Figure 2: The reconstructed volume at one time instance; the volume contains part of the left ventricle (LV), the intraventricular septum (IVS) at left, and the left ventricle outflow tract (LVOT). The measured velocity vector components are perpendicular to the extracted surface.

frequency, $w = \arg R(1) \in [-\pi, \pi]$ [16]. The Doppler frequency w was proportional to the blood flow velocity used in the volume flow calculations. Further processing on these autocorrelation function values was performed using MATLAB (MathWorks Inc., Natick, MA, USA).

2.3 Region of interest

Inside the Doppler flow region in the extracted slice, flow was detected from several sources. To prevent unwanted velocities from being used in the volume flow calculations, a region of interest (ROI) was manually indicated in the data. For the aortic outflow, one ROI was defined in the start-systolic frame and one in the end-systolic frame. Interpolation was performed for the frames in between. These contours were not used as the exact flow border definition, but only to exclude surrounding blood flow. This also reduced the errors from drop-out effects occurring when low gain tissue causes blood flow to be incorrectly detected.

2.4 Spatial and temporal signal smoothing

To smooth the data and reduce the variance, the values $R(0)$ and the complex $R(1)$ were filtered with a spatial average filter mask. The filter size depended on the amount of oversampling in the reconstructed 2D slice. The tissue values were detected with a higher spatial resolution than the Doppler values in the original scan plane (azimuth direction). During the resampling, the elevation resolution was set approximately equal to the original azimuth tissue resolution and equal for both the tissue and the Doppler values. The spatial Doppler filter size was adjusted so that it was close to the original Doppler sampling density. The data were then smoothed in the temporal direction by averaging each value with the values from the previous and the next time step. Finally, spatial interpolation was performed. The tissue values were filtered and interpolated accordingly.

2.5 Baseline shift

Aliasing of the Doppler frequency is common for the highest velocities during the aortic outflow. These values can be baseline shifted (unwrapped) to give the correct velocity value. In areas where high velocity blood flow meets slowly moving tissue, the filtering and interpolation of the aliased velocity values introduce velocity estimate errors. We corrected for this effect by first baseline shifting the aliased values, then dividing the complex $R(1)$-argument by 2 before doing the filtering and interpolation, and adjusting the nyquist velocity accordingly.

2.6 Volume flow calculation

All velocity vectors in the resampled cross-sectional surface were the components along the ultrasound beams. These vector components were perpendicular to the surface. By integrating all velocities across the surface, it was possible to calculate the total blood volume flow independent of the angle between the ultrasound beam and the flow direction. The magnitude of the velocity vector component at each position (x, y) at time n was given by

$$v_n(x,y) = v_{nyq} \cdot w_n(x,y)/\pi - v_n^{surf}, \quad n \in [0, N-1], \quad x, y \in U \times V. \tag{1}$$

Here, v_n was corrected for the velocity of the cross-sectional surface v_n^{surf}. N is the number of time steps and v_{nyq} is the nyquist velocity (Figure 3).

The instantaneous blood volume flow (the flow rate) through the region $U \times V$ at time n, was given by

$$q(n) = \sum_{k=0}^{U-1} \sum_{l=0}^{V-1} \Delta A(n) \cdot v_n(k,l), \tag{2}$$

where ΔA is the area occupied by one velocity vector component. The size of this area was time dependent since the surface was allowed to move; it was given by the Doppler resampling resolution which decreased with the distance from the probe. The velocity v_n was different from zero only when blood was detected.

The total blood volume flow was found by integrating the blood volume flow curve:

$$Q = \sum_{i=0}^{N-1} q(i)\Delta t, \tag{3}$$

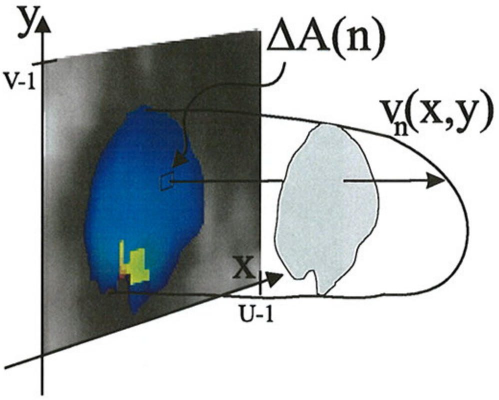

Figure 3: The 3D flow profile at time n consists of a set of discrete vector components $v_n(x, y)$ representing the velocity in the area ΔA.

where Δt is the temporal resolution. When N equaled the length of the cardiac cycle, Q was the stroke volume (SV). The cardiac output (CO) was then the SV multiplied by the heart rate: $CO = SV \cdot HR$.

2.7 *In vivo* volume flow

Dynamic 3D data from the aortic outlet were collected from a healthy volunteer without evidence of cardiac disease. We also calculated the CO by using the routine method as described by Skjærpe [14].

After transferring the raw digital ultrasound data from the scanner to the external computer, the instantaneous blood volume flow and the cardiac output were calculated from two different cross-sectional surface positions. First, the surface was placed in the aortic annulus moving along with this structure throughout the systole. Then the surface was placed 0.5 cm above the annulus in start-systole and kept at that depth throughout the systole (Figure 4). The last approach made direct comparison with the PW Doppler method possible.

3 Results

3.1 Raw data 3D reconstruction

After filtering the separate raw tissue and Doppler data, the different velocities were color encoded and mixed with the gray level tissue values. This produced a color overlay image similar to normal 2D CFI (Figure 5). This tissue/flow arbitration depended on the power of the signals. The moving myocardial tissue created positive Doppler frequencies (dark red) which were ignored after arbitration due to low signal power.

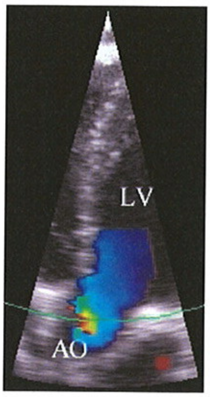

Figure 4: Mid-systolic outflow from the left ventricle (LV) through the aortic outlet (AO). The green curve indicates the intersection with the cross-sectional slice passing through the annulus.

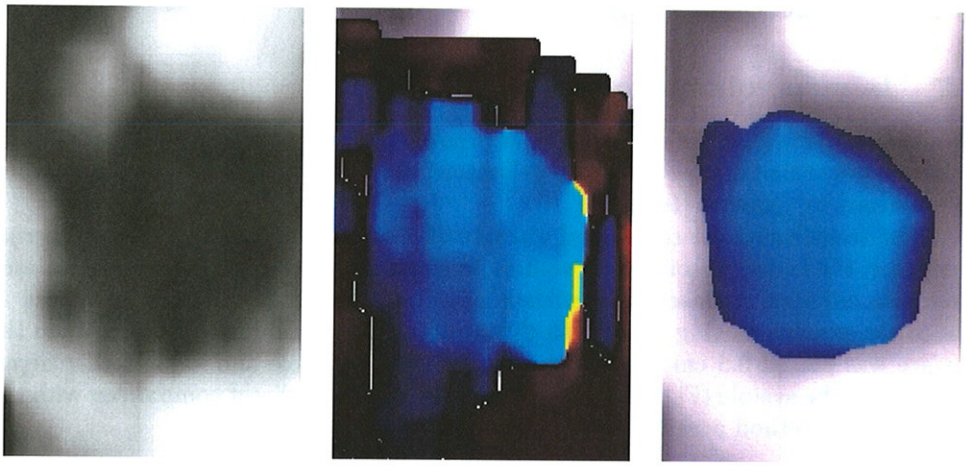
(a) (b) (c)

Figure 5: One slice through the 3D data in the distal LVOT during the aortic outflow in systole. (a) The raw tissue data. (b) The corresponding raw Doppler values. The negative velocities (away from the probe) are coded in blue. The red and dark colors are positive velocities (towards the probe). (c) Combination of the filtered, separate tissue and Doppler values. Note that the colors represent the velocity vector components perpendicular to the image plane.

The effect of filtering and arbitration is also shown in Figure 6 where one line through the data was plotted. The clutter filter removed signals with low frequency. This missing blood flow was seen near the tissue border (Figure 5).

Interpolation and filtering of raw Doppler data containing aliased blood velocities and tissue velocities resulted in over-estimated flow border values. With the corrected baseline shift algorithm this error was reduced (Figures 7 and 8).

Successful acquisition and reconstruction of 3D color flow data with temporal resolution of less than 10 ms were achieved (Figure 9). With a frame rate of 104 frames/s, the 3D data contained a total of 120 time steps through the cardiac cycle. There were 31 volumes with color flow data during the systole. With this time resolution, the maximal timing error (jitter) between two consecutive slices in one 3D volume was 4.8 ms.

3.2 Aortic blood volume flow

The instantaneous blood volume flow was calculated from both the moving and the fixed surface (Figure 10). The fixed surface was placed in the same position as the sample volume from the PW Doppler method, giving comparable flow volume estimates. With the fixed surface the CO was 4.5 l/min (SV=91.9 ml), while with the PW Doppler estimates the CO was 4.0 l/min (SV=87.0 ml). The moving surface resulted in a greater flow volume (CO=5.5 l/min and SV=112.9 ml). In this case, the average velocity of the surface was used. The blood flow volume represented by the movement of the annulus corresponded to 11% of the cardiac output.

We found that the velocity profiles in different persons had different shapes (Figure 11), indicating that the form of the profile was subject to individual variability.

4 Discussion

Measurement of cardiac blood volume flow by the conventional Doppler method is an established clinical procedure [14]. It is easy to perform and gives an estimate of the cardiac output. There are, however, several shortcomings to this method. The Doppler velocity is measured from within a small sample volume, and the cardiac output estimate is sensitive to the placement of this volume [7]. The method assumes a flat velocity profile, but it has been shown that the flow velocity distribution in the aorta may have different characteristics, which can influence the velocity estimates of this method [12]. This was also illustrated by the 3D reconstructions in this study. In addition, the method is sensitive to errors in the tracing of the Doppler spectrum.

Several techniques have been proposed to improve volume flow estimation based on the principle of integrating velocity vectors across a surface. Sun et al. [15] estimated the volume flow rate by surface integration of velocity vectors from two rotated planes. Poulsen and Kim [11] showed a similar method using several rotated planes and it was tested in an *in vitro* model. This method was also applied *in vivo* [8]. Common for these methods was that the volume flow was estimated independently of the angle

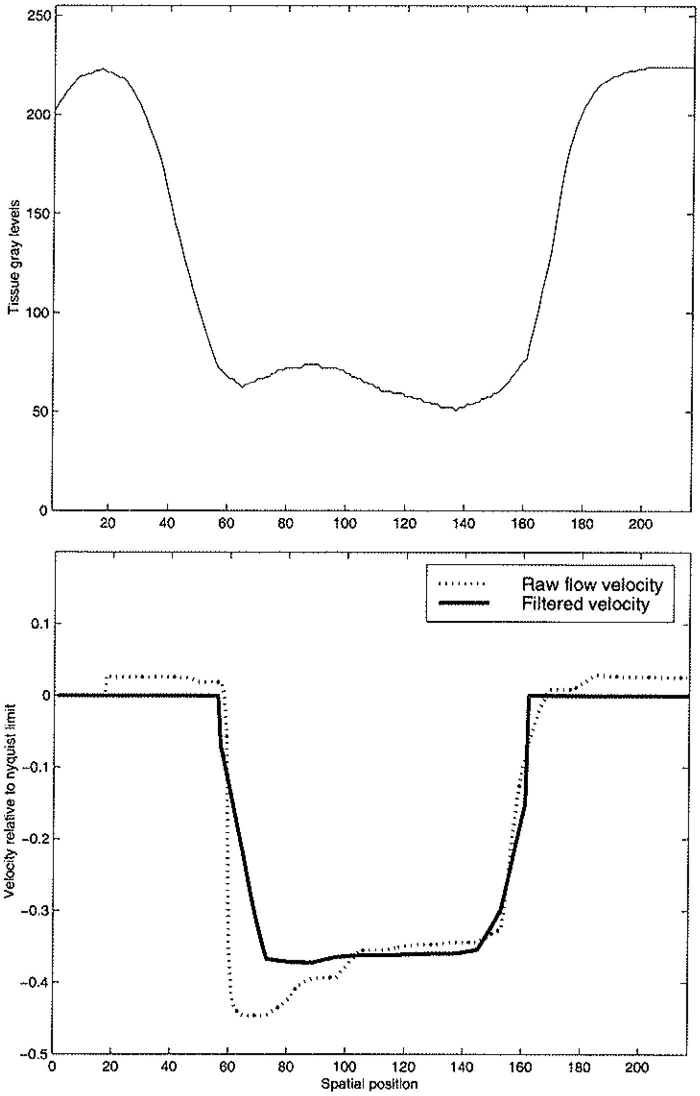

Figure 6: Plots of one vertical line in Figure 5. The gray level tissue values (above), the raw flow data velocity (below, dotted), and the filtered flow values (below, solid). The nyquist limit is at -0.5.

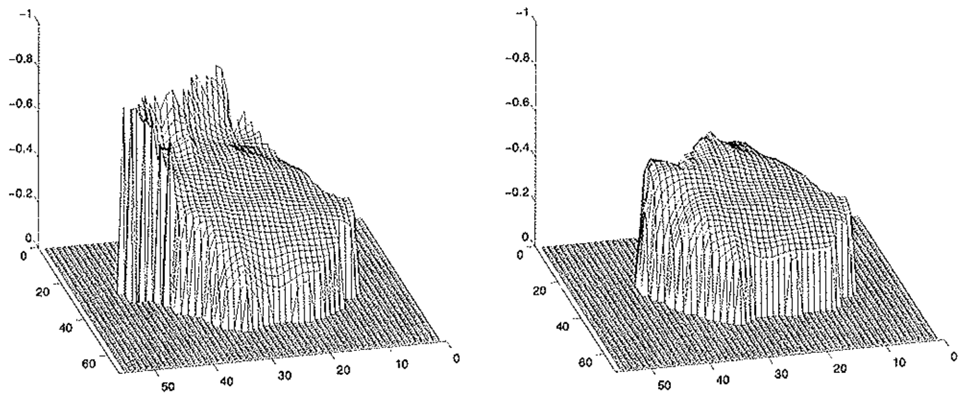

(a) (b)

Figure 7: Mesh plots of aortic flow velocity profile with aliased velocities near the tissue border. The height of the mesh is proportional to the blood velocity. (a) Over-estimated border velocities. (b) Border values decreased towards zero velocity using the corrected baseline shift algorithm.

between the ultrasound beam and the blood flow. We also used this approach, but unlike the previously presented methods, our method used a full 3D dataset consisting of raw digital color flow data to estimate and visualize the blood flow. Using high frame rates, it was not necessary to average the flow measurements from several consecutive cardiac cycles as described earlier [8, 11]. There were, however, still limitations to the accuracy with which we could measure the blood flow due to errors from Doppler velocity estimation, aliasing and 3D reconstruction.

The Doppler frequency shift from the backscattered ultrasound signal contains information from both moving blood and tissue (clutter). The separation of blood and tissue moving at equal velocities was not possible, so this clutter filtering resulted in a loss of blood signals with low velocity. Too low a cutoff frequency for filtering clutter gave a bias in the estimate towards zero velocity.

Aliased velocities were overestimated at the border between the tissue and the blood. This occurred when the unwrapped velocity values were averaged with slowly moving tissue velocity values. Correct unwrapping of the aliased velocities is difficult, especially when flow in two directions occurs simultaneously. In our calculations, however, we considered only flow in one direction at the time, making a baseline shift possible.

It has been shown that the reconstruction errors for this freehand technique were smaller than the resolution of the original ultrasound beam [2]. The jitter artifacts in the 3D reconstruction were at most 10 ms when the frame rate was 50 frames/s. This introduced errors in the volume flow estimates; these errors were reduced by increasing

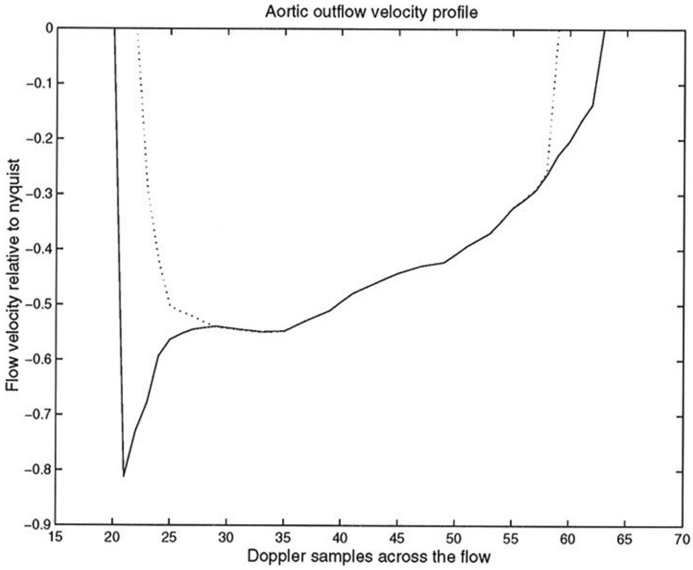

Figure 8: Plot of one line through the data in Figure 7. The solid curve is the profile with the over-estimated border values and the dotted curve is the corrected profile which decreases towards zero. The nyquist limit is at -0.5.

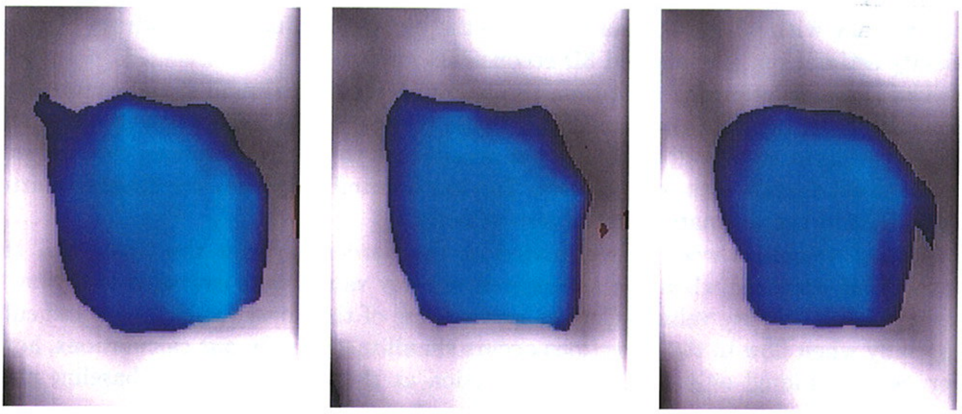

Figure 9: Three consecutive slices of aortic outflow with a time resolution of 9.6 ms.

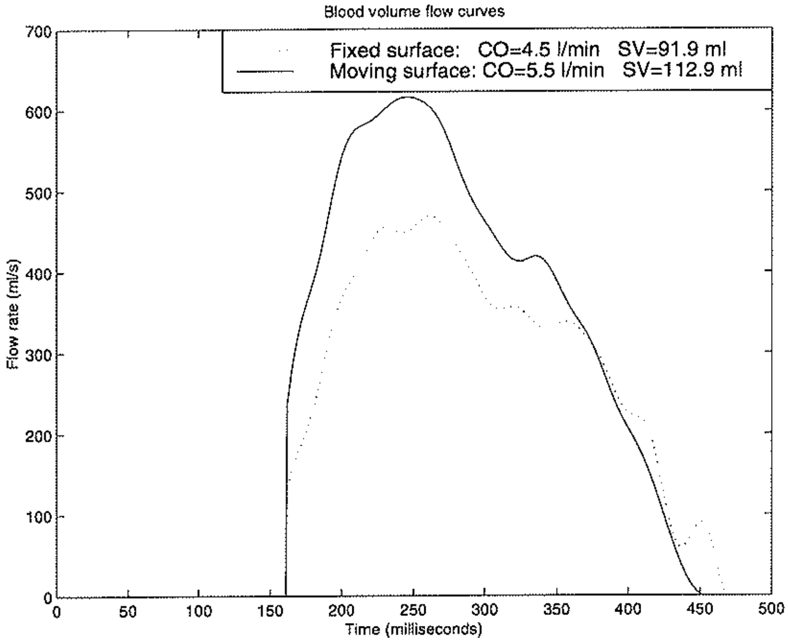

Figure 10: *In vivo* blood volume flow curves from two different measurements, showing the aortic outflow during systole. Moving surface (solid) and fixed surface (dashed).

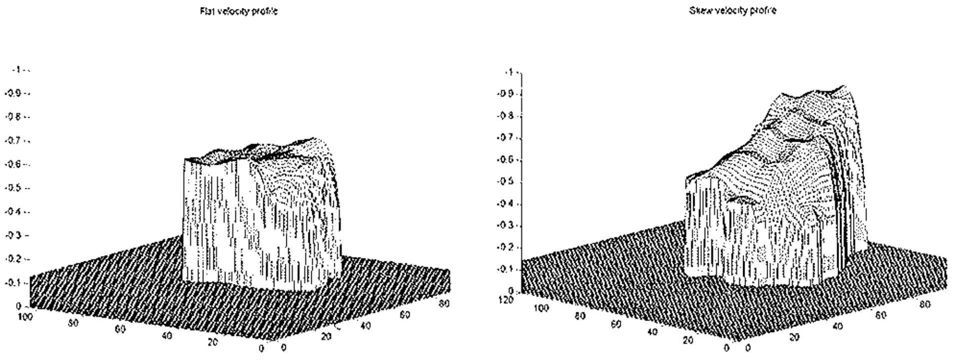

(a) (b)

Figure 11: Two velocity profiles in two different persons from the aortic outflow in the peak systole with different characteristics. The velocity scale was defined with the nyquist velocity at -0.5. (a) Flat profile. (b) Skew profile with higher velocities towards the intraventricular septum.

the frame rate. As shown, it was possible to reconstruct 3D color flow data with a frame rate of 104 frames/s, reducing the jitter to a maximum of 4.8 ms.

For gated 3D ultrasound, movement of the patient during acquisition results in reconstruction errors. In the present study, this error was reduced by the short acquisition time (10–20 s).

Poor detection of the myocardial tissue introduced uncertainty in the flow region definition, and resulted in volume flow estimation errors. It was important to tilt the probe sufficiently to totally cover the flow and surrounding tissue area.

The method has been evaluated *in vivo* in 18 persons by comparison with the 2D PW Doppler method [6], and showed good agreement with a mean difference of 0.3 l/min using a fixed surface and 0.7 l/min using a moving surface. These results confirm the tendency given by the patient example in the present paper. Since the raw data were used in the reconstructions, and since the cross-sectional surface was clearly placed in relation to anatomical structures, one potential of this method is greater independence of the examiner than is possible with the ordinary PW Doppler method.

4.1 Limitations

The acquisition method presented here required regular heart rhythm during the scanning. Even though the scan time is short, there may not be sufficient time to cover the area of interest for patients not able to hold their breath. In addition, the acoustic window must provide sufficient access to cover the whole flow region.

5 Conclusion

The present method enables calculation of blood volume flow versus time throughout the cardiac cycle *in vivo* with freehand 3D ultrasound using raw digital tissue and Doppler data. The 3D reconstructed flow data had the same temporal resolution as the original 2D data. As much as 104 frames/s were achieved reducing the reconstruction jitter artifacts to less than 5 ms which were small compared to the physiological beat-to-beat variations. The blood volume flow through the LVOT was correctly measured with respect to the movement of the aortic annulus relative to the probe. The method was angle independent and no assumption of the flow geometry was made. In addition, blood flow velocity profiles could be analyzed throughout the cardiac cycle.

6 Acknowledgments

The authors thank Ditlef Martens, Christian Michelsen Research, Bergen, Norway, for developing software for reconstruction of the 3D data, and Nancy Eik-Nes for revision of the paper.

References

1. M. Belohlavek, D. A. Foley, T. C. Gerber, et al. Three-dimensional reconstruction of color Doppler jets in the human heart. *J Am Soc Echocardiogr*, 7(6):553–560, 1994.

2. S. Berg, H. Torp, D. Martens, et al. Dynamic three-dimensional freehand echocardiography using raw digital ultrasound data. *Ultrasound Med Biol*, 25(5):745–753, 1999.

3. R. De Simone, G. Glombitza, C. F. Vahl, J. Albers, H. P. Meinzer, and S. Hagl. Three-dimensional color Doppler: a new approach for quantitative assessment of mitral regurgitant jets. *J Am Soc Echocardiogr*, 12(3):173–185, 1999.

4. A. Delabays, L. Sugeng, N. G. Pandian, et al. Dynamic three-dimensional echocardiographic assessment of intracardiac blood flow jets. *Am J Cardiol*, 76:1053–1058, 1995.

5. Z. Guo, M. Moreau, D. W. Rickey, P. A. Picot, and A. Fenster. Quantitative investigation of in vitro flow using three-dimensional colour doppler ultrasound. *Ultrasound Med Biol*, 21(6):807–816, 1995.

6. B. O. Haugen, S. Berg, S. O. Samstad, T. Skjærpe, and H. Torp. A new method to measure volumetric blood flow in the aorta based on freehand three-dimensional color flow imaging acquired at high frame rate. An in vivo validation. Submitted for publication, 1999.

7. H. Ihlen, J. P. Amlie, J. Dale, et al. Determination of cardiac output by Doppler echocardiography. *Br Heart J*, 51:54–60, 1984.

8. W. Y. Kim, J. K. Poulsen, K. Terp, and N.-H. Staalsen. A new Doppler method for quantification of volumetric flow: in vivo validation using color Doppler. *J Am Coll Cardiology*, 27(1):182–192, 1996.

9. Y. Miyagi, H. Masaoka, N. Akamatsu, and K. Sekiba. Development of a three-dimensional color Doppler system. *Med Prog Technol*, 18:201–208, 1993.

10. P. A. Picot, D. W. Rickey, R. Mitchell, R. N. Rankin, and A. Fenster. Three-dimensional colour Doppler imaging. *Ultrasound Med Biol*, 19(2):95–104, 1993.

11. J. K. Poulsen and W. Y. Kim. Measurement of volumetric flow with no angle correction using multiplanar pulsed Doppler ultrasound. *IEEE Trans Biomed Eng*, 43(6):589–599, 1996.

12. O. Rossvoll, S. Samstad, H. G. Torp, et al. The velocity distribution in the aortic anulus in normal subjects: a quantitative analysis of two-dimensional Doppler flow maps. *J Am Soc Echocardiogr*, 4(4):367–378, 1991.

13. T. Shiota, M. Jones, S. Aida, et al. Calculation of aortic regurgitant volume by a new digital Doppler color flow mapping method: an animal study with quantified chronic aortic regurgitation. *J Am Coll Cardiology*, 30(3):834–842, 1997.

14. T. Skjærpe. *Principles of volume flow measurements. In: J. R. T. C. Roelandt et al., editors. Cardiac Ultrasound*, pages 199–205. Churchill Livingstone, 1993.

15. Y. Sun, P. Ask, B. Janerot-Sjöberg, L. Eidenvall, D. Loyd, and B. Wranne. Estimation of volume flow rate by surface integration of velocity vectors from color Doppler images. *J Am Soc Echocardiogr*, 8(6):904–914, 1995.

16. H. Torp, K. Kristoffersen, and B. A. J. Angelsen. Autocorrelation techniques in color flow imaging: signal model and statistical properties of the autocorrelation estimates. *IEEE Trans Ultrason Ferrelec Freq Contr*, 41(5):604–612, 1994.

17. H. Tsujino, E. Shiki, M. Hirama, and K. Iinuma. Quantitative measurement of volume flow rate (cardiac output) by the multibeam Doppler method. *J Am Soc Echocardiogr*, 8(5):621–630, 1995.

18. J. Yao, N. D. Masani, Q.-L. Cao, P. Nikuta, and N. G. Pandian. Clinical application of transthoracic volume-rendered three-dimensional echocardiography in the assessment of mitral regurgitation. *Am J Cardiol*, 82:189–196, 1998.